Real-time atomic-resolution probing of lithium ion intercalation in TiO_2–related anodes using transmission electron microscopy

by

Sung Joo Kim

A dissertation submitted in partial fulfillment
of the requirements for the degree of
Doctor of Philosophy
(Materials Science and Engineering)
in the University of Michigan
2015

Doctoral Committee:

Adjunct Professor Xiaoqing Pan, Co-Chair
Assistant Professor Emmanouil Kioupakis, Co-Chair
Adjunct Professor George W. Graham
Professor Joanna Millunchick
Professor Jamie D. Phillips

Dedication

This work is dedicated to my parents, my sister, and my fiancée.

Acknowledgment

I would like to, first, thank my advisor, professor Xiaoqing Pan. He has guided me through my entire PhD career with many thoughtful advices both inside and outside of research. I would like to also thank Dr. George Graham for his tremendous scientific support on large portion of my research. None of PhD works including those presented in this document would have been possible without their guidance. I would like to thank other members of my committee. Professor Jamie Phillips was responsible for guiding me through a large portion of my early PhD works, which unfortunately are not included in this thesis. Professor Emmanouil Kioupakis was always willing, as a co-chair of doctoral committee, to appreciate and support my work. Professor Joanna Millunchick was very supportive in bringing up nice collaboration works. Although not being part of my doctoral committee, I sincerely thank professor Anton van der Ven, professor Rachel Goldman, professor Pei-cheng Ku, and professor Pierre Ferdinand Poudeu for many advices on data analysis and manuscript writing.

I want to also thank all the staffs at Electron Microbeam Analysis Laboratory, Dr. John Mansfield, Dr. Kai Sun, and Dr. Haiping Sun, who were very willing to be of help for operation of instruments even at night. I want to appreciate many helps that I received from a former employee of Nanofactory Instruments, Dr. Junhang Luo and Dr. Paul Mainwaring, who gave very helpful advices on the operation of in-situ TEM holders.

I would like to extend my appreciation to current and former members of the Pan Research Group who have been such great colleagues inside and outside of the lab for my 5.5 years of PhD. As my research mentor, Dr. Christopher Nelson guided me with TEM sample preparation, operation, and Starcraft. Dr. Obiefune Ezekoye taught me STEM operation and analysis. Dr. Kui Zhang helped me with the thin-film growth and Li ion cell testing and analysis and gave me a lot of useful insights on Li ion battery in general. Jacob R. Jokisaari was always helpful for the electrical set-up and fixing millions of problems aroused in the lab. Shuyi Zhang and Dr. Michael Katz provided me inputs for high-resolution STEM operation. I would also like to thank all my current and former Chinese colleagues including long-term visiting students and scholars including: Big Dr. Yi Zhang, Small Yi Zhang, Dr. Baihai Li, Dr. Xianfeng Du, Mingjie Xu, Guangsha Shi, Dr. Lin Xie, and Dr. Sheng Dai, Zhou Chang, Pei Lei, and Wei Cai for their kind assistance and thoughtful advices.

I must also thank all my former collaborators and supporters from many different fields of science inside the University of Michigan for supporting with sample preparations and property measurements and some for being my joyful companion during coffee breaks. These include Dr. Weimin Wang, Bor-chau Juang, Dr. Jimmy Chen, and Dr. Jinyoung Hwang for the growth and characterization of II-VI quantum dots, Dr. Michael Kuo and Dr. Taesu Oh for the growth of InGaN NWs, Dr. Andrew Martin and Dr. Kevin Grossklaus for the growth of III-V quantum dots, Dr. Pranati Sahoo and Yuanfeng Liu for the synthesis of thermoelectrics powders, and many others.

I also want to thank all my current collaborators for Li ion battery outside the University of Michigan. These include Dr. Alireza Kargar from University of California-San Diego, who always wanted to do something for me including the transition metal oxide nanowire growth, and

Donghee Chang, my lovely fiancée who helped me with theoretical calculations on a Li ion battery anode.

I am also indebted to all the Materials Science and Engineering staffs for providing me tremendous amount of assistance whenever I have concerns inside and outside the research. These include Keith McIntyre, Kevin Worth, Georgia Knope, Shelley Feller, Debbie Johnson, Pattie Vogel, and Lisa Moran. I would like to especially express my gratitude to Renee Hilgendorf who listened to all my petty complaints and made my timely graduation possible.

I would like to acknowledge my former primary funding agency, Department of Energy Office of Science, Basic Energy Sciences (DE-SC0000957) and its University of Michigan chapter program coordinator, Brenda Vyletel, who put tremendous amount of efforts in organizing so many funding-related works. I would also like to acknowledge National Science Foundation for TEM usage (DMR-0723032).

Table of Contents

List of Figures

List of Appendices

Abstract

Real-time atomic-resolution probing of lithium ion intercalation in TiO_2–related anodes using transmission electron microscopy

by

Sung Joo Kim

Nanostructured TiO_2 polymorphs such as rutile and bronze have been considered for lithium ion battery (LIB) application due to their chemical stability and accessibility. Despite their promising performance as anodes and coating materials, understanding of lithium ion behaviors in TiO_2-related systems is still controversial, since most studies have relied on bulk characterization techniques which do not present local changes in morphology. Here, we employed in-situ transmission electron microscopy (TEM) and high-resolution scanning TEM (HRSTEM) to perform nano-scale structural studies of TiO_2-related anodes upon Li intercalation.

The electrochemical study of a single-crystalline rutile TiO_2 nanowire (NW) was conducted under high-resolution TEM aided by selected area electron diffraction. The result demonstrates the two-step lithiation accompanied by the highly anisotropic volumetric expansion and phase transformation.

An in-depth study of lithiation in bronze TiO_2 (TiO_2-B) had been possible by the growth of a high-quality TiO_2-B thin film templated by Ca-modified bronze phase, $CaTi_5O_{11}$ (Ca:TiO_2-B). Various interfaces and defects in TiO_2-B and Ca:TiO_2-B thin films deposited on (100) and (110) $SrTiO_3$ substrates were first studied under HRSTEM. High crystallinity of (001) TiO_2-B on a Ca:TiO_2-B template motivated us to perform lithiation on the structure under HRTEM. Revealed by high-resolution observation of electrochemical lithiation into TiO_2-B, many defects were induced by strain relaxation upon Li-induced TiO_2-B lattice expansion. In fact, depending on Li intercalation direction into the structure, either high-symmetry structural transformation or plain shears was generated. The observations were corroborated by post-mortem HRSTEM characterization and theoretical calculation.

The capability of a TiO_2 nanostructure as a coating material for a LIB anode was also investigated via potentiostatic lithiation of a rutile TiO_2-coated Si NW. It was found that lithium intercalation into this NW occurred locally by having each segment achieving full lithiation throughout the Li migration pathway. The TiO_2 coating also influenced final lithiated morphology of a coated Si ($Li_{15}Si_4$) to be different from that of an uncoated one.

The results discussed in this thesis provide the in-depth knowledge on the Li ion dynamics in the two TiO_2 polymorphs. The application of in-situ high-resolution TEM technique can be expanded towards other polymorphs of various different structural forms.

Chapter 1. Introduction and Background

1.1. Fossil fuel

According to the 2014 energy review published by US Energy Information Administration (EIA), the fossil fuel is by far the largest primary source of US annual energy consumption, accounting for 82 % of total consumption[1], which is not much deviated from the reported percentage of global energy consumption 81 %.[2] Recently, EIA projected an alarming 38 % increase in world fuel consumption including petroleum and liquid fuels by 2040 due to increasing demand from developing countries in Asia and Middle East. According to Topal, et al., the depletion time for fossil fuel is projected to be 37, 107, and 37 years, respectively, for oil, coal, and gas.[3] A continued surge on consumption rate of fossil fuels, however, may shorten the projected depletion time and increase the unwelcoming emission of greenhouse gases (e.g. CO_2) that potentially contribute to global warming. Hence, there has been growing need and research interest for the technology for effective energy generation and storage.

1.2. Renewable Energy and Battery Market

According to the data published by International Energy Agency, the portion on modern renewables excluding traditional biomass has already passed 10 % of total global energy consumption;[4] These include geothermal, hydropower, wind, bio-fuels, and solar energy. From

those categories, solar energy has become the fastest developing renewable energy in production. According to the 2014 Global Status Report on Renewables, solar PV (photovoltaics) has demonstrated the most remarkable growth rate of 55 %, within the period from 2008 to 2013, outperforming all other renewable energies.[2] Now, it has had the second highest increase in global capacity, only second to hydropower, and recently become the fourth largest renewable energy sector. Surprisingly in 2013, there has been a first cross-over between solar cell global installment and investment, possibly indicating the decrease in the PV cost.[2] Despite continued increase in power conversion efficiency (PCE) and cost reduction, PV is still unlikely to take over a large portion of energy utilization capacity from the fossil fuel and stir up the consumption interest for this new energy source. The main reason is its installation cost. According to Beard and Nozik, the energy cost needs to be lowered as much as 0.03 $/kWh, that is a half or a third of the current average grid cost.[5] Another reason is the difficulty in solar energy storage. Environmental factors such as the position of the sun and diurnal cycles also need to be considered since they affect depreciation and the maintenance costs of solar modules.

Hence, the application of a battery for electrical energy storage (EES) is underway for successful deployment of the renewable energy technology since it meets the requirements for EES including a compact size, high cycling efficiency, and a flexible control on outputs.[6] A battery uses electrochemical means to store energy within the electrode via charge transfer reactions between the electrode and the electrolyte. This makes the operation self-sustained without having to recharge externally like other storage systems such as a fuel cell.

Hence, a battery, specifically a rechargeable (secondary) battery, is actively used for versatile applications, not just for renewable energy storage but also for portable electronics and electric vehicles (EV). A high operational capacity of a Lithium ion battery has already improved the

performance of mobile phones and laptop computers ever since Sony released its first commercial battery with much improved safety in 1991. In fact, most of newly released smartphones carry portable Li-ion batteries. According to the 2013 Li ion battery market report by Frost and Sullivan, the consumer sector including portable electronics occupies around 60% of a total Li ion battery market.[7] The second largest sector is automotives that accounts for 18.3% of a total Li ion battery market share. This market will continue its growth because of the increase in EV production and the continuing consumer demand for hybrid electric vehicles (HEVs) and plug-in hybrid electric vehicles (PHEVs). The pre-existing vehicles of such kinds like Nissan Leaf (EV) and Chevy Volt (PHEV) from General Motors continue to generate more demands in the automotive market. Other companies like BMW and Volkswagen that newly launched the electric and the hybrid electric vehicles are expecting to bring the automotive market towards a new level.

1.3. Working principles and development of a Li-ion battery

A Li battery cell is composed of the positive and negative electrodes that are separated by the electrolyte solution which has appreciable ionic conductivity to be capable of driving Li ion transfer across the electrodes under the certain chemical potential difference. Chemical reactions in either of the electrodes liberate electrons out, letting them pass through a current collector towards the external circuit. When the cell is discharged, the Li ions flow from the negative to the positive electrode to minimize the potential difference between two electrodes. However, upon charge, the ions are forced to migrate back to the negative electrode, thus generating potential difference between the two. The electrical energy, or specifically energy density (Whg^{-1})

delivered from the chemical reaction is the function of the cell potential (V) and specific capacity ($Ahkg^{-1}$). A Li ion battery has demonstrated by far the best performance with the highest energy density out of all types of commercial battery systems known to exist.[8]

Before the discovery of a Li ion battery in 1972, a battery community initially considered Li metal, being the most electropositive as well as the lightest metal, to be the most suitable replacement for Ni-Cd and Pb-based batteries.[9-10] However, a soon found safety issue owing to dendritic growth of Li metal during cycling has made the research gradually put more emphasis on the ionic rather than the metallic character of Li. Hence, the host materials for Li ion insertion replaced Li metal, to be subsequently paired up with high-potential insertion positive electrodes like transition metal oxides. Taking nearly two decades from a concept to commercialization, the new-generation Li-ion cell was finally realized with the creation of a graphite - Lithium cobalt oxide (LCO) cell, as also schematically shown in Figure 1.1. More than 20 years since its first appearance, this cell is still being used in many of today's portable electronics.

Since its discovery, there has been tremendous interest in improving the performance (i.e. potential or energy density) of the Li ion battery by scrutinizing over all possible transition metal oxide candidates for both positive and negative electrodes. Many Li-alloyed transition metal oxides ($LiMO_x$, M = Co, Ni, Mn, and Fe) that are structured in spinel have been intensively studied for positive electrodes.[11-13] With controlled tuning of redox potentials via incorporation of poly-anions like phosphate (PO_4^{3-}) was discovered a more customized positive electrode like olivine $LiFePO_4$[14-15], which is currently considered very promising for the next-generation Li-ion cell. The important criteria when searching for an anode material are low potential relative to Li, high specific capacity, and cyclability. With regards to specific capacity, no anode can surpass Si, which has a theoretical capacity of 4200 $mAhg^{-1}$ when fully lithiated to $Li_{4.4}Si$. This value easily

overpasses specific capacity of conventional graphite (372mAhg^{-1}), even exceeding that of Li metal (3600mAhg^{-1}). However, charging of Si involves large volumetric expansion (~400%)[16] that leads to the fracture of a neighboring current collector and induces a large drop in specific capacity over the course of cycling. In fact, anodes like Si, Ge, and Sn that operate via *alloying/dealloying reaction* upon electrochemical cycling heavily suffer from capacity fading due to a large volume change and the formation of unstable secondary phases.[16-19] As an alternative to the system above, anodes like transition metal binary compounds that operate via *conversion reaction* have also been studied. The reaction involves full reduction of a binary compound to metal nanoparticles before they get embedded in a newly formed Li-binary compound matrix. The main advantage of a such reaction is high reversibility upon discharge since a considerably large interfacial surface between nanoparticles and the matrix after charging is conducive to fast decomposition of the matrix upon applying reverse polarity.[20] However, the downside of a such reaction is large cycling hysteresis generated by the difference in a reaction pathway between charge and discharge. Hence, low coulombic efficiency induced by severe polarization loss still remains the fundamental problem with no effective solution. Despite all the advantages that they have, both *alloying/dealloying reaction* and *conversion reaction* face challenges that are too formidable for commercial use. In this regard, anodes with the third type of reaction, that is *insertion/deinsertion reaction*, have been widely considered due to their high coulombic efficiency and capacity retention, despite their low specific capacity range (120-330 mAhg^{-1}). Besides the conventional carbonaceous materials like Graphite, there is another class of *insertion/deinsertion reaction* materials, titanium oxide (TiO_2) systems, that have been considered promising as Li ion battery anodes for their unparalleled chemical and structural stability.

1.4. Nanostructured engineering of TiO_2 anodes

The two important requirements for commercialization as a Li ion battery anode are its availability for mass production and environmental friendliness. In this context, TiO_2 is good since it has excellent chemical stability and relative easiness for cost-efficient fabrication. When applied as a Li ion battery anode, a volumetric change of TiO_2 is limited to only 4%[21-22];this suggests the outstanding structural stability for prolonged cycling. Furthermore, a relatively high working potential (1.5-1.8 V vs. Li)[23] hampers any unstable solid-electrolyte interphase (SEI) layers to form, further contributing to battery stability. All TiO_2 polymorphs including rutile, bronze, and anatase follow the same reaction path that can typically be expressed as following:

$$TiO_2 + xLi^+ + xe^- \rightarrow Li_xTiO_2$$

where a positive Li ion basically compensates Ti^{3+} in the original Ti^{4+} lattice by taking one electron. It has been known that except a bronze polymorph, this induces phase transition depending on its ionic concentration in the reaction.

Unfortunately, the maximum attainable capacity of bulk TiO_2 upon Li insertion is only half of the a full theoretical capacity 330 $mAhg^{-1}$ because Li-Li repulsion impedes Li ion mole fraction in Li_xTiO_2 to go beyond 0.5.[24] Furthermore, low ionic and electronic conductivity of bulk TiO_2 result in very low energy density.[25] Hence, to alleviate such problems, nanostructured engineering of TiO_2 has been proposed to not only enhance the intercalation density but also improve cycling characteristics. By greatly reducing the scale of the operating system to nanometers, lithium ions with much smaller diffusion length can be less kinetically confined. Furthermore, a high surface area of the nanostructured TiO_2 promotes more active chemical

reactions between Li ions and TiO_2. Ultimately, these not only boost the specific capacity but also increase the rate capability of a TiO_2 system. Until recent, many papers on various TiO_2 polymorphs have reported dramatic improvement in their performance as anodes by synthesizing them into various nanostructured forms.

Many electrochemical studies on rutile TiO_2 nanoparticles have focused on the effects of nanostructuring on their specific capacity. According to Hu et al., there is an order of magnitude difference in the charge capacity between micro-sized and nano-sized nanoparticles.[26] A more systematic study on this subject suggested the inverse relationship between the particle size and the charge capacity.[27] Not surprisingly, a similar effect has also been demonstrated for rutile nanowires[28] and nanotubes[29]. Since the surface effects upon Li intercalation is much larger than that of a bulk, a significant amount of Li stored at the surface of the rutile nanostructure greatly contributes to the storage capacity and, thus, makes the size dependence of its specific capacity more dramatic.[30-31] For anatase TiO_2 nanostructures, many studies on its size dependence of specific capacity have been done under different annealing temperatures because the crystallite size is dependent on this temperature[32-33] Similar to that of a rutile polymorph, its size and specific capacity has demonstrated inverse relationship. However, as opposed to a rutile structure with which the capacity retention is also strongly size-dependent, the anodic cyclability bears no relationship with the crystallite size in the case of an anatase.[34] In fact, regardless of the size, its cyclability is well maintained above 90%. To further improve its specific capacity while maintaining cyclability close to 100%, another morphology like a nanotube[35-36] was also considered. A TiO_2 nanotube has shown superior performance with well-maintained specific capacity of nearly 270 $mAhg^{-1}$ at 1C due to additional Li intercalation and accommodation of volumetric expansion through the inner core of the nanotube.

Nanostructured engineering of bronze polymorph of a TiO_2 (TiO_2-B) has demonstrated the most promising results with its specific capacity exceeding those of the above mentioned polymorphs. Li mole fraction upon full intercalation into TiO_2-B NWs, for example, is 0.91, which is equivalent to the specific capacity of 305 $mAhg^{-1}$.[37-38] What is more impressive than the high capacity is extremely high rate capability; even at discharge rate of 2000 mAg^{-1}, the specific capacity remains above 100 $mAhg^{-1}$.[38] This remarkable feature of TiO_2-B is stemmed from its large b-axis open channels that act as sub-surfaces for Li ion intercalation via non-faradaic, surface redox process.[39] Hence, this surface charge transfer and storage mechanism, also known as a pseudocapactive behavior, allows fast charge-discharge rate capability of a TiO_2-B anode.[40] Obviously, an increased surface area of TiO_2-B upon nano-structuring further contributes to enhancement of its property. To better exploit this unique surface phenomenon, various other morphologies such as nanoflowers,[41] nanosheets,[42] and nanoparticles[43] have also been actively considered.

1.5. TiO_2 coating for nanostructured anodes

In addition to the electrochemical studies of nanostructured TiO_2 as an anode material, there has been a significant work on utilizing TiO_2 polymorphs as a coating layer on various high-performance Li ion battery anodes like SiO[44], $Li_4Ti_5O_{12}$[45], and ZnO[46]. This is because the electrical conductivity of nanostructured TiO_2 increases significantly under a certain degree of Li insertion. This provides effective conduction paths to the anode and ultimately enhances its electrochemical reversibility.[44-45,47-48] Another reason is its excellent thermal stability upon SEI formation reaction between Li and the anode. According to the work by Jeong et al.[44], the

outstanding thermal stabilization of a SiO anode upon lithiation can be achieved by TiO_2 coating by restraining any exothermic reaction between lithiated SiO and the electrolyte even at high temperature;this cannot be expected from more conventionally used carbon coating. Thermal stability over the wide temperature range is critical for the safety of a rechargeable Li ion cell.

Although there have been intensive characterization works on electrochemical properties of the various polymorphic TiO_2-related nanostructures, there has been a lack of extensive experimental studies on structural transformation of TiO_2 upon Li ion intercalation as most works rely heavily on theoretical predictions. A handful of experimental papers on this subject is based on bulk structural characterization techniques such as X-ray photoelectron spectroscopy (XPS), X-ray absorption near-edge structure (XANES), and X-ray diffraction (XRD), all of which do not present clearly but rather are only suggestive of Li ion intercalation behaviors within the TiO_2 hosts. Studying such behaviors requires *in-situ* high-resolution characterization like transmission electron microscopy (TEM), which this dissertation uses extensively to directly probe Li ion dynamics within TiO_2-related anodes.

1.6. Objectives and organization of the dissertation

The primary objective of this thesis is to demonstrate the capability of *in-situ* TEM to investigate the functionality of various nanostructures involving TiO_2 polymorphs as host anode materials for Li ion battery. As a nano-sized probe tool, TEM is capable of atomically resolving any local, nano-scale structural changes associated with Li ion migration into the host, thereby enabling the direct interpretation of all the electrochemical activities within TiO_2-related anodes. All the model samples studied in this work will be synthesized and prepared for TEM in different forms

and manners. By investigating all the nano-scale morphological changes associated with Li migration within the nanostructures, this dissertation aims to obtain better understanding of the Li ion dynamics under various structural forms and bonding environments of TiO_2. The work strongly relates itself to a structural stability aspect of TiO_2 nanostructures, as a mean to explore the possibility of its use as the next-generation Li ion battery anodes.

The dissertation is organized as follows: Chapter 2 explains primarily the experimental techniques for TEM and STEM, and auxiliary spectroscopy tools. Chapter 3 discusses about a lithiation mechanism, specifically multi-step phase transformation, of a rutile TiO_2 NW. Chapter 4 and 5 discuss TiO_2-B and its Ca-modified variant, $CaTi_5O_{11}$ (Ca:TiO_2-B), which can act as a template for high-quality TiO_2-B growth. Due to the novelty of single crystalline thin-film forms of TiO_2-B and Ca:TiO_2-B, the whole Chapter 4 is dedicated in detail the STEM characterization of the atomic structure of defects and interfaces of these films before considering the in-situ Li intercalation experiments. The chapter fully discusses TiO_2-B and Ca:TiO_2-B films grown on (100) and (110) $SrTiO_3$ substrates. In chapter 5 performs electrochemical lithiation on one of the films studied in Chapter 4, (001) TiO_2-B grown on a (100) substrate, mainly focusing on its strain relaxation mechanism upon Li insertion. Chapter 6 specially looks into the use of rutile TiO_2 crystallites as the semi-inert coating material for a high performance anode material like Si to investigate the effect of TiO_2 coating on both a lithiation behavior and a final morphology of Si. Finally, aconclusion in chapter 7 summarizes all the findings from the current works and proposes the future works, some of which have preliminary results presented in the appendix.

1.7. **References**

1. US Energy Information Administration, *Monthly Energy Review* (2014)

2. Renewable Energy Policy Network for the 21st Century, *Renewables 2014: Global Status Report* (2014)

3. S. Shafiee, E. Topal, "When will fossil fuel reserves be diminished?", *Energ. Policy* **37** 181-189 (2009)

4. International Energy Agency, *Key World Energy Statistics* (2014)

5. M. C. Beard, J. M. Luther, A. J. Nozik, "The promise and challenge of nanostructured solar cells", *Nat Nano* **9** 951-954 (2014)

6. B. Dunn, H. Kamath, J.-M. Tarascon, "Electrical Energy Storage for the Grid: A Battery of Choices", *Science* **334** 928-935 (2011)

7. Frost & Sullivan, *2020 Vision: Global Lithium-Ion Battery Market* (2014)

8. J. M. Tarascon, M. Armand, "Issues and challenges facing rechargeable lithium batteries", *Nature* **414** 359-367 (2001)

9. H. Ikeda, T. Saito, H. Tamura, *Proc. Manganese Dioxide Symp.* **1** (1975)

10. M. S. Wittingham, "Electrochemical energy storage and intercalation chemistry ", *Science* **192** 1126-1127 (1976)

11. A. S. Arico, P. Bruce, B. Scrosati, J.-M. Tarascon, W. van Schalkwijk, "Nanostructured materials for advanced energy conversion and storage devices", *Nat. Mater.* **4** 366-377 (2005)

12. K. Mizushima, P. C. Jones, P. J. Wiseman, J. B. Goodenough, "LixCoO_2 ($0<x\leq1$): A new cathode material for batteries of high energy density", *Mater. Res. Bull.* **15** 783-789 (1980)

13. M. M. Thackeray, W. I. F. David, P. G. Bruce, J. B. Goodenough, "Lithium insertion into manganese spinels", *Mater. Res. Bull.* **18** 461-472 (1983)

14. N. Ravet, J. B. Goodenough, S. Besner, M. Simoneau, P. Hovington, M. Armand, *Abstract #127*, 196th ECS Meeting, Honolulu, HI, (1999)

15. M. Takahashi, S. Tobishima, K. Takei, Y. Sakurai, "Characterization of $LiFePO_4$ as the cathode material for rechargeable lithium batteries", *J. Power Sources* **97–98** 508-511 (2001)

16. H. Wu, Y. Cui, "Designing nanostructured Si anodes for high energy lithium ion batteries", *Nano Today* **7** 414-429 (2012)

17. X. H. Liu, L. Q. Zhang, L. Zhong, Y. Liu, H. Zheng, J. W. Wang, J.-H. Cho, S. A. Dayeh, S. T. Picraux, J. P. Sullivan, S. X. Mao, Z. Z. Ye, J. Y. Huang, "Ultrafast Electrochemical Lithiation of Individual Si Nanowire Anodes", *Nano Lett.* **11** 2251-2258 (2011)

18. X. H. Liu, S. Huang, S. T. Picraux, J. Li, T. Zhu, J. Y. Huang, "Reversible Nanopore Formation in Ge Nanowires during Lithiation–Delithiation Cycling: An In Situ Transmission Electron Microscopy Study", *Nano Lett.* **11** 3991-3997 (2011)

19. L. Y. Beaulieu, K. W. Eberman, R. L. Turner, L. J. Krause, J. R. Dahn, "Colossal Reversible Volume Changes in Lithium Alloys", *Electrochem. Solid-State Lett.* **4** A137-A140 (2001)

20. J. Cabana, L. Monconduit, D. Larcher, M. R. Palacín, "Beyond Intercalation-Based Li-Ion Batteries: The State of the Art and Challenges of Electrode Materials Reacting Through Conversion Reactions", *Adv. Mater.* **22** E170-E192 (2010)

21. M. Wagemaker, G. J. Kearley, A. A. van Well, H. Mutka, F. M. Mulder, "Multiple Li Positions inside Oxygen Octahedra in Lithiated TiO_2 Anatase", *J. Am. Chem. Soc.* **125** 840-848 (2002)

22. D. Deng, M. G. Kim, J. Y. Lee, J. Cho, "Green energy storage materials: Nanostructured TiO_2 and Sn-based anodes for lithium-ion batteries", *Energy Environ. Sci.* **2** 818-837 (2009)

23. V. Aravindan, Y.-S. Lee, R. Yazami, S. Madhavi, "TiO_2 polymorphs in 'rocking-chair' Li-ion batteries", *Materials Today* In press (2015)

24. G. Nuspl, K. Yoshizawa, T. Yamabe, "Lithium intercalation in TiO_2 modifications", *J. Mater. Chem.* **7** 2529-2536 (1997)

25. X. Su, Q. Wu, X. Zhan, J. Wu, S. Wei, Z. Guo, "Advanced titania nanostructures and composites for lithium ion battery", *J Mater Sci* **47** 2519-2534 (2012)

26. Y. S. Hu, L. Kienle, Y. G. Guo, J. Maier, "High Lithium Electroactivity of Nanometer-Sized Rutile TiO_2", *Adv. Mater.* **18** 1421-1426 (2006)

27. C. Jiang, I. Honma, T. Kudo, H. Zhou, "Nanocrystalline Rutile TiO2 Electrode for High-Capacity and High-Rate Lithium Storage", *Electrochem. Solid-State Lett.* **10** A127-A129 (2007)

28. B. Han, S.-J. Kim, B.-M. Hwang, S.-B. Kim, K.-W. Park, "Single-crystalline rutile TiO_2 nanowires for improved lithium ion intercalation properties", *J. Power Sources* **222** 225-229 (2013)

29. D. Liu, P. Xiao, Y. Zhang, B. B. Garcia, Q. Zhang, Q. Guo, R. Champion, G. Cao, "TiO_2 Nanotube Arrays Annealed in N_2 for Efficient Lithium-Ion Intercalation", *J. Phys. Chem. C* **112** 11175-11180 (2008)

30. C. Jiang, E. Hosono, H. Zhou, "Nanomaterials for lithium ion batteries", *Nano Today* **1** 28-33 (2006)

31. A. Stashans, S. Lunell, R. Bergström, A. Hagfeldt, S.-E. Lindquist, "Theoretical study of lithium intercalation in rutile and anatase", *Phys. Rev. B* **53** 159-170 (1996)

32. A. K. Rai, L. T. Anh, J. Gim, V. Mathew, J. Kang, B. J. Paul, J. Song, J. Kim, "Simple synthesis and particle size effects of TiO_2 nanoparticle anodes for rechargeable lithium ion batteries", *Electrochim. Acta* **90** 112-118 (2013)

33. V. Subramanian, A. Karki, K. I. Gnanasekar, F. P. Eddy, B. Rambabu, "Nanocrystalline TiO_2 (anatase) for Li-ion batteries", *J. Power Sources* **159** 186-192 (2006)

34. J. W. Kang, D. H. Kim, V. Mathew, J. S. Lim, J. H. Gim, J. Kim, "Particle Size Effect of Anatase TiO_2 Nanocrystals for Lithium-Ion Batteries", *J. Electrochem. Soc.* **158** A59-A62 (2011)

35. D. Pan, H. Huang, X. Wang, L. Wang, H. Liao, Z. Li, M. Wu, "C-axis preferentially oriented and fully activated TiO_2 nanotube arrays for lithium ion batteries and supercapacitors", *J. Mater. Chem. A* **2** 11454-11464 (2014)

36. W. Wei, G. Oltean, C.-W. Tai, K. Edstrom, F. Bjorefors, L. Nyholm, "High energy and power density TiO_2 nanotube electrodes for 3D Li-ion microbatteries", *J. Mater. Chem. A* **1** 8160-8169 (2013)

37. A. R. Armstrong, G. Armstrong, J. Canales, P. G. Bruce, "TiO_2-B Nanowires", *Angew. Chem. Int. Ed.* **116** 2336-2338 (2004)

38. A. R. Armstrong, G. Armstrong, J. Canales, R. García, P. G. Bruce, "Lithium-Ion Intercalation into TiO_2-B Nanowires", *Adv. Mater.* **17** 862-865 (2005)

39. V. Augustyn, P. Simon, B. Dunn, "Pseudocapacitive oxide materials for high-rate electrochemical energy storage", *Energy Environ. Sci.* **7** 1597-1614 (2014)

40. A. G. Dylla, G. Henkelman, K. J. Stevenson, "Lithium Insertion in Nanostructured TiO_2(B) Architectures", *Acc. Chem. Res.* **46** 1104-1112 (2013)

41. Z. Zhang, Z. Zhou, S. Nie, H. Wang, H. Peng, G. Li, K. Chen, "Flower-like hydrogenated TiO_2(B) nanostructures as anode materials for high-performance lithium ion batteries", *J. Power Sources* **267** 388-393 (2014)

42. A. G. Dylla, P. Xiao, G. Henkelman, K. J. Stevenson, "Morphological Dependence of Lithium Insertion in Nanocrystalline TiO_2(B) Nanoparticles and Nanosheets", *J. Phys, Chem. Lett.* **3** 2015-2019 (2012)

43. Y. Ren, Z. Liu, F. Pourpoint, A. R. Armstrong, C. P. Grey, P. G. Bruce, "Nanoparticulate TiO_2(B): An Anode for Lithium-Ion Batteries", *Angew. Chem. Int. Ed.* **51** 2164-2167 (2012)

44. G. Jeong, J.-H. Kim, Y.-U. Kim, Y.-J. Kim, "Multifunctional TiO2 coating for a SiO anode in Li-ion batteries", *J. Mater. Chem.* **22** 7999-8004 (2012)

45. Y.-Q. Wang, L. Gu, Y.-G. Guo, H. Li, X.-Q. He, S. Tsukimoto, Y. Ikuhara, L.-J. Wan, "Rutile-TiO2 Nanocoating for a High-Rate Li4Ti5O12 Anode of a Lithium-Ion Battery", *J. Am. Chem. Soc.* **134** 7874-7879 (2012)

46. J.-H. Lee, M.-H. Hon, Y.-W. Chung, I.-C. Leu, "The effect of TiO2 coating on the electrochemical performance of ZnO nanorod as the anode material for lithium-ion battery", *Appl. Phys. A* **102** 545-550 (2011)

47. R. van de Krol, A. Goossens, E. A. Meulenkamp, "Electrical and optical properties of TiO2 in accumulation and of lithium titanate Li0.5TiO2", *Journal of Applied Physics* **90** 2235-2242 (2001)

48. G. Du, N. Sharma, V. K. Peterson, J. A. Kimpton, D. Jia, Z. Guo, "Br-Doped Li4Ti5O12 and Composite TiO2 Anodes for Li-ion Batteries: Synchrotron X-Ray and in situ Neutron Diffraction Studies", *Adv. Funct. Mater.* **21** 3990-3997 (2011)

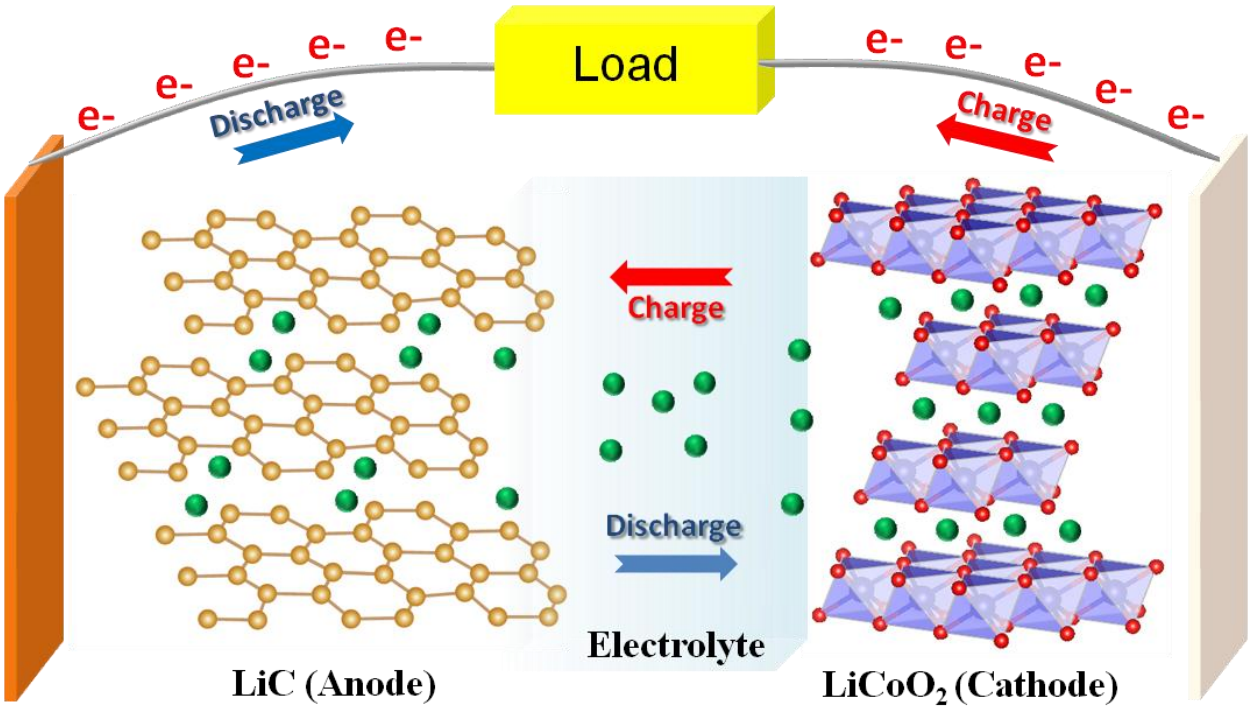

Figure 1.1 A representation of a Li ion battery similar to that developed by Sony based on insertion-deinsertion reaction upon electrochemical charge and discharge**.**

Chapter 2. Experimental Techniques

2.1. Overview

This dissertation work involves primarily the electrochemical characterization of TiO_2 polymorphs grown into different structural forms. For each of these systems, we performed the systematic study that correlates three different basis of materials science - that is structure, properties, and performance.[1] Prior to discussing the results obtained from each study, it is essential to go through the experimental set-ups and techniques that are extensively used in synthesizing and characterizing various forms of TiO_2 polymorphs. Hence, this chapter is dedicated to providing a such overview. More details about each of these techniques, if necessary, will be included within the experimental procedure part of each of their relevant chapters.

2.2. Characterization Techniques

2.2.1 Transmission Electron Microscopy

All the material systems that will be discussed in this thesis are within the order of nanometers and can only be characterized with instruments that accommodate such a scale. The structural characterization of these systems, however, are performed on an Angstrom (1×10^{-10} m) level since it is the scale of interatomic bonds of the atomic unit cells and crystal lattice

structure that constitute various kinds of material systems.[2] It is also the scale that can provide better physical understanding of the material properties from a structural perspective.

The transmission electron microscope (TEM) is the most practical atomic-scale characterization tool available for local probing and imaging of the crystal. It involves an electron beam interaction with the thin material specimen. Since electrons are accelerated by several hundred kilo-volts in TEM, the effective wavelength of the electron beam, according to the de Broglie equation, $\lambda = h\left[2m_e eE\left(1+\frac{eE}{2m_e c^2}\right)\right]^{-0.5}$, is approximately 0.02-0.03 Å for 200-300 keV[3], which is far below the resolution required to observe the atomic-scale features. In the following paragraph, the general TEM set-up and techniques used for the study presented in this dissertation will be introduced. For a more detailed understanding of theory and practice of TEM, the textbooks written by Fultz and Howe[4] and by Williams and Carter[3], can be referred.

TEM is composed of three major components - an electron gun, electromagnetic lenses, and detectors. High-energy electrons start off by accelerating from the electron gun toward the specimen, pass through an aligned lens system that defines configuration of an electron beam, and finally reach a detector to be collected after interacting with the specimen. Various types of lenses and apertures near those lenses determine the modes of TEM operation, depending on how an electron beam probes the specimen and what elemental and crystallographic information needs be obtained.

A most widely used mode of operation is conventional TEM (CTEM) - that is also performed in this dissertation work - uses a parallel illumination system with which all electron rays are formed parallel to the optic axis before reaching a specimen by the condenser lens system and

finally focused onto an objective plane within the objective lens system. The electron beams then are diffracted by the specimen towards a specimen image plane and the back focal plane. Both intermediate and projector lens systems can be functional to focus the beam on either of the two planes to obtain either an image or a diffraction pattern from a selected region. In conjunction with these lenses, apertures are often inserted to limit and select only the portion of the total electrons emitted from the source. Hence, they give the control over the resolution of an image and a diffraction pattern and the image contrast. The image resolution is determined by the size of a condenser aperture, located within the condenser lens system, before the selected portion of an electron beam is impinged upon the specimen for probing. However, in choosing the imaging resolution (smaller aperture allowing a fewer electrons) needs to sacrifice the imaging signal (larger aperture allowing more electrons). An additional artifact such as the Airy disk blur that reduces image resolution upon insertion of a smaller aperture also needs to be considered. An objective aperture is located at the back focal plane which contains the diffraction pattern of the specimen. This allows the aperture to select a certain diffraction to be used to form an image, and this is known as a 'diffraction-contrast image'. By either using a center diffraction spot (from a direct beam) or any other diffraction spot (from a diffracted beam), either a bright-field (BF) or a dark-field (DF) mode of imaging can be performed. Another main aperture, selected area aperture, that is located in the image plane can be used to choose rays on a specific area of interest to generate a diffraction pattern. Another TEM mode besides CTEM mode is high-resolution TEM (HRTEM) mode, also known as 'phase-contrast imaging mode', which is associated with the interference of the electron waves after diffracted from the specimen. It is closely related to the phase change of the electron wave by a specimen and the objective lens.

HRTEM provides detailed information about the atomic-scale features including atom arrangements near various types of defects.

In addition to CTEM and HRTEM, a large portion of a thesis work is devoted onto the use of scanning TEM (STEM) for profound chemical analysis of the materials. In STEM mode, the condenser lens system ensures the electron rays from the source converged onto a specimen to generate a point that acts as a movable "probe" that can be rastered across the specimen. Then, the signal generated from the scanned region of the specimen gets collected to the detector for a certain time period to be displayed pixel-by-pixel onto a computer screen as a raster image. Indeed, each of the electron detectors used in STEM mode is responsible for collecting as much electrons scattered off or transmitted through the atomic columns as possible at various angles, and the most frequently used ones are high-angle annular dark field (HAADF) detector and bright field (BF) detector. The HAADF detector is responsible for collecting *incoherent* elastically-scattered electrons at high angles (i.e. Rutherford scattering) and helps generate the imaging contrast with which its intensity is proportional to atomic number (Z) of a probed atom (i.e. $I \propto Z^2$).[5] HAADF imaging in STEM, hence, is alternatively known as Z-contrast imaging. All the *coherent* elastically scattered electrons at low angles (i.e. Bragg scattering) that are responsible for diffraction contrast will be neglected as they fall within the inner diameter of the HAADF detector with a large collection angle. This implies that HAADF imaging is not influenced by the artifacts (i.e. thickness contrast, bending contour, etc) and diffraction contrast (i.e. defects) but is based solely on the contrast from the mass and thickness of the specimen. Another imaging mode, that is BF imaging, will not be discussed in this thesis since the data based on this technique are not used much in this study. The schematics of a STEM is illustrated in the Figure 2.1.

In reality, electromagnetic lenses that are essential to various TEM/STEM modes of operation suffer through imperfection that greatly limits the imaging resolution. One consequence for having a lens defect is spherical aberration (C_S) that accounts for off-axis rays in a lens field behaving differently; the rays further away from the optic axis bend back towards the axis more strongly than the ones close to the optic axis. The variation in focal power within different areas of the lens due to this imperfect geometry forbids all rays converging into a single spot and creates 'disk of least confusion', thus limiting the lens resolution. To solve such a problem, a C_S-corrector has been developed over the past decades[6] to achieve the ability to resolve atomic columns and identify single atoms, thus making imaging more informative.

For the works presented in this thesis, several TEM/STEM microscopes were employed for different modes of microscopy. For CTEM/HRTEM operation, a JEOL JEM-3011 HRTEM, operated at 300 kV, was used. For high-resolution STEM operation, two Cs-corrected STEMs - JEOL JEM-2100F STEM and JEOL JEM-3100R05 AEM - operated at 200 kV and 300kV respectively were used. The point-to-point resolutions for the two STEMs are 0.10 nm and 0.055nm, respectively. All the microscopy works were performed at the University of Michigan Electron Microbeam Analysis Laboratory (EMAL).

2.2.2 Spectroscopy in the Transmission Electron Microscope

Although high-resolution images of the specimen taken with TEM/STEM entail a lot of crystallographic information about the material of interest themselves, the spectroscopy in conjunction with imaging is still needed for proper chemical profiling of the elements and compounds within the specimen. Both X-ray energy dispersive spectroscopy (XEDS) and

electron energy loss spectroscopy (EELS) enable a detailed chemical analysis of a single or a group of atoms that constitute the specimen, but each having both advantages and disadvantages of its own.

XEDS uses the ionized radiation of a high-energy electron that bombards onto the specimen and ejects an inner electron from the core of the atom nucleus. This induces an electron transition by having an electron weakly bound to an outer shell fall onto a hole in a core. This transition process generates a X-ray emission that can be a characteristic of a particular element. Despite most elements from the periodic table can be mapped out using XEDS, the detection of lighter elements like B, C, N, and O is somewhat inefficient and limited by the detector window. Another practical problem associated with XEDS is the low collection efficiency of X-rays. Despite that the total solid angle of characteristics X-ray scattering is 4π steradian, only the small fraction of X-ray (in the range of 0.03-0.3 steradian) can be collected using a detector due to its geometrical limitation. The collection angle is limited because the upper pole piece of the objective lens gets in the way of the detector window, making the detector difficult to approach near the region within the specimen and tilt to higher angles. The tilting angle of the detector needs to be compromised since the spurious signals from the specimen holder can be shown from the X-ray detection at a lower angle.

Another spectroscopy technique used for chemical analysis in this work is EELS. When a high energy electron impinges upon and interacts inelastically with an atom from the specimen, it loses its energy to the specimen before it continues down through the TEM column. The bombardment of a beam electron with an inner electron near the core of an atom (i.e. bound to K, L, M, etc., shells) gives enough energy to ionize an inner electron to have it completely extracted or transitioned into an higher unoccupied shell. The characteristic signal from this ionization loss,

also known as an EELS edge, presents the information about an individual element or ion in the material. The affected beam electrons continue their way down passing the entrance aperture through the drift tube and are spread out by the surrounding magnetic prism before being focused onto the detector (a CCD or a photodiode). In this thesis work, the PEELS spectrometer developed by Gatan, Inc (known as Gatan Imaging Filter or simply GIF) that has a 2D slow-scan CCD detector was used. In EELS, spatial resolution is important to obtain the high-intensity ionization-edge spectrum and is dependent on the penetration thickness of a specimen. Hence, a thin specimen is preferred since thinner the specimen, less the degree of the inelastic scattering of the beam electrons, and thus more electrons can pass through the entrance aperture and contribute to the EELS edge. A thicker specimen causes more scattering of electrons to induce multiple plasmon events to generate more intense low-loss plasmon peaks that can potentially dampen out all other important peaks. Another factor that affects EELS spatial resolution is carbon contamination that occurs as the focused high energy beam probe decomposes carbon within the TEM column to have it deposited onto the specimen. Despite the difficulty of the specimen preparation (i.e. thin, clean specimen), however, EELS is extremely powerful, especially when studying the local chemistry of the small region of interest (i.e. off-stoichiometry defects). This is true for many elements except for some that produce high energy EELS edges that are more difficult to collect. Since the difference in the orbital energy of an atom is related to a different bonding state with another neighboring atom, each EELS edge of an atom arising from the excitation loss should be distinct from one another. If monochromated, EELS can be even more powerful with higher energy resolution that can resolve more peaks and generate more information on, for example, the oxidation state of the element at different bonding environments.[7]

In this work, both XEDS and EELS were used interchangeably depending on the element of interest and the information needed from it. However, for the most part, EELS was preferentially used for detecting a Li signal and identifying the oxidation state of TiO_2, and, hence, only EELS work is presented in this thesis. With the help of advanced STEM, an extremely fine sub-angstrom probe was used to perform atomic-scale XEDS and EELS to determine any fine structures on a very local region. For this work, both EELS and XEDS were performed under the microscope JEOL JEM-2100F and JEOL JEM-3100F using a XEDS detector developed by EDAX and a EELS system (GIF) by Gatan.

2.2.3 In-situ electrochemical testing under TEM

What is even more impressive than simply characterizing as-grown samples is to gain capability to alter the specimen environment while performing the atomic-scale characterization inside a TEM. Hence, this so-called *in-situ* microscopy is an extremely powerful technique that offers dynamic information of the specimen under various external stimuli including an electrical bias, optical illumination, mechanical stress, and heating.[8] As appealing as all other commercially available TEM holders with *in-situ* capabilities, the *in-situ* TEM-STM holder is capable of applying an electrical bias to perform electrical measurement and observe structural changes of any nano-scale devices.[9-11] This holder consists of a conductive STM tip drivable by a piezo-motor on one side and a fixed metal rod for specimen loading on the other. After making a fine contact between a STM tip and a specimen loaded onto a metal rod, a voltage bias can be applied externally through a STM tip to the specimen that is grounded on one side to take time-integrated current measurement. Using this holder, much work has been done on many promising lithium

ion battery anodes for their structural characterization by simply coating Li metal onto a STM tip and inducing Li ion migration toward the anode material via electrical biasing.[12-13] Unfortunately, the holder does not have any property testing capability as in the *in-situ* electrochemistry TEM holder equipped with a microfluidic cell. However, HRTEM imaging can easily be performed with the TEM-STM holder because it does not have a cell window that seals off a liquid electrolyte from affecting vacuum and greatly disturbs the electron beam. Details on the *in-situ* TEM electrochemical testing set-up for the lithium ion cell will be dealt in subsequent chapters.

2.3. Sample preparation

2.3.1 Materials Synthesis and Thin Film Deposition

A. Growth of Nanowires[a]

Rutile TiO_2 nanowires were prepared by the hydrothermal method, which begins with synthesis of titanium tetraiospropoxide (TTIP). A substrate coated with TTIP dissolved in a solvent was initially mixed with a precursor, rinsed, and dried for several times before annealing it at high temperature to produce a thin TiO_2 layer on it. Then, TTIP stirred into the acid and water was placed inside an autoclave with a coated substrate to be heated for many hours before cooling it to room temperature. For the growth of rutile TiO_2-coated Si nanowires, Si NWs were first fabricated on a n-Si wafer via an electroless etching method. Then, TiO_2 coating was done via atomic layer deposition by introducing TTIP and O_2 as sources.

[a] Growth of all the NWs was performed by Alireza Kargar from Deli Wang's group in University of California-San Diego.

B. Thin film deposition

TiO_2-B thin film growth was done by pulsed laser deposition (PLD), which is a fine scale epitaxial growth technique for a thin film.[b] PLD uses high power laser pulses focused onto the surface of the ablation target, which in this study was TiO_2. This starts an ablation event by producing a plasma plume that blows rapidly off from the surface of the target and builds up on a heated substrate as a thin film. More details on growth of a TiO_2-B film will be dealt in Chapters 4 and 5.

2.3.2 Transmission Electron Microscopy Specimen Preparation for TEM/STEM Imaging

NW TEM specimens were prepared by scraping a copper TEM grid with a carbon support (Structure Probe, Inc, and Ted Pella, Inc) against the NWs grown on a substrate to pull off a few NWs.

Cross-sectional thin film specimens for TEM were prepared by mechanical polishing. Thin films were first glued to the sacrificial silicon wafers with M-Bond 610 epoxy (Vishay Precision Group) before being segmented into several pieces by a diamond cutter. Then, a single cut piece was placed on a wedge-polishing tool (Precision TEM, Inc), thinned, and fine-polished against diamond lapping films (Southbay Technology, Inc.) of varying grit sizes before being glued with a molybdenum ring (Structure Probe, Inc) with M-Bond 610 epoxy. The details of a mechanical polishing procedure is illustrated in Figure 2.2. The polished cross-sectional pieces were then

[b]Kui Zhang in our (Xiaoqing Pan's) group performed the PLD growth of all the TiO_2-B thin films. For the details of the growth technique, his thesis needs to be referred.[14]

ion-milled under Ar gas for finer polishing using a Precision Ion Polishing System (Gatan, model 691 and model 695).

2.3.3 Transmission Electron Microscopy Specimen Preparation for in-situ TEM

Preparation for a cross-sectional thin film specimen for *in-situ* TEM experiments is similar to that for TEM imaging, except that it is glued onto a half-cut Mo ring. This is a necessary measure to ensure a STM tip motion is not interrupted by a Mo ring when it approaches the film surface inside TEM. This half ring attached with a specimen is then attached onto a specially designed Cu post using a silver conductive epoxy (Ted Pella, Inc) for loading onto a TEM-STM holder.

For preparation for a NW specimen for *in-situ* TEM, a tinned Cu wire finely polished to 0.25mm in diameter (a dimension equivalent to that of a specimen-loading metal rod of a TEM-STM holder) was cut sharply with scissors. A sharp end of the wire then is wetted with a silver conductive epoxy (Ted Pella, Inc) before the light contact with the NW batch to have a couple of NWs transferred from a substrate onto a Cu wire. (See Figure 2.3)

2.4. References

1. W. D. Callister, *Materials Science and Engineering: An Introduction*, 7th, John WIley & Sons, Inc. (2007)

2. G. S. Rohrer, *Structure and Bonding in Crystalline Materials*, 1st, Cambridge University Press (2001)

3. D. B. Williams, C. B. Carter, *Transmission Electron Microscopy*, 2nd, Springer (2009)

4. B. Fultz, J. M. Howe, *Transmission Electron Microscopy and Diffractometry of Materials*, 3rd, Springer (2008)

5. S. J. Pennycook, "Structure determination through Z-contrast microscopy", *Advances in Imaging and Electron Physics* **123** 173-206 (2002)

6. P. W. Hawkes, "Aberration correction past and present", *Philos. Trans. A* **367** 3637-3664 (2009)

7. O. L. Krivanek, J. P. Ursin, N. J. Bacon, G. J. Corbin, N. Dellby, P. Hrncirik, M. F. Murfitt, C. S. Own, Z. S. Szilagyi, "High-energy-resolution monochromator for aberration-corrected scanning transmission electron microscopy/electron energy-loss spectroscopy", *Philos. Trans. A* **367** 3683-3697 (2009)

8. P. J. Ferreira, K. Mitsuishi, E. A. Stach, "In Situ Transmission Electron Microscopy", *MRS Bull.* **33** 83-90 (2008)

9. J.-Y. Chen, C.-L. Hsin, C.-W. Huang, C.-H. Chiu, Y.-T. Huang, S.-J. Lin, W.-W. Wu, L.-J. Chen, "Dynamic Evolution of Conducting Nanofilament in Resistive Switching Memories", *Nano Lett.* **13** 3671-3677 (2013)

10. D.-H. Kwon, K. M. Kim, J. H. Jang, J. M. Jeon, M. H. Lee, G. H. Kim, X.-S. Li, G.-S. Park, B. Lee, S. Han, M. Kim, C. S. Hwang, "Atomic structure of conducting nanofilaments in TiO_2 resistive switching memory", *Nat. Nanotechnol.* **5** 148-153 (2010)

11. Y. Yang, P. Gao, S. Gaba, T. Chang, X. Pan, W. Lu, "Observation of conducting filament growth in nanoscale resistive memories", *Nat. Commun.* **3** 732 (2012)

12. X. H. Liu, J. Y. Huang, "In situ TEM electrochemistry of anode materials in lithium ion batteries", *Energy Environ. Sci.* **4** 3844-3860 (2011)

13. X. H. Liu, Y. Liu, A. Kushima, S. Zhang, T. Zhu, J. Li, J. Y. Huang, "In Situ TEM Experiments of Electrochemical Lithiation and Delithiation of Individual Nanostructures", *Adv. Energy Mater.* **2** 722-741 (2012)

14. K. Zhang, *Ph. D. Thesis*, "Epitaxial $CaTi_5O_{11}$ and TiO_2-B Thin Films for High Rate Lithium-Ion Batteries", Materials Science and Engineering, University of Michigan, (2014)

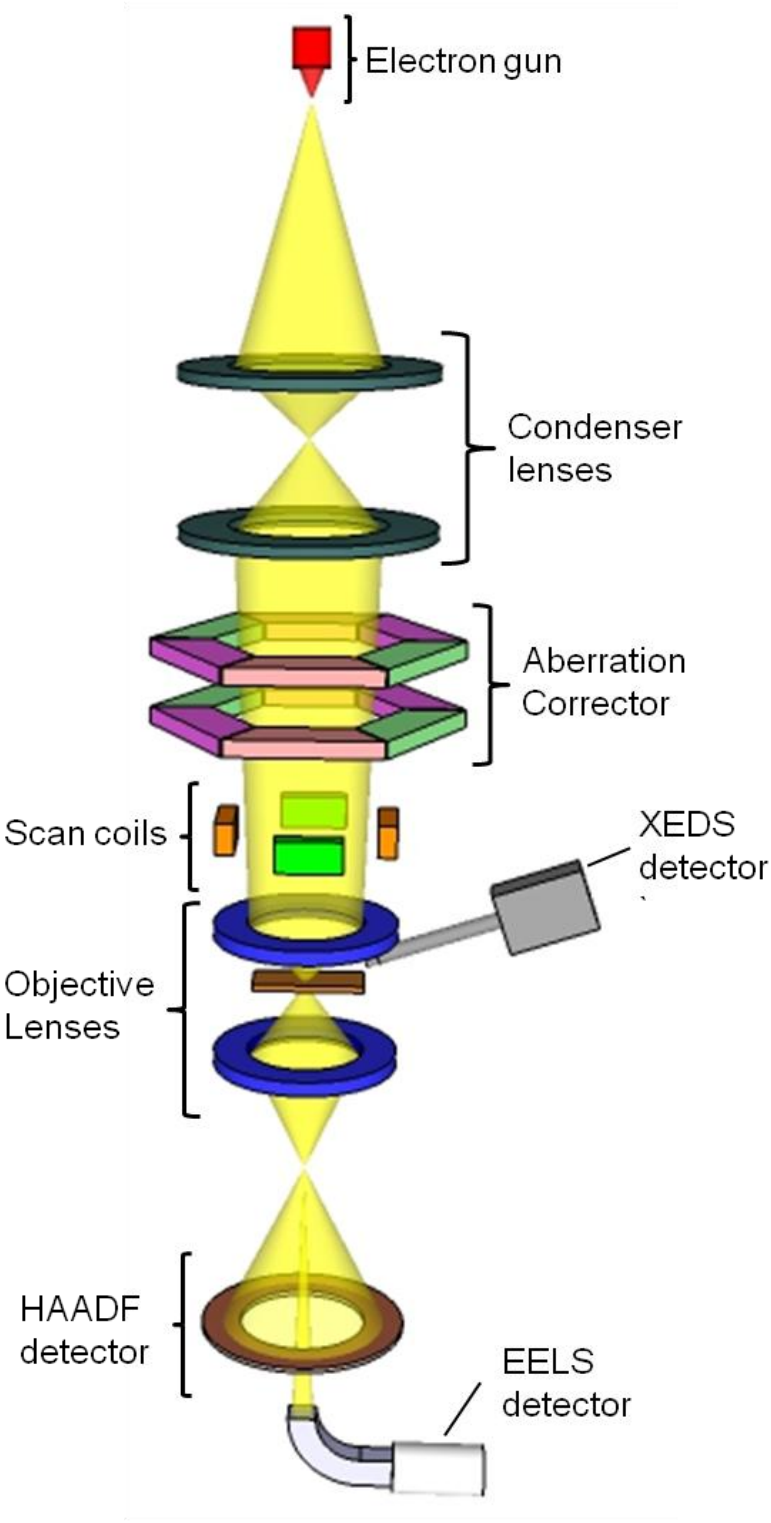

Figure 2.1 Schematics of STEM with relevant components for specimen characterization

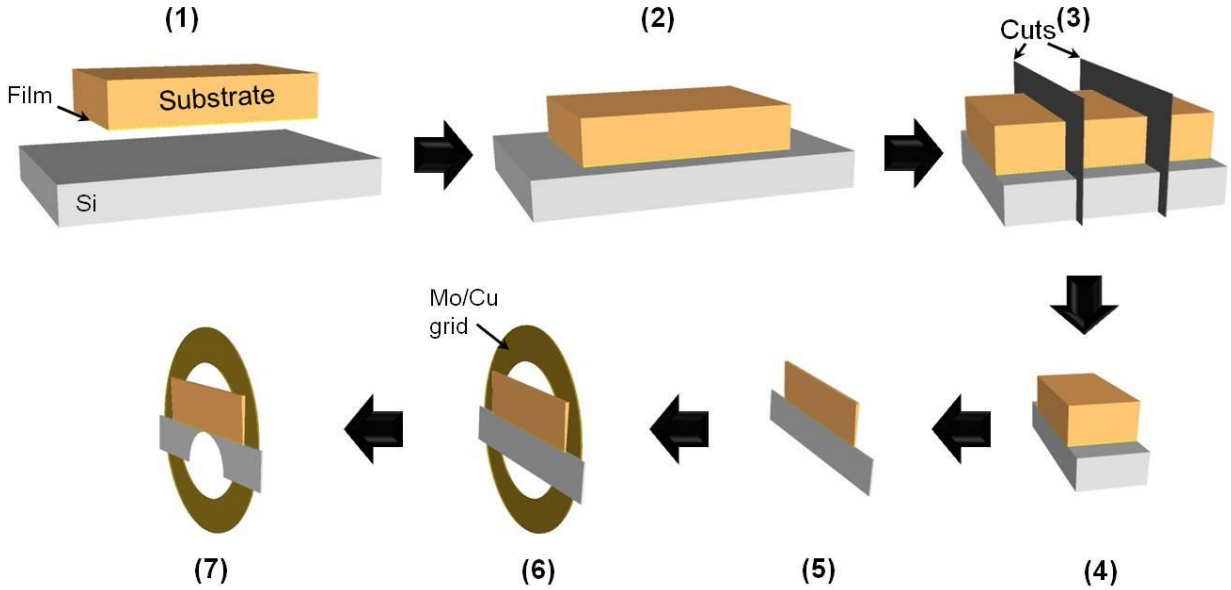

Figure 2.2 A schematic illustrating the various steps involved in cross-sectional preparation of the TEM specimen. (1) The film side of the specimen is glued to a sacrificial Si piece (2) before the glued piece gets stayed on the hot plate for 3-4 hours for curing of a glue layer. (3,4) The glued piece is cut into smaller pieces and (5) then flat-polished on both sides into a wedge shape before (6) it gets glued to a Mo ring for finer ion milling. (7) The ion milling stops as the hole formed in Si upon fine thinning reaches the film side. At this point, the TEM specimen is ready for examination under TEM.

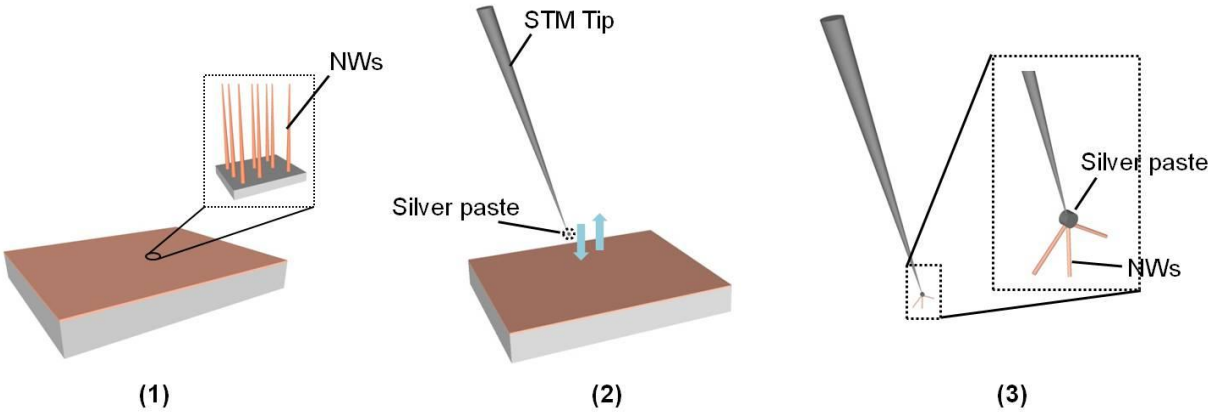

Figure 2.3 A schematic illustrating the various steps involved in preparation of a NW specimen for in-situ TEM. (2) A STM tip soaked with a silver paste on the edge is pressed against the NWs on a substrate to pull out some NWs from the substrate. (3) After pulling out NWs, the silver paste that connect NWs to the STM tip is let dry in air or put on a hot plate for better adhesion between NWs and the STM tip.

Chapter 3. Phase transformation mechanism of a rutile TiO_2 NW upon lithiation

3.1. Introduction and Background

Over the past decade, inorganic oxide semiconductors have attracted tremendous interest for the possible exploitation of their profound material chemistry. Amongst many oxides, rutile TiO_2 has received attention because of its application in the field of lithium ion batteries as an anode that acts as a low-voltage lithium intercalation host.[1-4] Since the extent of intercalation is limited in the bulk material, nanostructured rutile TiO_2 has been considered for shortening transport lengths of Li ions and for effective strain relaxation, thus providing more undisrupted Li ion migration channels. In fact, recent studies demonstrate the superior performance of nano-sized rutile TiO_2, with specific charge capacity 4–5 times greater than that of micro-sized (bulk) materials[5-8] and excellent capacity retention.[8-10]

In view of the dramatic increase in the extent of lithium intercalation provided by the nano-scale material, it would be of considerable interest to learn more about the details of its structure. In a series of theoretical studies, the possible existence of an intermediate phase transition, rutile-to-monoclinic Li_xTiO_2 upon lithium insertion of $x \sim 0.5$, has previously been reported,[11-13] and it has been speculated that this could be a major factor contributing to irreversible charge capacity loss

upon cycling. Some studies of TiO_2 have also suggested that the fully lithiated form, Li_xTiO_2 ($x \sim 0.8$), has a hexagonal structure that is energetically more favorable than the rutile form.[12] This view is supported by *ex situ* X-ray diffraction (XRD), transmission electron microscopy (TEM) and selected-area electron diffraction (SAED) results,[5-6] though others have argued that $LiTiO_2$ has either the rock-salt or spinel structure,[2,7,9,14] depending on the dimensions of the structure, and that the hexagonal phase does not exist. In fact, the situation is ambiguous since the peak or ring positions in XRD and SAED of hexagonal and rock-salt phases are strikingly similar. More importantly, these experimental studies are potentially influenced by exposure of the material to the atmosphere. Obviously, a definitive experiment is needed to resolve these matters, and in this chapter, the electro-chemical testing of a single-crystal rutile TiO_2 nanowire (NW) within a high-resolution transmission electron microscope (TEM) was reported, thus, offering direct proof of the actual structural transitions that occur upon Li ion insertion and cycling.

3.2. Experimental Procedures

A batch of rutile TiO_2 NWs with varying sizes was grown *via* a hydrothermal method, as explained in Chapter 2 and also reported elsewhere.[15] High-resolution transmission electron microscopy (HRTEM) and scanning transmission electron microscopy (HRSTEM) images of TiO_2 NWs were taken using JEOL JEM-3010F and aberration-corrected JEOL-JEM2100F transmission electron microscopes, operating at accelerating voltages of 300kV and 200kV, respectively.

A TEM specimen was prepared by embedding NWs in Ag-based paste on a Cu post. A prepared specimen was loaded onto a single-tilt in-situ Nanofactory Instruments TEM-STM holder to be part of an electro-chemical cell assembly as an anode in a JEOL JEM-3010F microscope. Bulk Li metal, as a counter-part, was scrapped onto a tungsten STM tip that was loaded on a piezo-drive of the holder inside the glove box. A naturally formed Li_2O layer on the Li metal from the 3-6 sec exposure to air during transportation from an Ar-filled bag into the TEM column, acted as a solid electrolyte that allows transport of Li ions but not electrons. (Figure 3.1) A piezo-movement supporting the W tip (an *in situ* STM–TEM holder) attached with NWs can be controlled with great precision, allowing a single NW to be contacted within the TEM, thus completing the assembly of an electro-chemical cell. Electrical biasing of the assembly was provided by a Keithley 2635A source meter.

3.3. Results and Discussion

The morphology of an as-grown single-crystalline rutile TiO_2 NW is shown in HRTEM and HRSTEM images in Figure 3.2. From the SAED shown in the inset of Figure 3.2b, the long dimensions of the NWs are found to be along the *c*-direction. Based on theoretical results, Li ions are expected to migrate *via* tetrahedral sites along *c*-axis channels. The calculated Li ion diffusion coefficient is 10^{-6} cm^2 s^{-1} along the *c* direction *versus* 10^{-15} cm^2 s^{-1} along either the *a* or *b* direction.[16] Hence, within the as-grown NWs for this study, Li ion migration is expected to be very mobile and efficient along their length, largely free of kinetic limitations normally observed in poly-crystalline nanostructures with non-homogenous channels that are usually tested, thus favoring Li insertion and extraction during *in situ* electrochemical testing

within the TEM. Another advantage of having a single-crystal NW is unambiguous spot-pattern identification of the phase using SAED, which should be free of multiple ring patterns found in poly-crystalline nanostructures.

Then, electro-chemical cycling was done on a NW using a standardized bias cycle, varying the electrical input for insertion of Li ions into and extraction from it to resemble the standard cyclic voltammetry testing of a bulk cell. Before cycling, the NW was first lightly lithiated by applying a potential sweep of −5 to 0 V with respect to the Li counter-electrode at a rate of 2 V s^{-1}. Then the NW was tested with continuous bias cycling, first with delithiation (0 to 5 to 0 V), then lithiation (0 to −5 to 0 V) at a rate of 2 V s^{-1}. This cycle scheme was adopted instead of a conventional fixed-voltage lithiation (and delithiation) process in order to limit the quantity of Li ions moving into the single nanostructure and thus prevent the NW from becoming fully lithiated at this stage. After multiple electro-chemical cycles, the morphological change of the rutile TiO_2 NW was examined by TEM, which revealed a clear structural transformation, accompanied by volumetric expansion, as shown in Figure 3.3. Compared to the pristine TiO_2 NW, the lateral (a-b directions) expansion is at least 140 %, with a slight longitudinal (c direction) contraction of 97 %. The total volumetric expansion of the NW is thus approximately 120 %. Along with lateral expansion, the NW also twisted sharply. SAED taken on the NW confirms that there has been a structural change of the NW from rutile (*P*42/*mnm*) to monoclinic (*P2/m*). The remnant peaks in the SAED pattern are from primitive rutile, implying that the physical contact made between the Li-coated tip and the NW was not uniform enough to cause Li ions to be inserted through all available c-channels into the NW. A similar test was conducted on another rutile TiO_2 NW close to the zone axis [100] to verify this phase transformation (Figure 3.4). Both low- and high-magnification images clearly show that there is lattice expansion of a rutile TiO_2 NW upon

intermediate phase transformation ($TiO_2 \rightarrow Li_xTiO_2$). The measured lattice spacings (d(202)) for TiO_2 and Li_xTiO_2 are 0.248nm and 0.250nm, respectively, the difference of which is slightly larger than that theoretically calculated. (d_{101} for TiO_2 and Li_xTiO_2 are 0.2487nm and 0.2489nm) The SAED study of the NW before and after just two cycles clearly demonstrates the emergence of a new, distinct pattern overlapping the primitive pattern from the rutile phase (Figure 3.5). Simulation of the diffraction confirms that this pattern is, in fact, coming from a monoclinic phase.

The structural deformation observed agrees well with recent theoretical calculations on lithiation of rutile TiO_2.[11-13] As Li ions are inserted into tetrahedral sites along open c-channels, neighboring Ti ions get repelled away from their initial positions.[13] This distortion lowers crystal symmetry, which changes from tetragonal to monoclinic, with highly anisotropic expansion of a- and b-lattice constants and slight contraction of c-lattice constant. This phase transformation of rutile TiO_2 to monoclinic Li_xTiO_2, predicted to happen near x~0.5, can be regarded as an intermediate phase transformation since it is not reversible under conditions that should lead to extraction of Li ions from the TiO_2 NW. Sharp twisting and bending of the NW is likely to disrupt the c-channels, potentially contributing to loss of capacity, as reported in the literature.[6,9] At this stage, no further morphology change or volumetric expansion was found to occur, even after 20 voltage cycles, indicating that the NW has remarkable structural stability under this degree of lithiation. I-V curved measured during cycling at this stage (Figure 3.6) provide evidence of reversible Li-ion insertion and extraction, though its extent is difficult to measure quantitatively. In accordance with the I-V curve, evidence of reversibility is provided by the subtle changes in overall contrast observed in the in-situ TEM images observed first with delithiation (0 to 5 to 0 V) then with lithiation (0 to -5 to 0 V). The overall dimension of the NW

under monoclinic phase remains unchanged throughout the electro-chemical cycling at this stage.

The possibility that additional structural transitions of Li_xTiO_2 might occur was explored by injecting more Li ions into the NW by applying a constant potential of -4 V for 5-6 minutes. During this lithiation process, a slow but gradual change in image contrast along the body of the structure was observed. The most noticeable change, however, was the further expansion of the NW along the a-direction. Instead of a uniform dilation, the expansion appeared in bubble-like form, indicated by a clear change in image contrast. As lithiation proceeded, multiple bubbles tended to grow along the a-direction, as shown in Figure 3.7a and c. This bubble-like dilation is a clear indication of transformation of the monoclinic NW into a new phase. The SAED pattern from the bubble matches well with the rock-salt structure (*Fm-3m*). An interesting aspect of this observation is the way in which the transformation of the NW from monoclinic to rock-salt proceeds. As Li ions are continuously injected along c-channels in the NW, they tend to accumulate near the contact between the NW and the Cu rod. When the Li content becomes high enough, it evidently raises the probability of octahedral site occupancy by Li ions, thus making the monoclinic-to-rock-salt transition more favorable. This may be why the top half of the NW remains monoclinic in structure. Another noticeable feature is the array of (200) stripes that emerge across the NW. (Figure 3.7b) This is similar to what has been observed in the lithiation of a SnO_2 NW[17] and is most likely either a tetrahedral or octahedral site filling within the monoclinic structure, reflecting a Li preference during inter-structural diffusion.

Figure 3.8 summarizes the proposed overall structural transformation upon lithiation of a rutile TiO_2 NW. After multiple cycling, the NW first irreversibly undergoes the intermediate phase transition from rutile to monoclinic structure, accompanied by large anisotropic lateral expansion and distortion. The distortion may give rise to some capacity loss due to disruption of c-channels

and preferential migration paths of Li ion within the structure, but at this stage, the NW does not undergo any further structural transformation upon continuous electro-chemical cycling that does not exceed a certain level of Li insertion. It is suspected that the functional form of nanostructured rutile titania as an anode actually has the monoclinic structure. When more Li ions are injected into the structure, the NW undergoes further transverse a-direction dilation and is able to reach its final stage of lithiation, which is a rock-salt phase. This discovery is of great importance since it is the first direct experimental proof that rutile TiO_2 nano-structures in fact undergo two-step lithiation with increasing Li-mole fraction in Li_xTiO_2.

3.4. Conclusions

To summarize the observations, electro-chemical lithiation on a single-crystal rutile TiO_2 nanowire have been performed and analyzed by constructing a nano-scale Li-ion battery within the TEM. The theoretical prediction regarding formation of an intermediate (monoclinic) phase have been somewhat verified, though we found that full lithiation in fact corresponds to yet another (rock-salt) phase. It is believed that the results presented here can expand the understanding of structural transition of the rutile TiO_2 system, the study of which has long proven to be difficult using bulk electro-chemical testing devices. These findings may lead to an improved nano-structuring of rutile TiO_2 to better accommodate anisotropy, thus optimizing its performance as a Li-ion battery anode.

3.5. References

1. B. Zachau-Christiansen, K. West, T. Jacobsen, S. Atlung, "Lithium insertion in different TiO_2 modifications", *Solid State Ionics* **28–30, Part 2** 1176-1182 (1988)

2. L. Kavan, "Lithium Insertion into Mesoscopic and Single-Crystal TiO_2 (Rutile) Electrodes", *J. Electrochem. Soc.* **146** 1375-1379 (1999)

3. D. Deng, M. G. Kim, J. Y. Lee, J. Cho, "Green energy storage materials: Nanostructured TiO_2 and Sn-based anodes for lithium-ion batteries", *Energy Environ. Sci.* **2** 818-837 (2009)

4. M. Pfanzelt, P. Kubiak, M. Fleischhammer, M. Wohlfahrt-Mehrens, "TiO_2 rutile—An alternative anode material for safe lithium-ion batteries", *J. Power Sources* **196** 6815-6821 (2011)

5. Y. S. Hu, L. Kienle, Y. G. Guo, J. Maier, "High Lithium Electroactivity of Nanometer-Sized Rutile TiO_2", *Adv. Mater.* **18** 1421-1426 (2006)

6. M. A. Reddy, M. S. Kishore, V. Pralong, V. Caignaert, U. V. Varadaraju, B. Raveau, "Room temperature synthesis and Li insertion into nanocrystalline rutile TiO_2", *Electrochem. Commun.* **8** 1299-1303 (2006)

7. E. Baudrin, S. Cassaignon, M. Koelsch, J. P. Jolivet, L. Dupont, J. M. Tarascon, "Structural evolution during the reaction of Li with nano-sized rutile type TiO_2 at room temperature", *Electrochem. Commun.* **9** 337-342 (2007)

8. C. Jiang, "Nanocrystalline Rutile TiO_2 Electrode for High-Capacity and High-Rate Lithium Storage", *Electrochem. Solid-State Lett.* **10** A127-A129 (2007)

9. D. Wang, D. Choi, Z. Yang, V. V. Viswanathan, Z. Nie, C. Wang, Y. Song, J.-G. Zhang, J. Liu, "Synthesis and Li-Ion Insertion Properties of Highly Crystalline Mesoporous Rutile TiO_2", *Chem. Mater.* **20** 3435-3442 (2008)

10. J. S. Chen, "H_2O-EG Assisted Synthesis of Uniform Urchinlike Rutile TiO_2 with Superior Lithium Storage Properties ", *ACS Appl. Mater. Inter.* **5** 9998-10003 (2013)

11. M. V. Koudriachova, N. M. Harrison, S. W. de Leeuw, "First principles predictions for intercalation behaviour", *Solid State Ionics* **175** 829-834 (2004)

12. W. J. H. Borghols, M. Wagemaker, U. Lafont, E. M. Kelder, F. M. Mulder, "Impact of Nanosizing on Lithiated Rutile TiO_2", *Chem. Mater.* **20** 2949-2955 (2008)

13. M. V. Koudriachova, "Density-functional simulations of lithium intercalation in rutile", *Phys. Rev. B* **65** 235423 (2002)

14. C. M. Wang, Z. G. Yang, S. Thevuthasan, J. Liu, D. R. Baer, D. Choi, D. H. Wang, J. G. Zhang, L. V. Saraf, Z. M. Nie, "Crystal and electronic structure of lithiated nanosized rutile TiO_2 by electron diffraction and electron energy-loss spectroscopy", *Appl. Phys. Lett.* **94** 233116 (2009)

15. H.-E. Wang, Z. Chen, Y. H. Leung, C. Luan, C. Liu, Y. Tang, C. Yan, W. Zhang, J. A. Zapien, I. Bello, S.-T. Lee, "Hydrothermal synthesis of ordered single-crystalline rutile TiO_2 nanorod arrays on different substrates", *Appl. Phys. Lett.* **96** 263104 (2010)

16. M. V. Koudriachova, N. M. Harrison, S. W. de Leeuw, "Effect of Diffusion on Lithium Intercalation in Titanium Dioxide", *Phys. Rev. Lett.* **86** 1275-1278 (2001)

17. J. Y. Huang, L. Zhong, C. M. Wang, J. P. Sullivan, W. Xu, L. Q. Zhang, S. X. Mao, N. S. Hudak, X. H. Liu, A. Subramanian, H. Fan, L. Qi, A. Kushima, J. Li, "In Situ Observation of the Electrochemical Lithiation of a Single SnO2 Nanowire Electrode", *Science* **330** 1515-1520 (2010)

18. P. G. Bruce, "Solid-state chemistry of lithium power sources", *Chem. Commun.* 1817-1824 (1997)

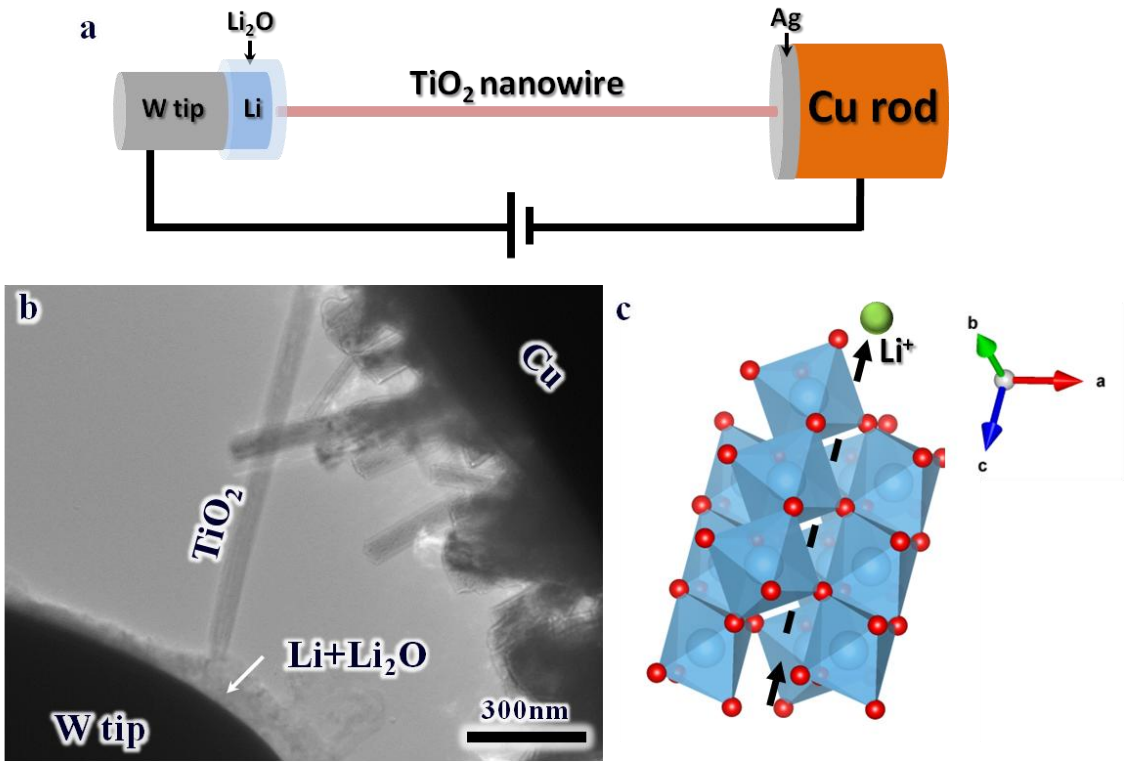

Figure 3.1 a. Schematic illustration of electrochemical set-up built inside TEM, **b.** TEM image of the set-up, and **c.** projected migration route of Li ion in a NW.

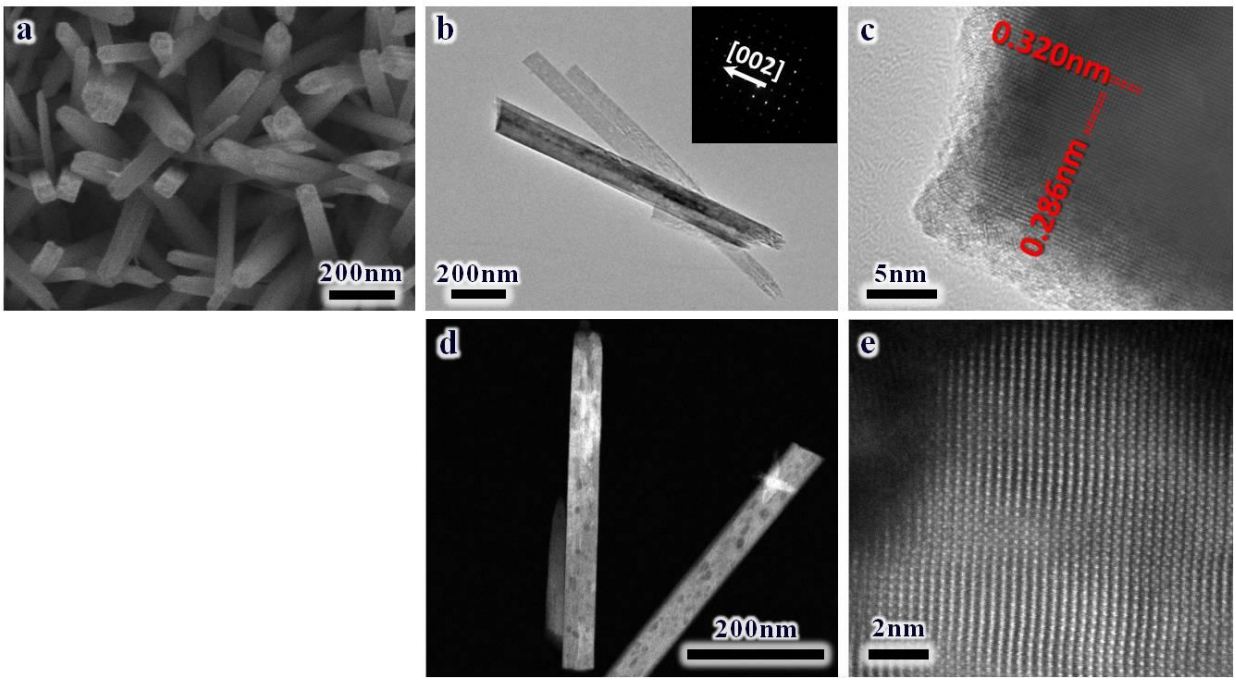

Figure 3.2 a. SEM image of rutile TiO_2 NWs grown on a fluorine-doped tin oxide substrate. **b-e.** TEM and HR-TEM images of a rutile TiO_2 NW

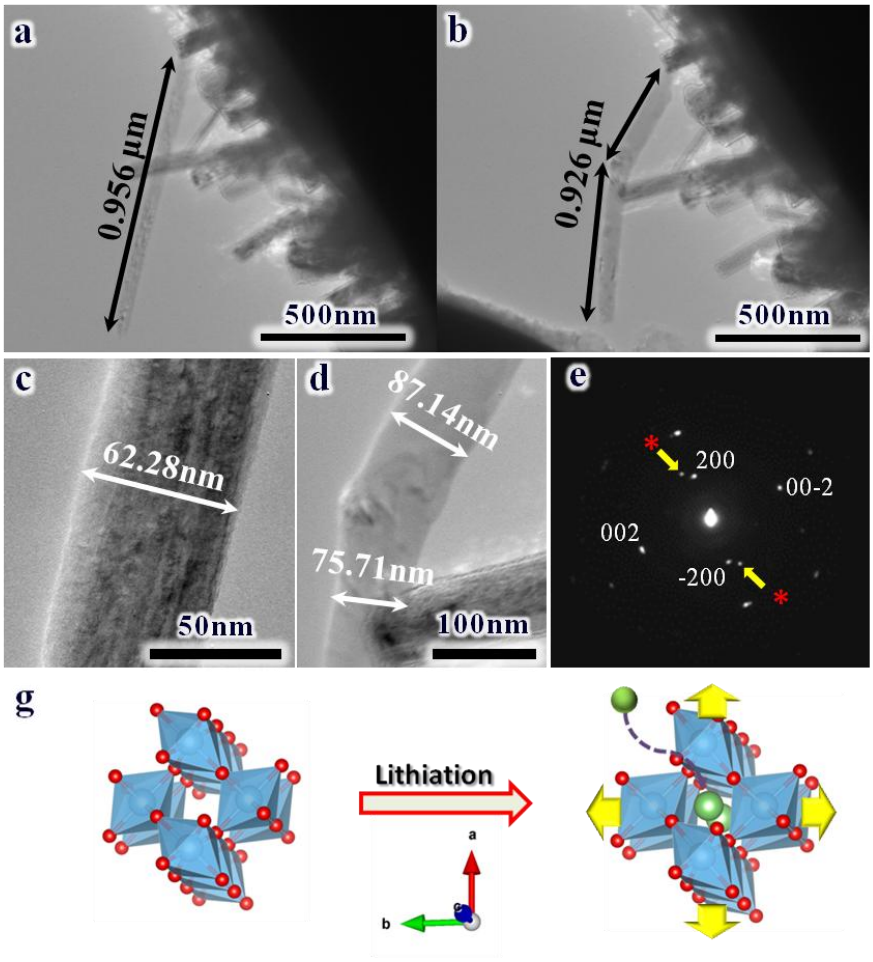

Figure 3.3 a and b. TEM images of a NW before and after transition to intermediate state, **c.** and **d.** higher magnification images of **a** and **b**, **e.** diffraction pattern from region shown in **d** (* is from the remaining rutile phase), and **g.** schematic of structural transformation of a rutile TiO_2 to monoclinic structure via intercalation of Li ion. *(Red: Oxygen, Green: Lithium, Blue: Titanium)*

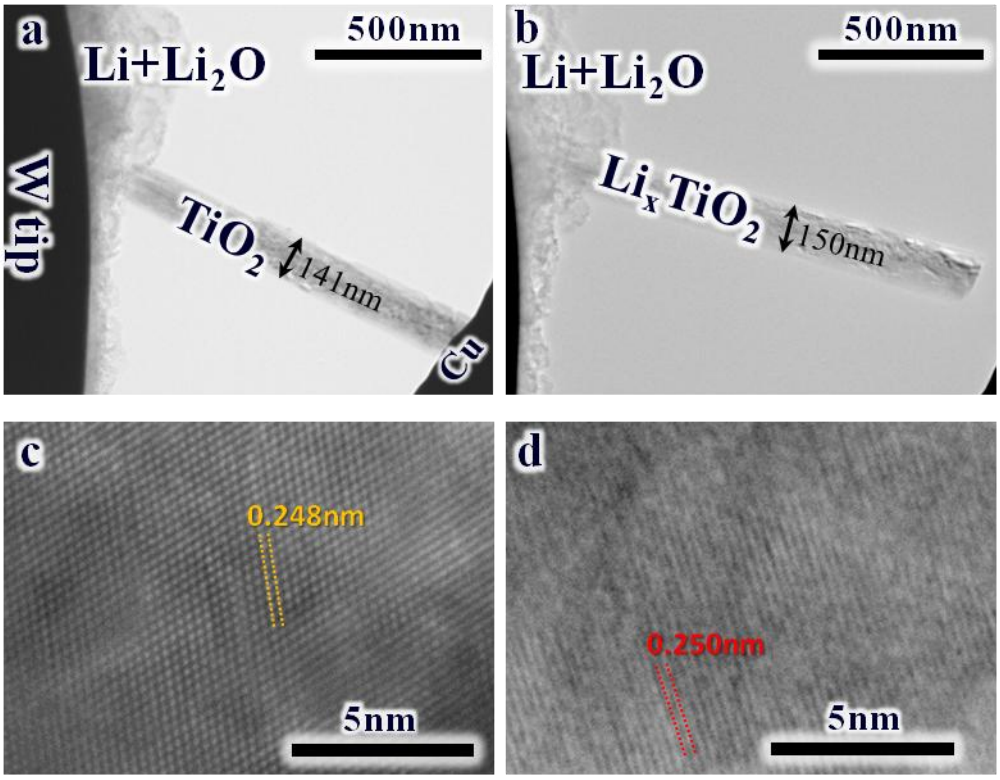

Figure 3.4 Low- and high-magnification TEM images of **a and c.** a TiO_2 NW in primitive state and **b and d.** a Li_xTiO_2 NW in transition to intermediate state.

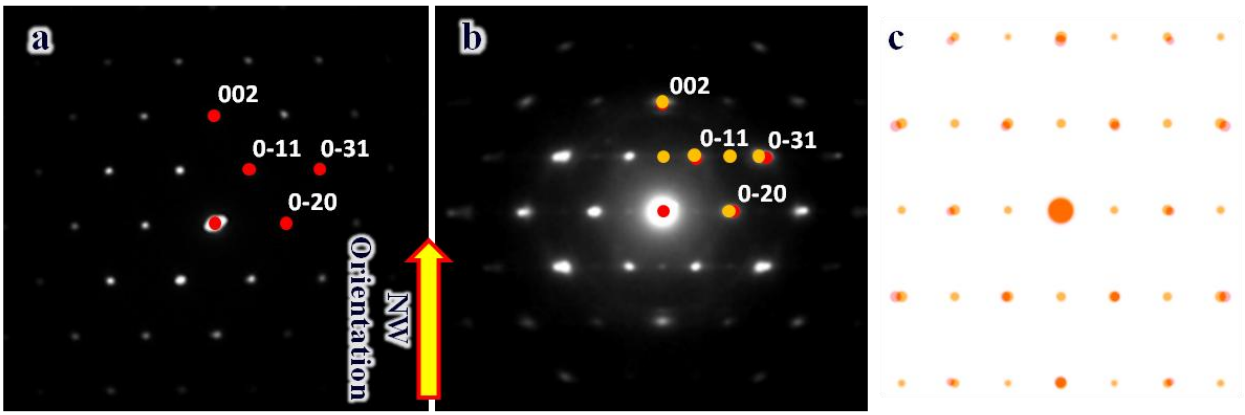

Figure 3.5 a and b. Selected area diffraction of a primitive TiO_2 NW and a Li_xTiO_2, respectively, under transition from rutile to intermediate state. Red and orange dots are the representative reciprocal spots for primitive TiO_2 and transformed Li_xTiO_2, respectively. **c.** Simulated electron diffraction pattern showing phase overlap between rutile TiO_2 and monoclinic Li_xTiO_2.

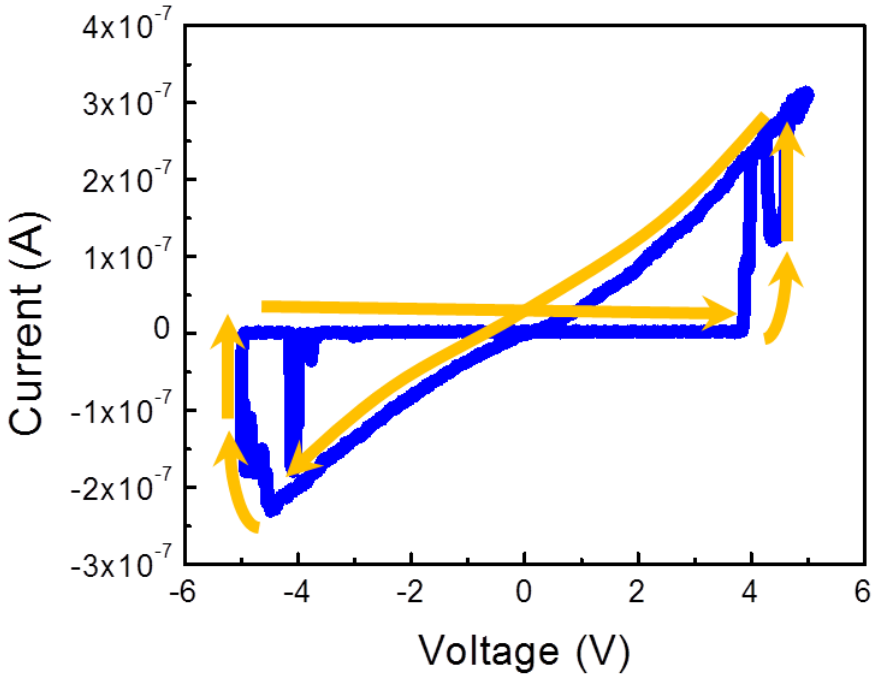

Figure 3.6 Representative graph showing the lithiation and de-lithiation behavior of the Li_xTiO_2 NW under standard voltage sweep. Lithiation (during the low-resistance branch of the voltage sweep from 0 to –5 V) of the NW (e.g., $TiO_2 + xLi^+ + xe^- \rightarrow Li_xTiO_2$) induces the NW to go through the transition from a low-resistance to a high-resistance state, while the opposite is true for de-lithiation (during the high-resistance branch of the voltage sweep from 0 to 5 V). Li-rich Li_xTiO_2 exhibits Schottky-type semiconductor behavior, while Li-deficient Li_xTiO_2 exhibits close-to-ohmic behavior, as reported in many literature references for other Li intercalation systems.[18] This transition, despite some difference in magnitude in each cycle, repeats throughout the continuous electrochemical cycling at this stage of Li intercalation.

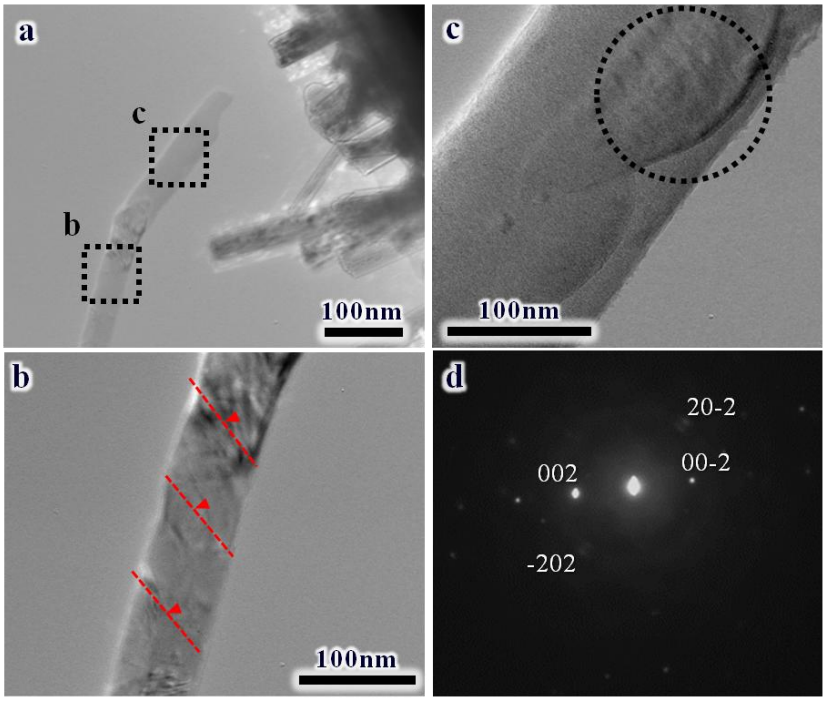

Figure 3.7 a. TEM image of a Li_xTiO_2 NW (pulled out of Cu post) after full lithiation that shows anisotropic distortion indicated by **b.** the array of stripes due to preferential insertion of lithium and anisotropic strain induced along a-plane, and **c.** side-swelling along b-direction. **d.** Diffraction pattern at the region in **c** marked by a circle.

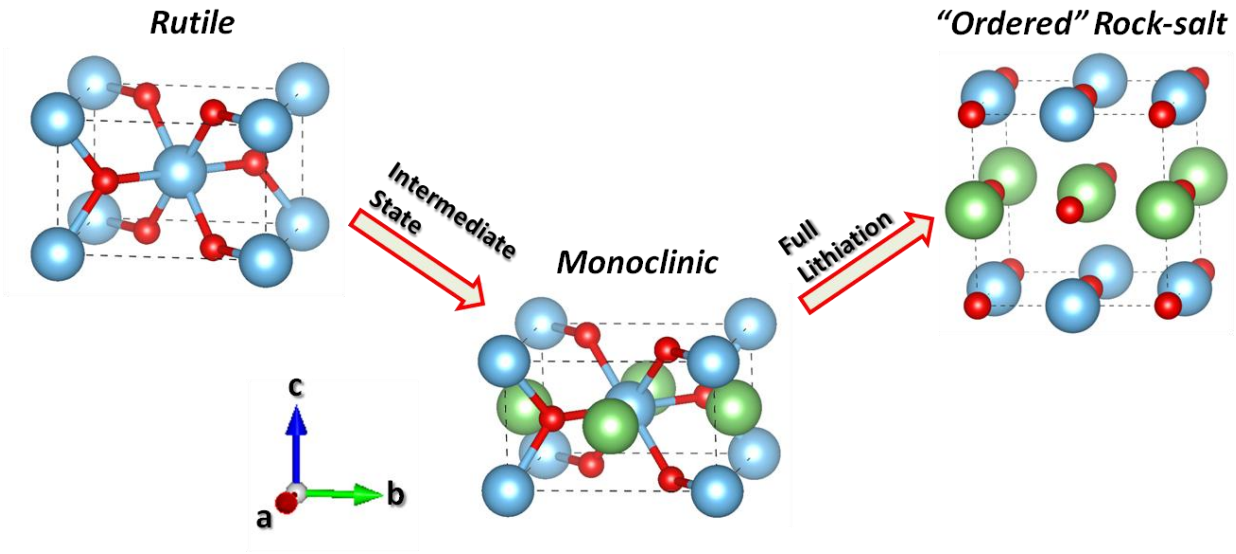

Figure 3.8 Schematics of structural transition of a rutile Li_xTiO_2 from primitive to fully lithiated phase

Chapter 4. Atomic structure of defects and interfaces in TiO_2-B and Ca:TiO_2-B ($CaTi_5O_{11}$) films grown on $SrTiO_3$

4.1. Introduction and Background

Recently, there has been tremendous interest in the bronze polymorph of TiO_2 (here designated TiO_2-B) due to its intriguing structure, which is composed of edge- and corner-sharing TiO_6 octahedra.[1-3] Compared to other polymorphs, such as anatase and rutile, bronze has the lowest density due to large, open channels suitable for diffusion of ionic species. This unique characteristic has triggered extensive study of various properties of TiO_2-B including electronic, vibrational properties[4], structural stability[5], water adsorption[6], and lithium ion transport[1-2,7-10]. Films of TiO_2-B have many possible applications, including dye-sensitized solar cells (DSSCs)[11-12] and Li ion batteries. TiO_2-B can potentially be used as a dye-absorbent for DSSCs because of its exceptional surface reactivity, comparable to that of commonly used anatase (here designated TiO_2-A)[13-14]. It has been reported that the (100) facet of TiO_2-B is less surface stable but more reactive to a dye molecule than most facets of anatase. TiO_2-B may also be used as an anode material in Li ion batteries[1-2,15-16]. Open (001) plane channels in TiO_2-B aligned parallel to [010] act as sub-surfaces for fast Li ion transport, hence, enhancing battery charging rate[17].

Although crystallographic orientation plays a critical role in device functionality, it is difficult to control the growth of TiO_2-B films due to lack of a lattice-matching substrate that can guarantee high crystallinity of the film. The use of a template layer has proven successful for single

crystalline film growth of materials with low symmetry, especially when such a layer partially satisfies an epitaxial relationship with both film and substrate.[18-19] For a material of lower symmetry, like monoclinic TiO_2-B, choices for the template layer are limited by availability of crystal types similar to that of TiO_2-B that also have a small lattice mismatch with a substrate. By identifying such a template layer, however, the film was successfully grown on $SrTiO_3$ (STO) substrates using pulsed-laser deposition (PLD). The template phase, a Ca modification to the TiO_2-B structure (here referred to as Ca:TiO_2-B) with the formula $CaTi_5O_{11}$, is composed of a Ca bonded TiO_x layer intercalated in between left c-oriented and right c-oriented TiO_2-B layers.[10] By using high-resolution transmission electron microscopy (HRTEM) and X-ray diffraction (XRD), both the c-axis growth and off-c-axis growth (tilted 45° to the substrate normal) of Ca:TiO_2-B, respectively, on (100) and (110) STO substrates have been examined. Interestingly, these films were found for their uses to serve as an anode material for a Li ion battery that exhibits high capacity and significantly enhanced rate capability.[10] More to the point, (001) Ca:TiO_2-B provides a suitable template layer for c-axis growth of high quality TiO_2-B films.

In addition to its value for optimizing film growth of the Ca:TiO_2-B phase (and the TiO_2-B phase deposited on top) along different orientations, the careful study of interfacial structures and various types of defects within the film is important since defects can potentially influence device characteristics. Hence, in the present work, using aberration-corrected scanning transmission electron microscopy (STEM), a detailed study of three sets of films was performed to discuss two main aspects: 1) interfacial structure and defects associated with the growth of Ca:TiO_2-B films on (100) and (110) STO substrates, and 2) defect structure associated with subsequent growth of a (001) TiO_2-B film on (001) Ca:TiO_2-B.

4.2. Experimental Procedures

The $CaTi_4O_9$ target used to grow Ca:TiO_2-B thin films was fabricated by mixing 80 % TiO_2 and 20 % CaO powders, sintering at 1400 ºC, and pressing a pellet under force equivalent to 10,000 lb. The TiO_2 target used to grow TiO_2-B thin films was made from pure TiO_2 powder in like manner. The vacuum chamber for PLD has a base pressure of $<10^{-7}$ Torr. A 248 nm KrF excimer laser with a pulse duration of 22 ns and a fluence of ~3.4 Jcm^{-2} was used for the film deposition at a repetition rate of 10 Hz. The target-to-substrate distance was set to 6.35 cm. All thin film deposition was done at 800 ºC in oxygen at ambient pressure of 0.05 Torr with a deposition rate of 0.01-0.02 Å/pulse. The deposited film thickness was in the range of 5-200 nm, which was measured by a Veeco Dektak profilometer and confirmed with TEM.

All high-angle annular dark field (HAADF) images were taken using a spherical aberration-corrected STEM (JEM JEOL-2100F). Cross-sectional TEM specimens were prepared via mechanical polishing and ion-milling under Ar gas at 4 kV.

4.3. Results and Discussion

4.3.1 Overview of films grown on (100) and (110) STO substrates

Films of Ca:TiO_2-B were deposited by PLD on both (100) and (110) STO substrates at 800 °C using a PLD target composed of $CaTi_4O_9$. A film of the regular TiO_2-B was subsequently deposited by PLD on the Ca:TiO_2-B film on the (100) STO substrate at 800 °C using a PLD target composed of pure TiO_2. As shown schematically in Figure 4.1a and 4.1b, growth of Ca:TiO_2-B is highly dependent on the STO orientation. Whereas growth on (100) yields a

smooth, epitaxial film that provides a good template for subsequent growth of TiO_2-B (Figure 4.2), growth on (110) initially results in a mixture of $CaTiO_3$ (here designated as CTO) and TiO_2-B at the interface, yielding a film with many more defects and a rough surface that does not support the subsequent growth of a high quality TiO_2-B film. In fact, owing to its high crystallinity, (001) TiO_2-B deposited on (100) STO was the model system used for electrochemical study under TEM as will be discussed in Chapter 5. STEM images shown in Figure 4.1c and 4.1d illustrate the features of the films grown on (100) and (110) substrates. Detailed differences and thorough analyses of interface and film structures are discussed below.

4.3.2 Interfacial structure and defects in a Ca:TiO_2-B film grown on (100) STO

For the c-axis growth of a Ca:TiO_2-B film, the titania polymorph that prefers to grow, TiO_2-A, competes with Ca:TiO_2-B to form an epitaxial interface with (100) STO. For Ca:TiO_2-B, since both in-plane *a* and *b* cell parameters are almost integer multiples of the lattice parameter of STO, the film can have either a (100) plane or a (010) plane oriented parallel to the STO surface. TiO_2-A, despite similar lattice mismatch (~3 %), exhibits a better epitaxial relationship with STO because the square-shaped arrangement of Ti atoms within its c-plane provides a cube-on-cube relationship with the similarly configured TiO_x termination of STO.[20] This characteristic naturally drives the growth of the TiO_2-A on this substrate over a wide temperature range, 600-900 °C. Hence, along either the [100] or [010] direction, the three differently configured interfaces were observed between the film and STO: (100)Ca:TiO_2-B||(100)STO, (010)Ca:TiO_2-B||(100)STO, and (100)TiO_2-A||(100)STO. Figure 4.3 shows high-resolution STEM images of these three possible interfaces between the film and (100) STO. STO substrates in all three cases

are atomically rough, in that there are several nm-wide steps with various heights, also known as surface-step terraces (SSTs), which contribute to misfit strain with the epitaxial film.[21-22] Although this is expected to generate vertical mismatch gaps at opposite ends of the SSTs due to incomplete accommodation of full unit cell stacking (Figure 4.4), the gaps were nevertheless filled by an additional vertical atomic plane during growth leading to local atomic rearrangement near the interface between the film and the substrate. This, in turn, would generate an elastic strain field near the interface, which affects the local atomic configuration of the Ca:TiO_2-B (and TiO_2-A) layer during continued growth. Based on comparison of the three different interfaces, a Ca:TiO_2-B layer does not accommodate SSTs of more than one-half unit cell high (Figure 4.3a and b) whereas a TiO_2-A layer accommodates SSTs as high as two unit cells, as shown in Figure 4.3c. In addition to the cube-on-cube in-plane symmetry it shares with STO, TiO_2-A also has good vertical matching with STO, corresponding to a 4 % mismatch. This is what enables TiO_2-A to tolerate SSTs of any width and height. On the other hand, Ca:TiO_2-B has a- and b-axis atomic configurations that are both different and have a larger vertical mismatch with STO. To tolerate even one-half unit cell surface roughness, as shown in Figure 4.3a, Ca:TiO_2-B needs to undergo local atomic ordering near the interface with STO. The first TiO_x stack that is left c-oriented (here denoted as A) suddenly changes its stacking orientation to the right c-orientation (here denoted as B) along the same plane at the one-half unit cell SST (indicated with a line on either side of the arrow in Figure 4.3a). This is due to the discontinuation of a Ca-modified TiO_x layer at the SST in order to accommodate the vertical lattice mismatch generated by this step.

Another prominent defect in the Ca:TiO_2-B film grown on (100) STO is the interphase boundary between Ca:TiO_2-B and TiO_2-A. Two of the major types of interface observed are (010)Ca:TiO_2-B||(100)TiO_2-A (Figure 4.5a) and (100)Ca:TiO_2-B||(100) TiO_2-A (Figure 4.5b). The first has a

boundary complexion that is rough but relatively sharp compared to the second, which has smooth and diffuse boundary complexion because the (100) planar surface of Ca:TiO_2-B is jagged due to repeated A- and B-orientation TiO_x stacking. Hence, despite the similar lattice mismatch in the two boundaries, the different planar surface morphology induces differently shaped interphase boundaries. A third type of interphase boundary, (100)Ca:TiO_2-B||(010)Ca:TiO_2-B (Figure 4.5d), has a complexion much more diffuse than that of (010)Ca:TiO_2-B||(100) TiO_2-A, with a width of 5-10 nm.

In addition to the vertical interphase boundaries, horizontal interphase boundaries were also observed in the Ca:TiO_2-B film. These were formed when Ca:TiO_2-B was deposited on top of an existing TiO_2-A grain. For a non-flat TiO_2-A base, two Ca:TiO_2-B grains with two different in-plane matching relationships with (001) TiO_2-A were observed. As illustrated in Figure 4.5c and 4.5d, for (100)Ca:TiO_2-B||(100)TiO_2-A, the boundary is sharp, as opposed to (010)Ca:TiO_2-B||(100)TiO_2-A, where the boundary is diffuse over a wide extent along the c-axis. Other minor defects that were observed, such as tiny grains buried inside a much larger grain along the film interface with STO, similar to a Ca:TiO_2-B grain buried inside a TiO_2-A grain, are illustrated in Figure 4.5d. These buried grains were identified in cross-sectional STEM as a lattice overlap between the small and larger grains of different phases.

4.3.3 Interfacial structure and defects in a Ca:TiO_2-B film grown on (110) STO

Distinct from the direct epitaxial growth on (100) STO, the growth of Ca:TiO_2-B films on (110) STO initially involves phase separation of Ca:TiO_2-B into two different phases, TiO_2-B and pseudo-cubic CTO before a continuous layer of Ca:TiO_2-B starts to grow. Hence, this growth is

quite unique since the film templates itself with these secondary phases. Although there has been a number of studies on the separate growth of an ultra-thin template layer of a certain phase for the successive deposition of a film of the same phase[23-24], there has not yet been any study on the naturally driven growth of a secondary phase, acting as a template for the growth of the main phase. As illustrated by the schematic (Figure 4.6a) and STEM images (Figure 4.6b and c), from each {100} facet of the triangular CTO islands on (110) STO, the growth of TiO_2-B noticeably occurred along both in-plane and out-of-plane directions, forming grain boundaries with each other and interphase boundaries with neighboring naturally grown TiO_2-A grains (Figure 4.6b and c). The volume proportion of TiO_2-A occupying the film grown on a (110) substrate is approximately 10-15 %, larger than that for the film grown on a (100) substrate (5-10 %).

The STEM image in Figure 4.7a and schematic in Figure 4.7b illustrate the possible steps involved in Ca:TiO_2-B growth on (110) STO. The growth sequence of the layers on (110) STO may be: (1) CTO + (2) TiO_2-B → (3) Ca:TiO_2-B, which is different from that on (100) STO, where Ca:TiO_2-B acts as a template layer for TiO_2-B growth. Based on high-resolution images, it seems possible that phase separation occurred via some combination of Ca and Ti atom migration, allowing epitaxially more favorable formation of the CTO structure directly on (110) STO. Since (110) STO apparently does not support the direct growth of Ca:TiO_2-B, which prefers to grow on (100), it is likely that (100) CTO induced the TiO_2-B grains to form along its [100] direction (Figure 4.8). Once a TiO_2-B layer was well established, single-crystalline $CaTiO_2$-B was able to grow along the c-axis of a TiO_2-B template layer, essentially reversing the process that occurs on (100) STO.

As mentioned above, due to the nature of its growth, this film contains many grain boundaries between the two differently oriented Ca:TiO_2-B grains and interphase boundaries formed

between the tilted grains of TiO_2-B, Ca:TiO_2-B, and TiO_2-A phases. This type of tilt boundary contains both ordered and disordered complexions, marked with a rectangle and a circle, respectively in Figure 4.9a. In the ordered region, a local, periodic atomic arrangement is present where (001) planes of alternating TiO_x layers in a Ca:TiO_2-B grain are coherently bonded to (100) planes of the adjacent TiO_2-A grain. The red dots in Figure 4.9a mark possible bonding sites for the Ti atoms from the two grains. While the ordered complexion is atomically sharp, the disordered complexion is rough, with random thickness; hence, the interphase boundary between Ca:TiO_2-B and TiO_2-A is also metastable. On the other hand, grain boundaries between Ca:TiO_2-B grains, which are more commonly found throughout the film, do not exhibit any epitaxial relation between the grains, having simply been formed via 45° inter-penetration of adjacent grains growing towards each other along their a-axes (Figure 4.9b).

Since the growth of TiO_2-B films happened on facets of small CTO islands, the interfacial strain between their (100) planes is not significant enough to induce much misfit relaxation, even if the lattice mismatch (calculated for diagonal mismatch) between pseudo-cubic CTO and TiO_2-B is close to 6 %. Nevertheless, a few of the larger sized TiO_2-B grains possess several types of c-plane stacking defects. A good example is shown in Figure 4.10a and represented schematically in Figure 4.10e, where a few Ca-modified layers are intercalated within a TiO_2-B grain, possibly due to incomplete phase separation between TiO_2-B and CTO, making a layer of Ca:TiO_2-B. In the same region was observed a sudden change in orientation of TiO_x stacking (indicated with arrows in Figure 4.10c). Possibly, this could indicate that there are missing c-planes of Ca-modified layers at those regions, and this could have resulted again from incomplete phase separation between TiO_2-B and CTO. This possibility is reasonable since this defect feature, shown in a-direction growth of Ca:TiO_2-B, is somewhat different from the case of c-growth of

Ca:TiO_2-B on (100) STO, where TiO_x layer stacking is unidirectional unless a Ca-modified TiO_x layer is present. However, despite these planar defects, since the growth of either a pure or an intermixed TiO_2-B layer happened along the a-direction from CTO, any planar defects associated with this growth do not affect the Ca:TiO_2-B growth that happens from a c-plane of TiO_2-B, so that defect-free single-crystalline grains could be grown, as shown in region 3 in Figure 4.10b.

4.3.4 Interfacial structure and defects in a TiO_2-B film grown on (001) Ca:TiO_2-B

Two main types of defects are present in a TiO_2-B thin film grown on a (001) Ca:TiO_2-B template, out-of-phase boundaries (OPBs) generated within a TiO_2-B layer and interphase boundaries that are formed between TiO_2-B and TiO_2-A grains. OPBs are stacking defects induced by off-stoichiometry, or local deficiencies (e.g., missing rows of atoms) within a given layer or from an underlying layer. These are distinct from stacking faults that usually involve syntactic intergrowth of a differently configured layer of the same atomic type.[25] Using aberration-corrected atomic scale microscopy, we confirm that the local atomic misregistry within a Ca:TiO_2-B template layer is the origin of OPBs in the TiO_2-B layer. As illustrated in Figure 4.11 and 4.12, a locally missing Ca-modified TiO_x layer in Ca:TiO_2-B stacking ultimately generates a c-axis offset equivalent of 0.42*c* (where *c* is the c-axis lattice constant of TiO_2-B) for a TiO_2-B film deposited on top. In addition to a c-axis offset, local deficiency of Ca atoms also affects the orientation of a TiO_2-B layer nucleated above, as shown schematically in Figure 4.11c and d. This is due to the unique stacking sequence of Ca:TiO_2-B that has a Ca-modified TiO_x layer changing the orientation of a TiO_x-only layer, for example, from A- to B-orientation and vice versa. Hence, the missing row of a Ca-modified TiO_x in Ca:TiO_2-B ultimately determines

the orientation of two abutting TiO_2-B layers with respect to the phase boundary during TiO_2-B growth. When the deficiency happens at the surface of a Ca:TiO_2-B layer, the resulting two abutting TiO_2-B grains will face in and out from each other (Figures 4.11a and b). However, when the missing Ca layer is in the middle of a $CaTiO_2$-B layer, a single (Figure 4.12a) or multi unit-cell surface step (Figure 4.12c) is generated at the interface with a TiO_2-B layer and may result in TiO_2-B grains oriented in the same direction. Depending on the relative orientations of the two adjacent grains, the nature and orientation of OPBs can be different. When the two grains are oriented towards or away from each other, OPBs only have short-range or no periodicity (Figures 4.11a and b). However, as in many cubic systems[26-27], when the relative orientation of the two grains is along the same axis, OPBs have long-range crystallographic periodicity (Figure 4.12). From the interface between Ca:TiO_2-B and TiO_2-B, a few mono-layers are needed for the boundary between the two TiO_2-B grains to become atomically ordered. Figure 4.12 illustrates different examples of long-range atomic ordering achieved between two TiO_2-B grains oriented along the same direction. The periodic crystallographic patterns are presented with dotted lines. In both cases, there are possible sites for Ti atoms from the two abutting grains (here, labeled as Grain 1 and Grain 2 in the schematic representations in Figures 4.12b and d) to share and form bonds. The atoms occupying these sites are presented with the two colors representative of Grain 1 and Grain 2. Even atoms that are displaced out from their original positions (Figure 4.12c) that do not seem to belong to either of the two abutting grains (area marked with red in Figure 4.12d) still have periodicity along the boundary. Another example is Ca:TiO_2-B grains having two missing Ca-modified layers near the interface between TiO_2-B and Ca:TiO_2-B with a multi unit-cell surface step (Figure 4.13a). An OPB generated in between the two grains oriented in the

same direction also has periodic crystallographic patterns again with possible sites for Ti atoms from either a left or right-side grain to occupy. (Figure 4.13b)

The local misregistry of atomic stacking within a Ca:TiO_2-B layer can be attributed to the SSTs from the STO substrate, forming an interface with the Ca:TiO_2-B template layer. The interfacial strain between STO and Ca:TiO_2-B comes not only from the difference in their in-plane lattice parameters but also from the imperfect vertical matching between unit cells of the film and the termination surface of the substrate. Another possible way to understand the local misregistry in Ca:TiO_2-B is by considering growth characteristics of a thin film. The controlled growth of a thin film (e.g., via PLD) is highly uni-directional and performed under lower temperature conditions than bulk synthesis. Because lower temperature possibly hinders surface diffusion and structural rearrangement of Ca atoms, stacking defects are generated.

The second distinct defect in a TiO_2-B film is interphase boundaries between anatase and bronze polymorphs of TiO_2 that were formed during growth. In conjunction with templated growth of TiO_2-B, some TiO_2-A grains grew simultaneously and formed a boundary with neighboring TiO_2-B and Ca:TiO_2-B, as shown in Figures 4.14a and b. The boundary consists of disordered arrays and does not exhibit any epitaxial relationships; hence, complexions arising from this boundary are most likely metastable. Looking into details, the interphase boundary between TiO_2-A and TiO_2-B grains is very sharp and uniform, with the width fluctuation from abutting phases varying only by a unit cell, whereas the boundary between TiO_2-A and Ca:TiO_2-B grains is relatively more diffuse over a wider thickness range. This qualitatively indicates that the boundary between TiO_2-A and Ca:TiO_2-B grains is more chemically unstable than between TiO_2-A and TiO_2-B grains.

Aside from these large interphase boundaries, as described above, there are small sized micro-grains of TiO_2-A sandwiched between two TiO_2-B grains, and these clearly have an epitaxial relationship with the neighboring TiO_2-B grains, as shown in Figure 4.14c. These are not stand-alone grains formed directly from the STO substrate but possibly formed as high temperature derivatives of bronze-type grains under topotactic reaction as has been reported in the literature,[28] judging from their atomic configuration. The formation of TiO_2-A grains most likely occurred via shearing of the two (-201) TiO_2-B planes along the [102] direction by 0.42*c*. After the reaction, (103) planes of a newly formed TiO_2-A grain is under epitaxy with TiO_2-B planes, forming a periodic boundary as shown in Figure 4.14d.

4.4. Conclusions

In summary, thin films of monoclinic TiO_2-B and Ca:TiO_2-B were grown on (100) and (110) cubic STO substrates in order to study the effect of substrate orientation on film morphology and the nature of defects present in the films. Aberration-corrected STEM has allowed analysis of both interfacial structure at phase boundaries and identification of a variety of interesting defect structures. Although the growth of a Ca:TiO_2-B film on the (100) substrate is highly c-oriented, the growth on the (110) substrate is affected by phase separation induced formation of the secondary phase, cubic $CaTiO_3$ that acts as a heterogeneous self-template for the crystallographically tilted growth of TiO_2-B grains. For c-axis Ca:TiO_2-B growth on a (100) substrate, SSTs at the STO surface induce local atomic ordering near the interface between Ca:TiO_2-B and STO. However, for growth on a (110) substrate, a-direction growth of a TiO_2-B layer separated from CTO induces only several planar stacking defects associated with a Ca-

modified TiO_x layer but does not affect Ca:TiO_2-B deposited along the c-axis. For c-axis TiO_2-B film growth on a (001) Ca:TiO_2-B template, out-of-phase boundaries are nucleated out of the plane with a missing Ca-modified TiO_x layer. This understanding of film growth mechanism and defect formation should provide an important step toward successful fabrication of high-performance energy devices.

4.5. References

1. A. G. Dylla, G. Henkelman, K. J. Stevenson, "Lithium Insertion in Nanostructured TiO_2(B) Architectures", *Acc. Chem. Res.* **46** 1104-1112 (2013)

2. A. R. Armstrong, G. Armstrong, J. Canales, R. García, P. G. Bruce, "Lithium-Ion Intercalation into TiO_2-B Nanowires", *Adv. Mater.* **17** 862-865 (2005)

3. R. Marchand, L. Brohan, M. Tournoux, "TiO_2(B) a new form of titanium dioxide and the potassium octatitanate $K_2Ti_8O_{17}$", *Mater. Res. Bull.* **15** 1129-1133 (1980)

4. M. Ben Yahia, F. Lemoigno, T. Beuvier, J.-S. Filhol, M. Richard-Plouet, L. Brohan, M.-L. Doublet, "Updated references for the structural, electronic, and vibrational properties of TiO_2(B) bulk using first-principles density functional theory calculations", *J. Chem. Phys.* **130** 204501 (2009)

5. A. Vittadini, M. Casarin, A. Selloni, "Structure and Stability of TiO_2-B Surfaces: A Density Functional Study", *J. Phys. Chem. C* **113** 18973-18977 (2009)

6. W. Liu, J.-g. Wang, W. Li, X. Guo, L. Lu, X. Lu, X. Feng, C. Liu, Z. Yang, "A shortcut for evaluating activities of TiO_2 facets: water dissociative chemisorption on TiO_2-B (100) and (001)", *Phys. Chem. Chem. Phys.* **12** 8721-8727 (2010)

7. C. Arrouvel, S. C. Parker, M. S. Islam, "Lithium Insertion and Transport in the TiO_2−B Anode Material: A Computational Study", *Chem. Mater.* **21** 4778-4783 (2009)

8. M.-C. Yang, Y.-Y. Lee, B. Xu, K. Powers, Y. S. Meng, "TiO_2 flakes as anode materials for Li-ion-batteries", *J. Power Sources* **207** 166-172 (2012)

9. H. Liu, Z. Bi, X.-G. Sun, R. R. Unocic, M. P. Paranthaman, S. Dai, G. M. Brown, "Mesoporous TiO_2–B Microspheres with Superior Rate Performance for Lithium Ion Batteries", *Adv. Mater.* **23** 3450-3454 (2011)

10. K. Zhang, M. B. Katz, B. Li, S. J. Kim, X. Du, X. Hao, J. R. Jokisaari, S. Zhang, G. W. Graham, A. Van der Ven, B. M. Bartlett, X. Pan, "Water-Free Titania-Bronze Thin Films with Superfast Lithium-Ion Transport", *Adv. Mater.* **26** 7365-7370 (2014)

11. C.-C. Tsai, Y.-Y. Chu, H. Teng, "A simple electrophoretic deposition method to prepare TiO_2–B nanoribbon thin films for dye-sensitized solar cells", *Thin Solid Films* **519** 662-665 (2010)

12. J. Procházka, L. Kavan, M. Zukalová, O. Frank, M. Kalbáč, A. Zukal, M. Klementová, D. Carbone, M. Graetzel, "Novel Synthesis of the TiO_2(B) Multilayer Templated Films", *Chem. Mater.* **21** 1457-1464 (2009)

13. L. Fernández-Werner, R. Faccio, A. Juan, H. Pardo, B. Montenegro, Á. W. Mombrú, "Ultrathin (001) and (100) TiO_2(B) sheets: Surface reactivity and structural properties", *Appl. Surf. Sci.* **290** 180-187 (2014)

14. L. Qi, Y. Liu, C. Li, "Controlled synthesis of TiO_2-B nanowires and nanoparticles for dye-sensitized solar cells", *Appl. Surf. Sci.* **257** 1660-1665 (2010)

15. B. Wang, H. Xin, X. Li, J. Cheng, G. Yang, F. Nie, "Mesoporous CNT@TiO_2-C Nanocable with Extremely Durable High Rate Capability for Lithium-Ion Battery Anodes", *Sci. Rep.* **4** 1-7 (2014)

16. A. R. Armstrong, G. Armstrong, J. Canales, P. G. Bruce, "TiO_2–B nanowires as negative electrodes for rechargeable lithium batteries", *J. Power Sources* **146** 501-506 (2005)

17. V. Augustyn, P. Simon, B. Dunn, "Pseudocapacitive oxide materials for high-rate electrochemical energy storage", *Energy Environ. Sci.* **7** 1597-1614 (2014)

18. T. Hamada, A. Ito, E. Fujii, D. Chu, K. Kato, Y. Masuda, "Preparation of single-crystalline ZnO films on ZnO-buffered a-plane sapphire by chemical bath deposition", *J. Cryst. Growth* **311** 3687-3691 (2009)

19. W. Guo, M. B. Katz, C. T. Nelson, T. Heeg, D. G. Schlom, B. Liu, Y. Che, X. Q. Pan, "Epitaxial ZnO films on (111) Si substrates with Sc_2O_3 buffer layers", *Appl. Phys. Lett.* **94** 122107 (2009)

20. C. K. Ong, S. J. Wang, "In situ RHEED monitor of the growth of epitaxial anatase TiO_2 thin films", *Appl. Surf. Sci.* **185** 47-51 (2001)

21. C. Ma, M. Liu, C. Chen, Y. Lin, Y. Li, J. S. Horwitz, J. Jiang, E. I. Meletis, Q. Zhang, "The Origin of Local Strain in Highly Epitaxial Oxide Thin Films", *Sci. Rep.* **3** 1-5 (2013)

22. C. R. Connell, R. E. Caflisch, E. Luo, G. Simms, "The elastic field of a surface step: The Marchenko–Parshin formula in the linear case", *J. Comput. Appl. Math.* **196** 368-386 (2006)

23. R. Takahashi, H. Misumi, M. Lippmaa, "Self-Template Growth of Orientation-Controlled Fe_3O_4 Thin Films", *Cryst. Growth Des.* **12** 2679-2683 (2012)

24. K. Zhang, S. J. Kim, Y. Zhang, T. Heeg, D. G. Schlom, W. Shen, X. Pan, "Epitaxial growth of ZnO on (1 1 1) Si free of an amorphous interlayer", *J. Phys. D: Appl. Phys.* **47** 105302 (2014)

25. M. A. Zurbuchen, W. Tian, X. Q. Pan, D. Fong, S. K. Streiffer, M. E. Hawley, J. Lettieri, Y. Jia, G. Asayama, S. J. Fulk, D. J. Comstock, S. Knapp, A. H. Carim, D. G. Schlom, "Morphology, structure, and nucleation of out-of-phase boundaries (OPBs) in epitaxial films of layered oxides", *J. Mater. Res.* **22** 1439-1471 (2007)

26. I. MacLaren, L. Wang, O. Morris, A. J. Craven, R. L. Stamps, B. Schaffer, Q. M. Ramasse, S. Miao, K. Kalantari, I. Sterianou, I. M. Reaney, "Local stabilisation of polar order at charged antiphase boundaries in antiferroelectric $(Bi_{0.85}Nd_{0.15})(Ti_{0.1}Fe_{0.9})O_3$", *APL Mat.* **1** 021102 (2013)

27. L. Q. Wang, B. Schaffer, I. MacLaren, S. Miao, A. J. Craven, I. M. Reaney, "Atomic scale structure and chemistry of anti-phase boundaries in $(Bi_{0.85}Nd_{0.15})(Fe_{0.9}Ti_{0.1})O_3$ ceramics", *J. Phys.: Conf. Ser.* **371** 012036 (2012)

28. L. Brohan, A. Verbaere, M. Tournoux, G. Demazeau, "La transformation TiO_2(B) → anatase", *Mater. Res. Bull.* **17** 355-361 (1982)

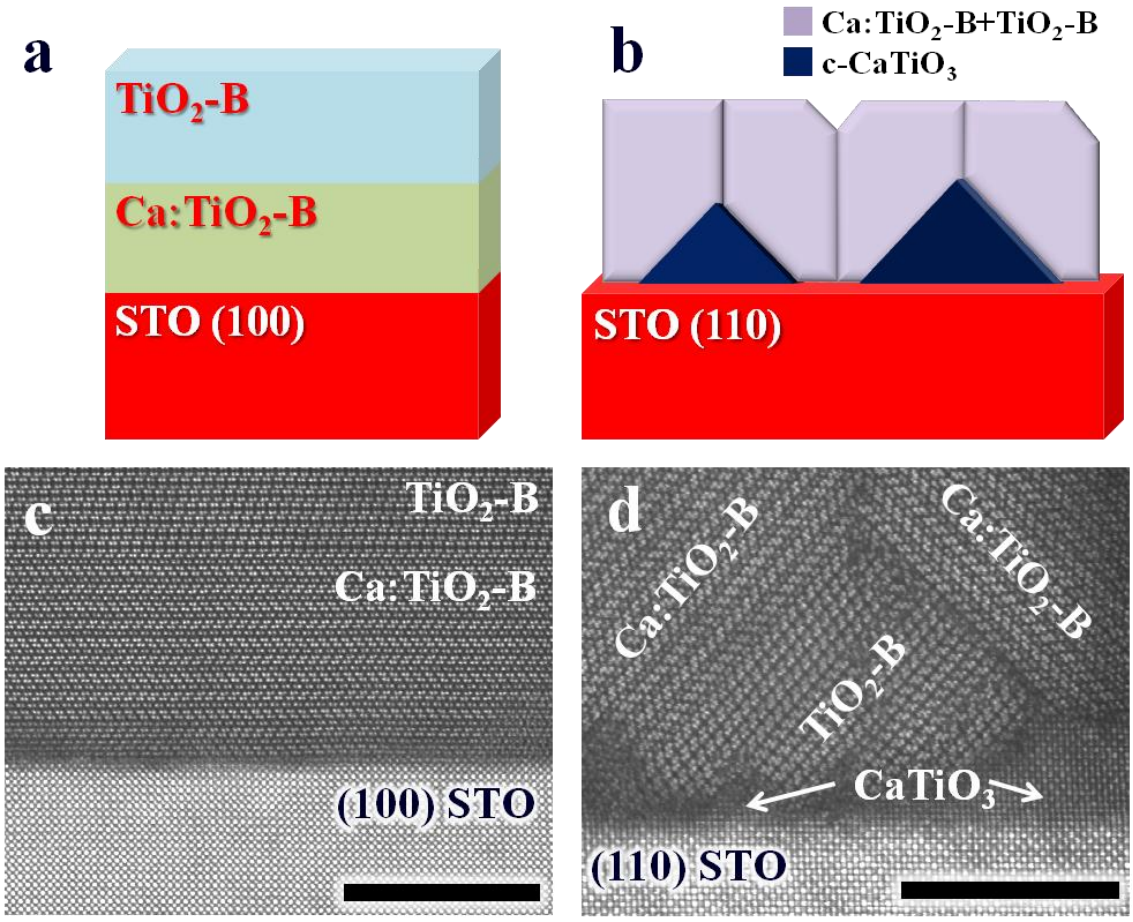

Figure 4.1 Schematics and corresponding high-resolution STEM images of films grown on **a.** and **c.** (100) and **b and d.** (110) STO substrates. Scale bars are 10 nm.

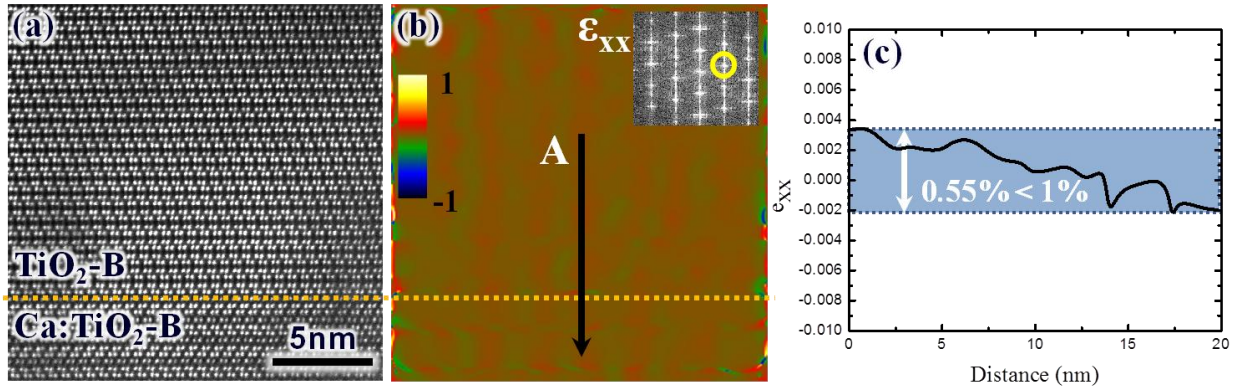

Figure 4.2 Misfit strain analysis of TiO_2-B and Ca:TiO_2-B using geometric phase analysis. **a.** An actual HR-STEM image, **b.** a strain (ε_{xx}) map of an image, and **c.** a strain profile from the line-scan A.

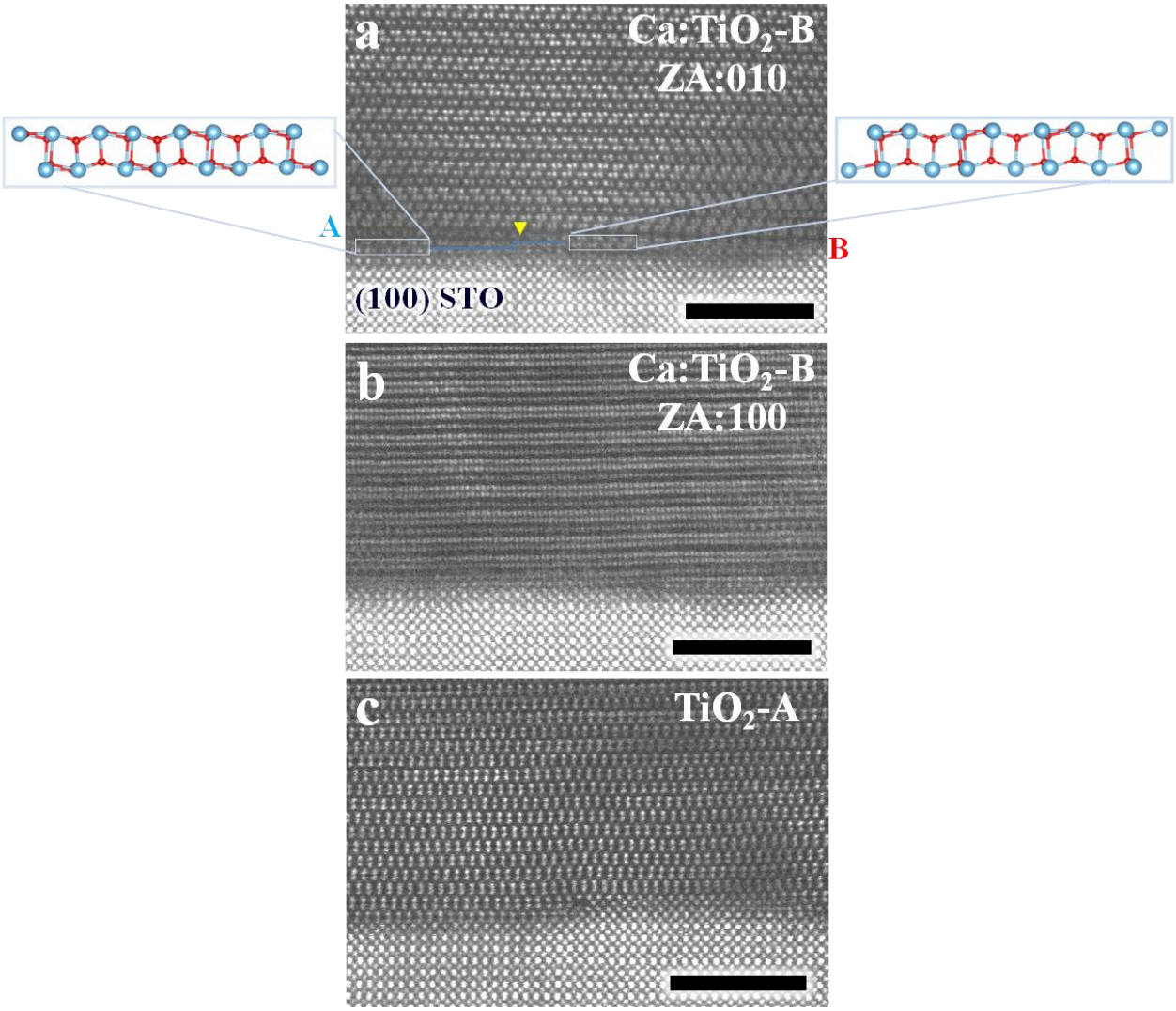

Figure 4.3 High-resolution STEM images of interfaces between STO and **a. and b.** Ca:TiO_2-B and **c.** TiO_2-A resulting from growth of a Ca:TiO_2-B film on (100) STO. A and B denote left and right c-orientation of a TiO_x stack. Scale bars are 5 nm.

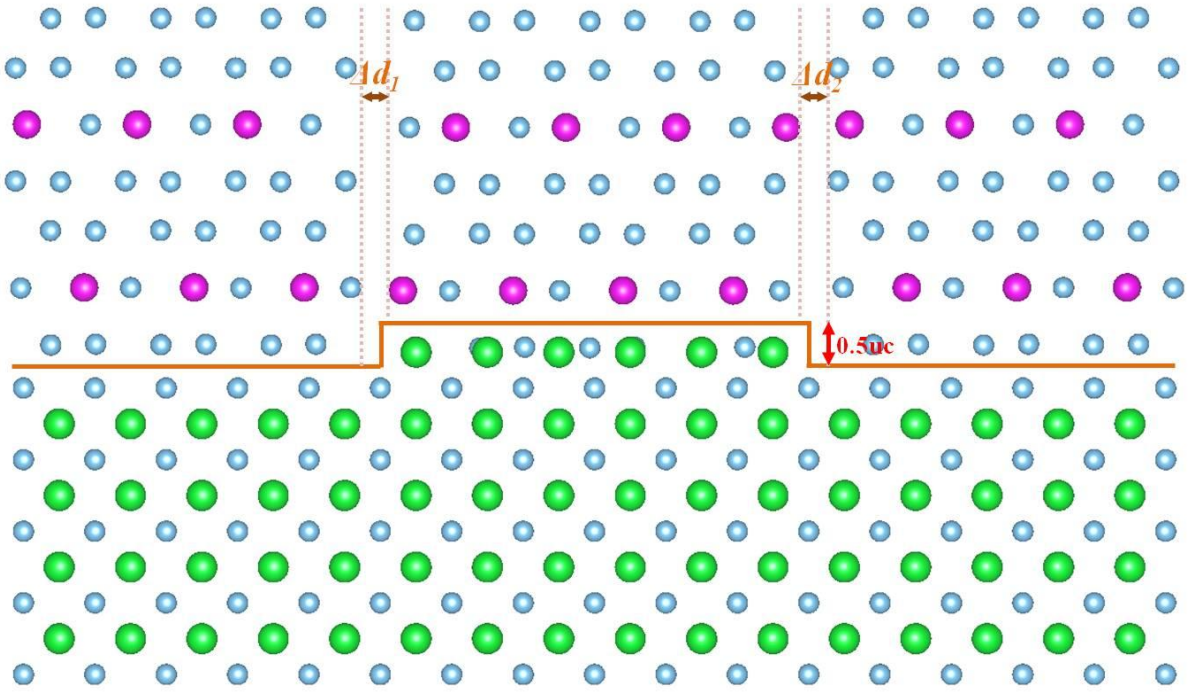

Figure 4.4 A schematic illustration of a surface step terrace (= 0.5 unit cell (u.c.)), or SST, at the interface between STO and Ca:TiO_2-B. Unit cells of Ca:TiO_2-B cannot fulfill epitaxy everywhere along the surface where there are gaps (equivalent of Δd_1 and Δd_2 in the diagram) due to the step. However, during growth, each gap is filled with another vertical row of atoms.

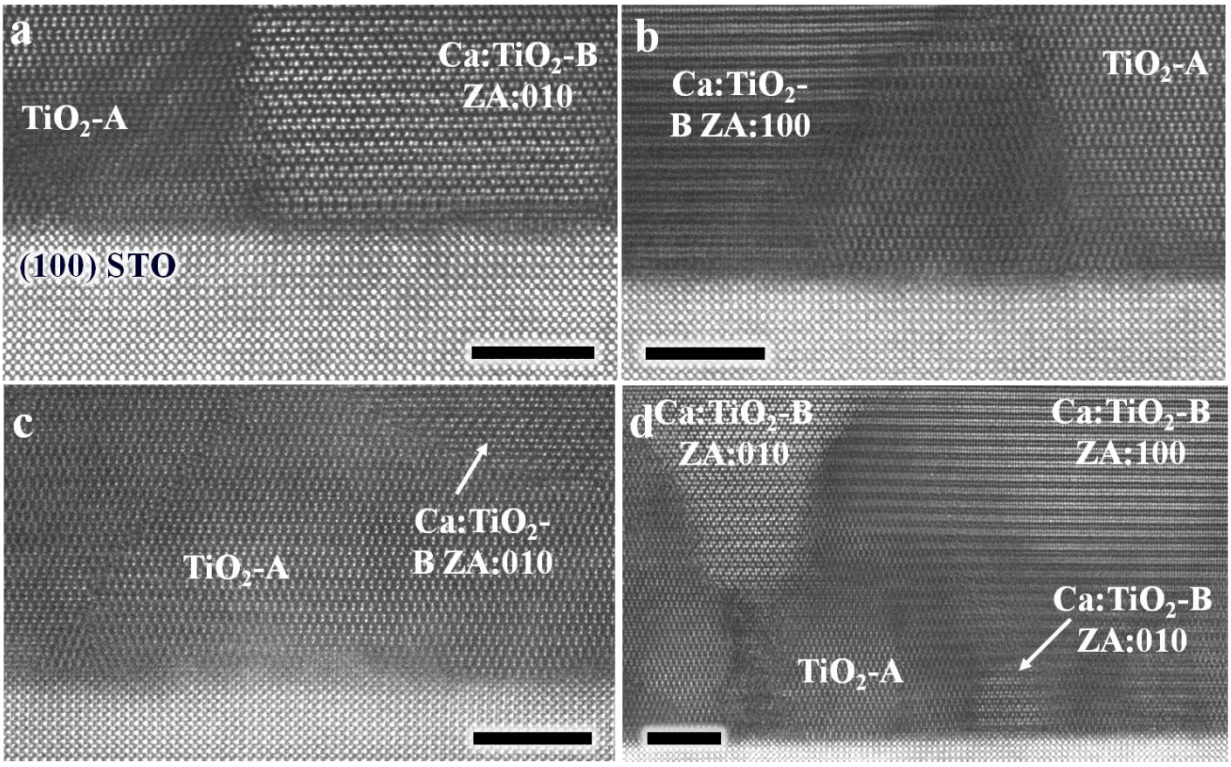

Figure 4.5 High-resolution STEM images of interphase boundaries between TiO_2-A and Ca:TiO_2-B along **a.** [010] zone axis (ZA:010) and **b.** [100] axis (ZA:100). **c. and d.** High-resolution STEM images of interphase boundaries formed via Ca:TiO_2-B intergrowth from TiO_2-A. Scale bars are 5 nm.

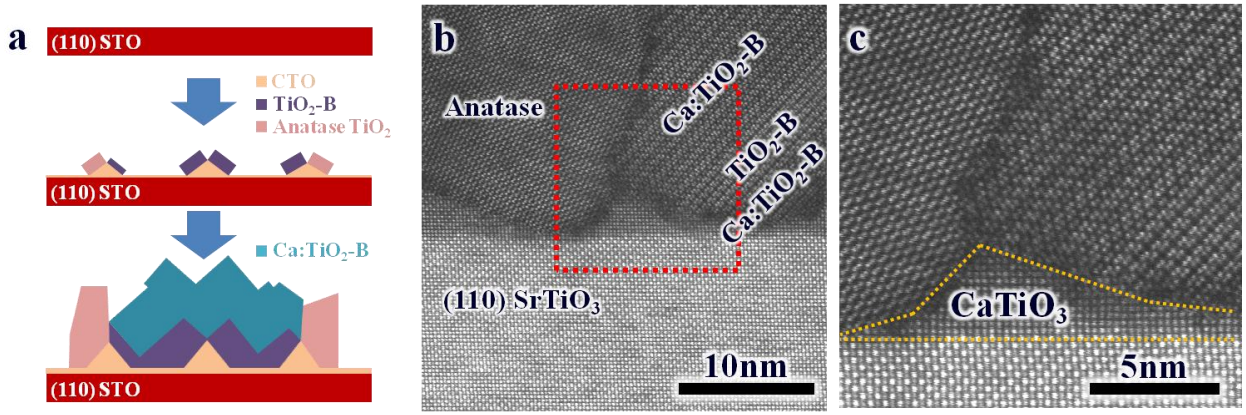

Figure 4.6 a. Schematic of sequential growth of TiO_2-B + Ca:TiO_2-B mixture phase and another titania polymorph, anatase, grown on (110) STO, **b.** high-resolution STEM images showing the presence of $CaTiO_3$ layer for tilted growth of the mixture phase. **c.** an interphase boundary formed between anatase and TiO_2-B grains.

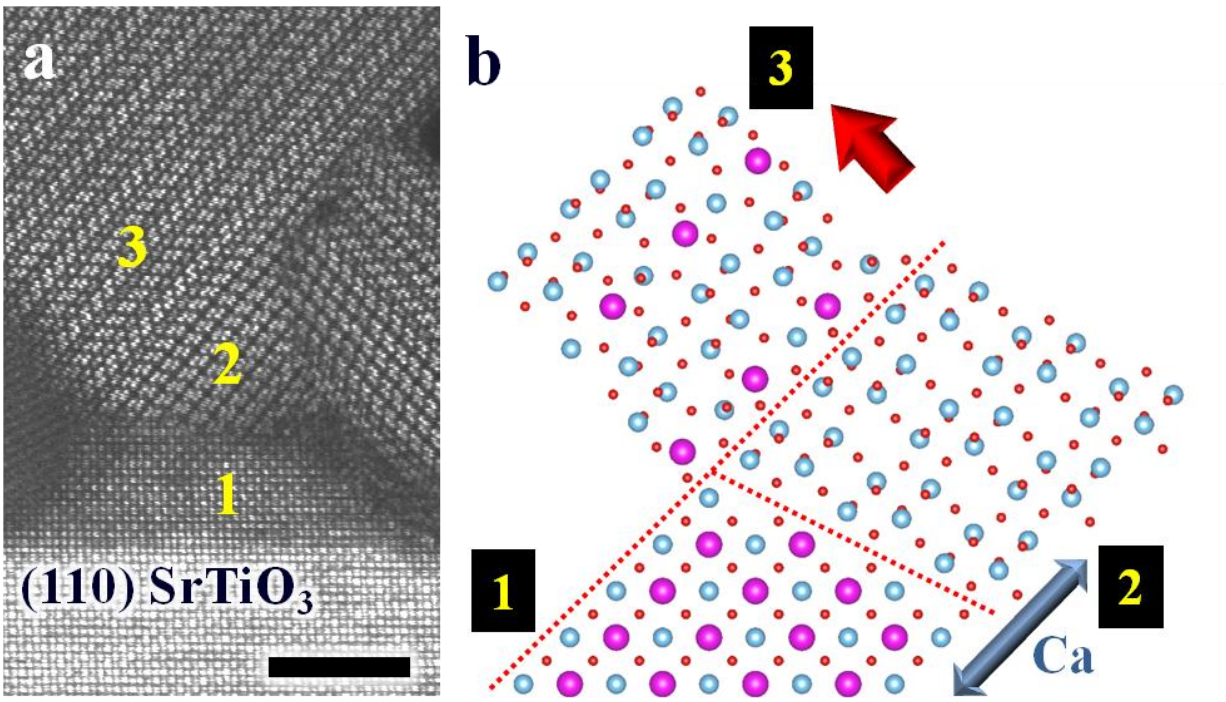

Figure 4.7 The growth of Ca:TiO_2-B on (110) STO begins with Ca ion migration and formation of discrete layers of (1) $CaTiO_3$ and (2) TiO_2-B which then acts as a template layer for deposition of (3) Ca:TiO_2-b as shown in **a.** high-resolution STEM images and **b.** atomic model schematic: (1) $CaTiO_3$ and (2)TiO_2-B are formed by phase separation via Ca flow. Scale bar is 5 nm.

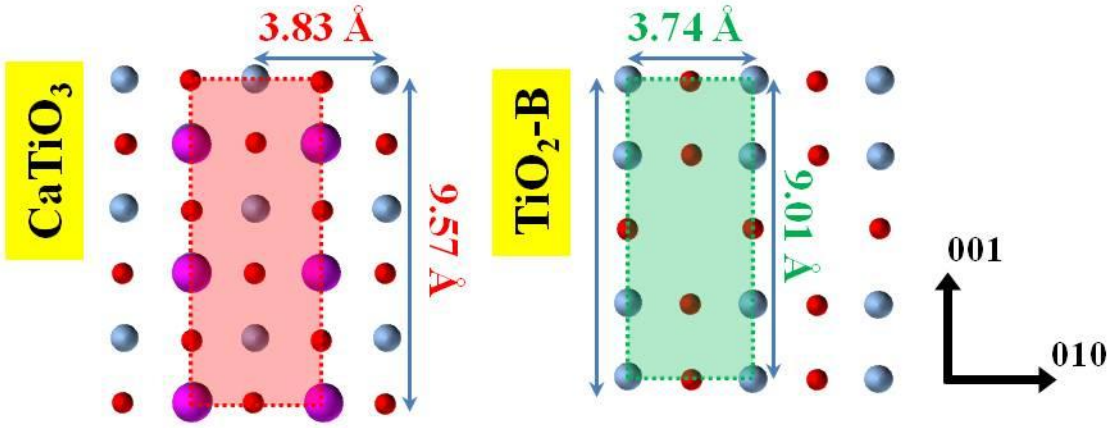

Figure 4.8 Comparison of atomic configuration between (100) planes of $CaTiO_3$ and TiO_2-B.

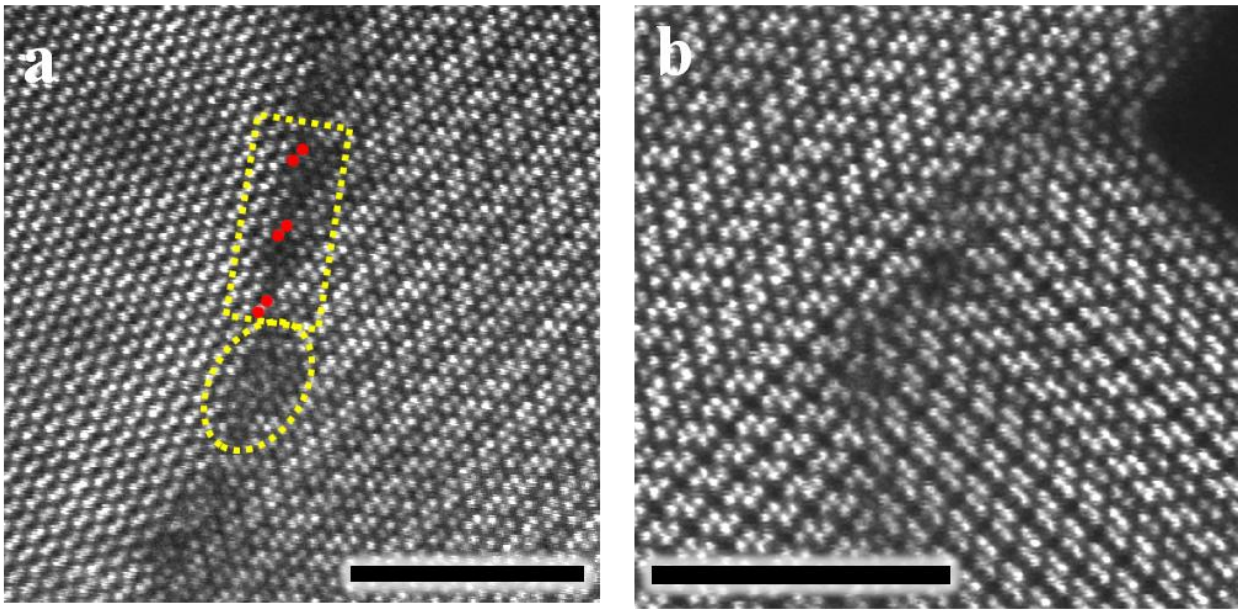

Figure 4.9 High-resolution STEM images showing **a.** an interphase boundary between the Ca:TiO_2-B and TiO_2-A grains and **b.** a grain boundary between the two abutting Ca:TiO_2-B grains tilted 45^o towards each other. A rectangle and a circle in **a.** show locally ordered and disordered regions within the boundary. Scale bars are 5 nm.

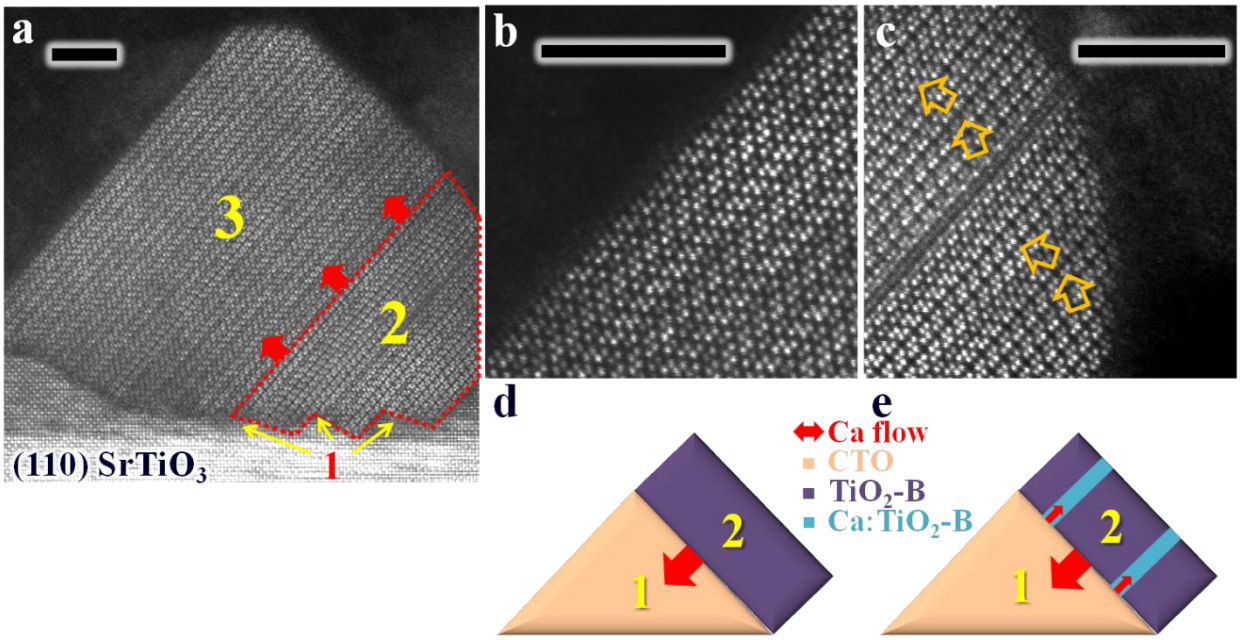

Figure 4.10 a. An example of an intermixed 2: TiO_2-B variant template layer due to intercalated calcium layers and its schematics **e.** It is different from the perfect template layer as illustrated in Figure 5 and also as a schematics in **d. b. and c.** High-resolution STEM images of regions 3 and 2, respectively. Scale bars are 5 nm

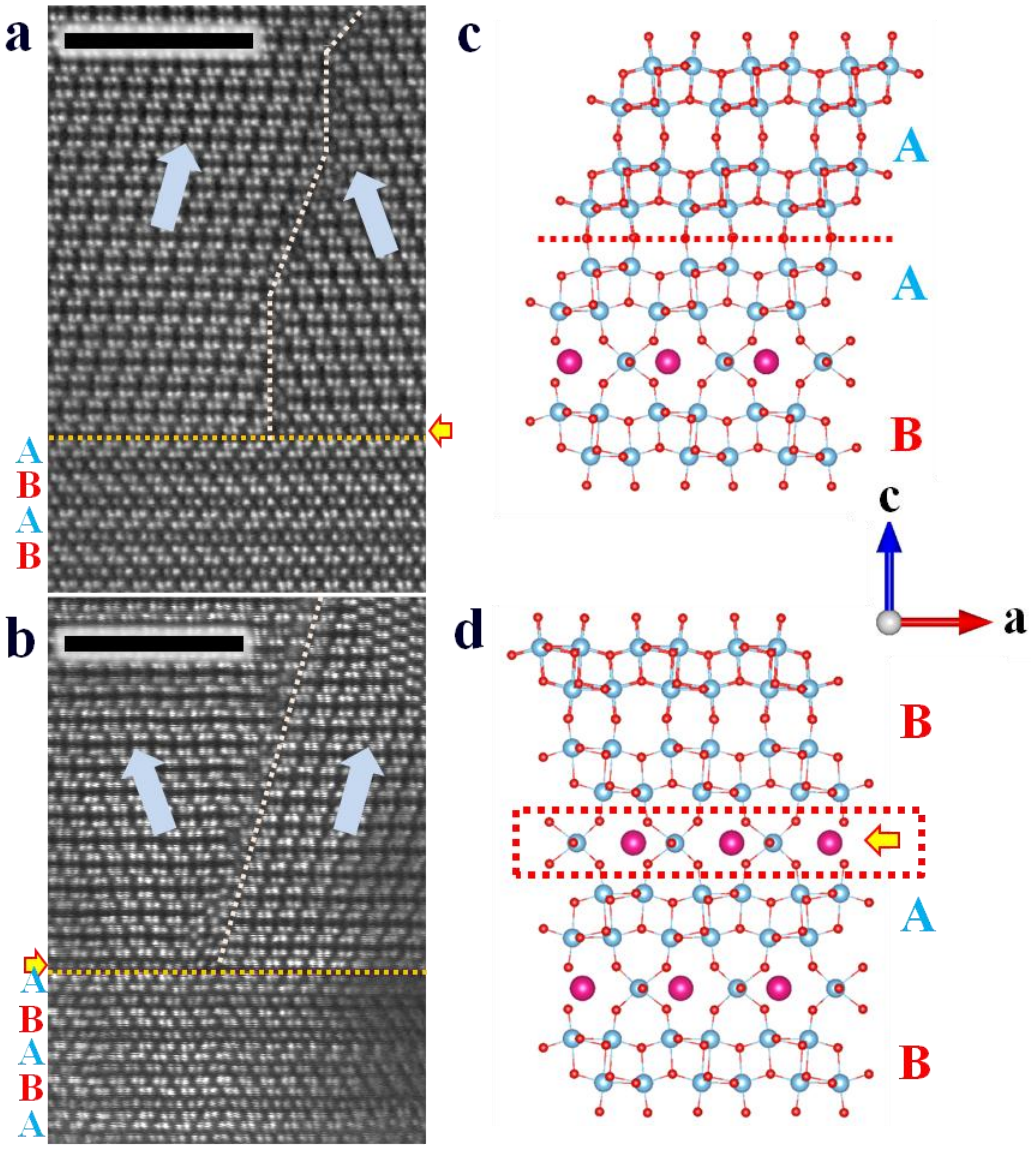

Figure 4.11 a. and b. High-resolution STEM images of defects at the interface between TiO_2-B and Ca:TiO_2-B that generate the two adjacent TiO_2-B grains oriented opposite direction and **c. and d.** schematics of TiO_2-B and Ca:TiO_2-B interface without and with presence of Ca-modified layer indicated with the yellow arrow. Scale bars are 5 nm.

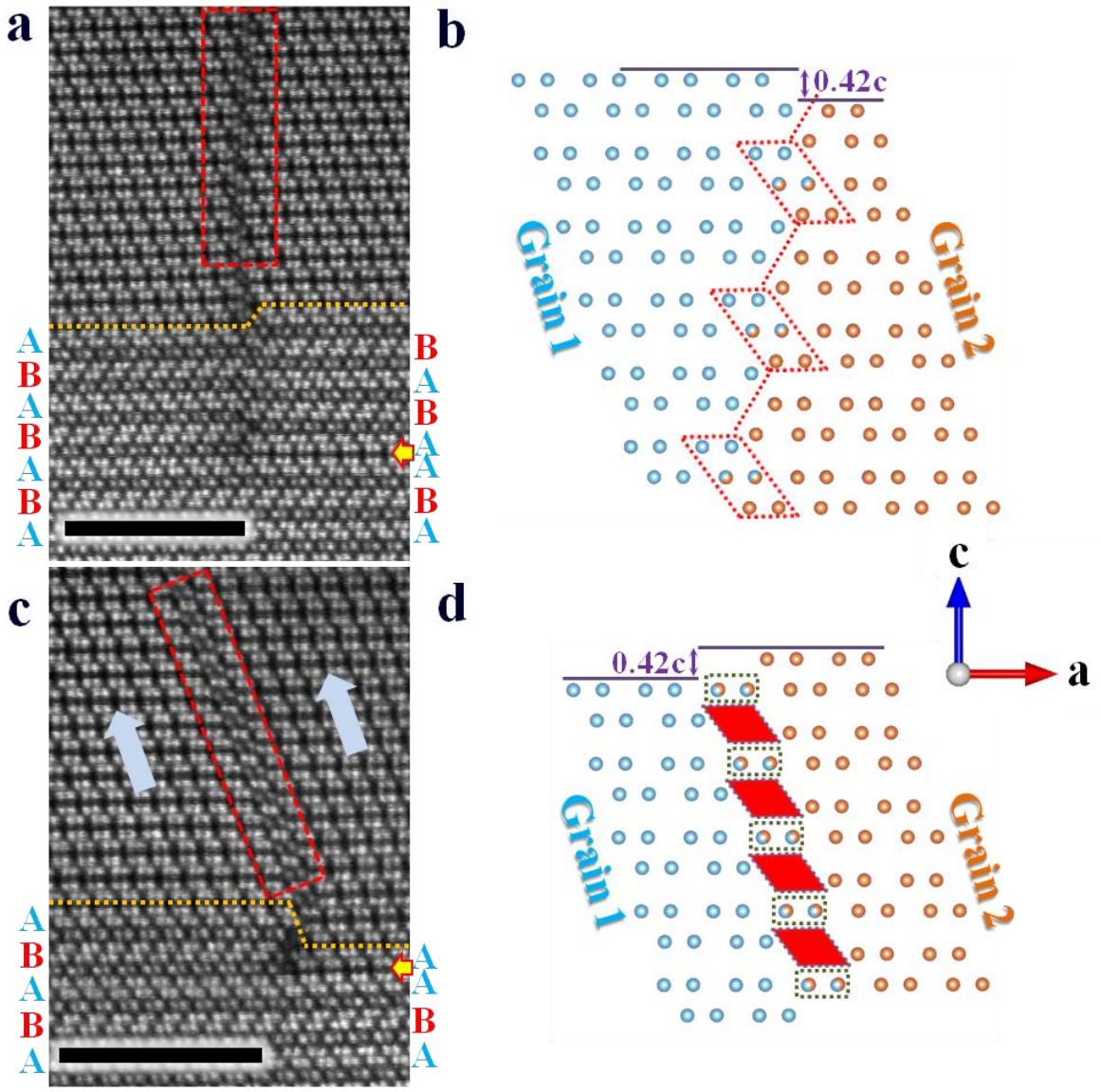

Figure 4.12 a. and c. High-resolution STEM images of defects at the interface between TiO_2-B and Ca:TiO_2-B with missing Ca-modified layer that generate the two adjacent TiO_2-B grains oriented same direction. **b. and d.** Schematics of periodic boundary formed between the two adjacent grains from the regions marked with red in **a** and **c**. Sites with atoms marked with both gold and blue represent possible occupancy sites for Ti atoms from either Grain 1 or Grain 2. Scale bars are 5 nm.

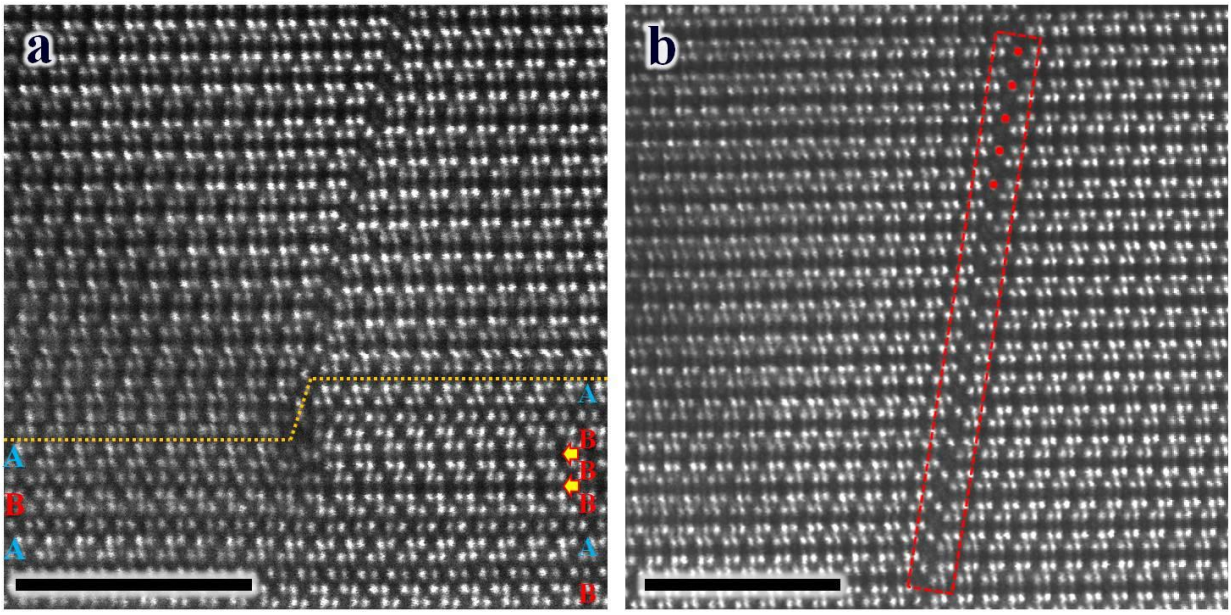

Figure 4.13 a. High-resolution STEM images of defects at the interface between TiO_2-B and Ca:TiO_2-B with two missing Ca-modified layers that generate the two adjacent TiO_2-B grains oriented same direction. **b.** This generates the long-range boundary condition throughout the boundary with possible occupancy sites for Ti atoms from either left or right-side TiO_2-B grain. Scale bars are 5 nm.

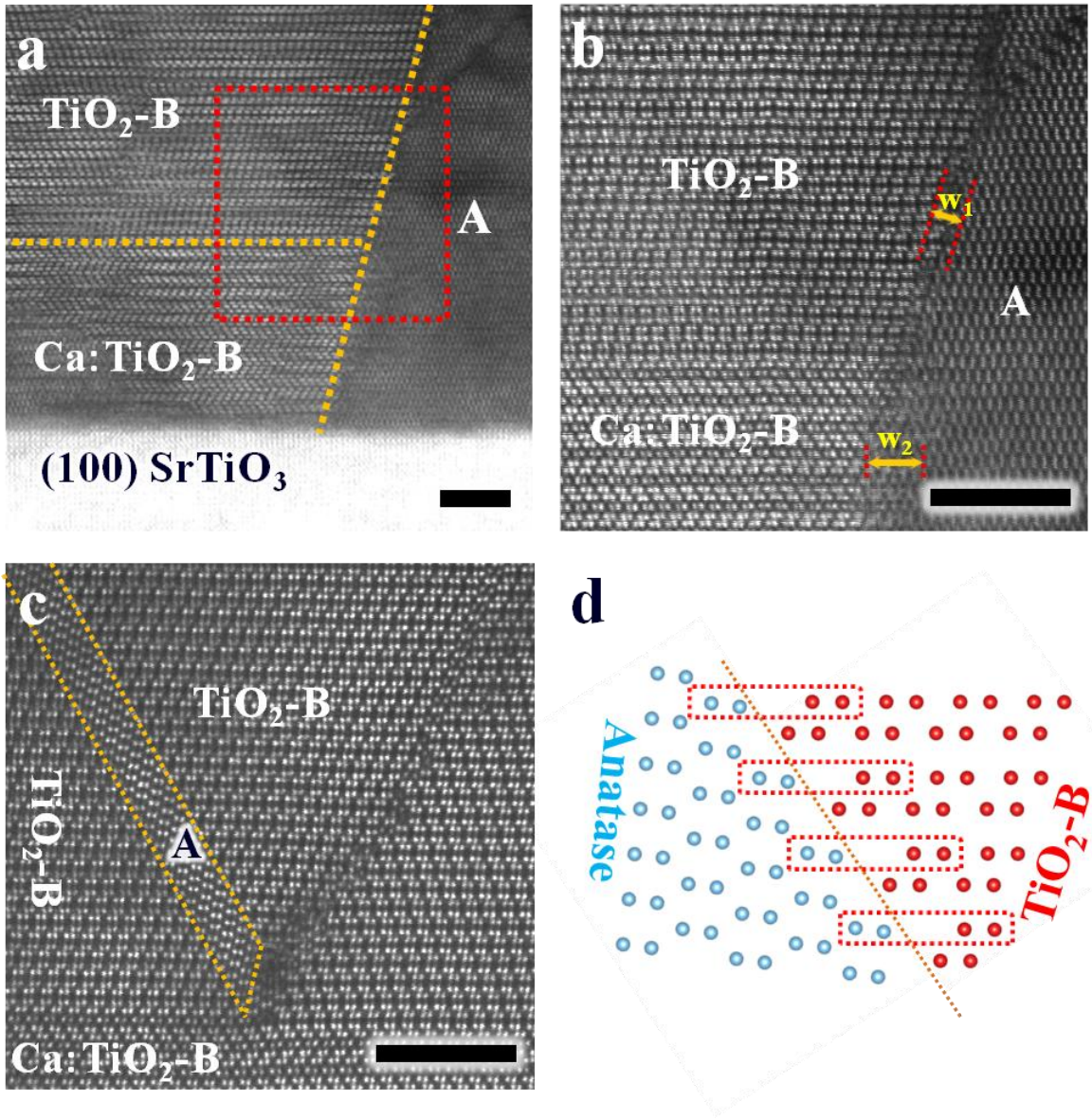

Figure 4.14 High-resolution STEM Images of **a. and b.** an interphase boundary between an anatase grain grown directly on (100) STO substrate independent from TiO_2-B and Ca:TiO_2-B and **c.** an anatase micro-grain epitaxially formed between the two TiO_2-B grains along with a **d.** schematics of bonding between periodic boundary formed between anatase and TiO2-B grains. Scale bars are 5nm.

Chapter 5. Study of strain relaxation mechanism of Ca:TiO_2-B-templated TiO_2-B thin film upon Li intercalation

5.1. Introduction and Background

As also mentioned in Chapter 4, the bronze polymorph of TiO_2 (TiO_2-B) is known to be a low-density lithium intercalation host that has open channels, favorable for Li ion migration, which maximizes both specific capacity and charge-discharge capability.[1-4] Indeed, the intercalation capacity of Li ions in TiO_2-B is reported to range from 0.8 Li^+ per TiO_2 unit (bulk) to as high as 0.91 Li^+ per TiO_2 unit (nanowires (NWs)).[5-8]

However, despite the recent success of nano-scale engineering of TiO_2-B, both in terms of mechanical stability and enhanced Li^+ intake[5,9-11], there is little known about the effect of Li insertion on structural stability of TiO_2-B. Most mechanistic studies employ theoretical calculations using density functional theory (DFT), and only a few of them have been supported with experimental findings.[6,12] Further, the theoretical results on the effect of Li ion intercalation are so different from one another that there has not even been agreement on Li site occupancy within the TiO_2-B lattice.[13-16] Recent work by Morgan et al. has demonstrated that this wide disagreement is because the DFT results are sensitive to the choice of assumed parameters.[15] These theoretical calculations thus have limited value for further study of the electronic and chemical profile of the TiO_2-B structure (i.e., bonding profile and electron density) surrounding

the inserted Li ions.[17-19] Here, by contrast, we conducted electrochemical lithiation of a highly crystalline TiO_2-B thin film via in-situ high-resolution transmission electron microscopy (HRTEM) for direct visualization of Li ion insertion and migration into TiO_2-B. In the course of this study, we observed the structural relaxation of a lithiated TiO_2-B film upon its Li-induced volumetric expansion and identified its unique mechanism with the help of theoretical calculation.

5.2. Experimental Procedures

5.2.1 Experimental

TiO_2-B thin films were synthesized by pulsed laser deposition (PLD) of a pure TiO_2 target onto a calcium-doped TiO_2-B (Ca:TiO_2-B) film deposited on (100) Nb-doped $SrTiO_3$ (Nb:STO). The details about this growth were already presented in Chapter 4.

Cross-sectional TEM specimens of after-cycled TiO_2-B films were prepared via mechanical polishing followed by Ar ion milling. All the specimens were characterized using aberration-corrected STEM (JEOL JEM 2100F and JEOL JEM 3100F).

A mechanically polished TEM specimen was loaded onto a single-tilt in-situ TEM-STM holder (Nanofactory) as one electrode of an electro-chemical cell assembly. The rest of the procedure for the electro-chemical set-up is similar to that presented in Chapter 3.

5.2.2 Theoretical calculation

First-principles electronic structure calculations and Monte Carlo simulations with cluster expansion formalism based on statistical mechanics were performed to predict phase stability of polymorph Li_xTiO_2 phase at finite temperature.[c]

5.3. Results and Discussion

For the purpose of this study, we fabricated a highly crystalline thin film of TiO_2-B on a (100) Nb:STO substrate, which again hinged on the use of $CaTi_5O_{11}$, as an interposed template layer, similar to that presented in the previous chapter. The lattice mismatch between regular TiO_2-B and Ca:TiO_2-B is again very small, less than 1% as calculated by geometric phase analysis (GPA).[21] The thin film was grown along [001] direction with mixed arrangements of large TiO_2-B grains with (100) and (010) planes exposed to the film's cross-section as illustrated in the high-resolution scanning transmission electron microscopy (HRSTEM) image that shows the boundary between those two representative grains (Figure 5.1b). Figure 5.1a and 5.1c are the atomic model schematics of a TiO_2-B lattice along [100] and [010] orientations and corresponding simulated selected area electron diffraction (SAED) patterns[22].

The thin film geometry was preferred over a NW for this study since the surface of a thin film grown along [001] direction, being much wider than the end of a NW, offers more choice for Li ions to diffuse through many different pathways, thus increasing the chance to identify evidence for Li ion insertion via in-situ TEM. Furthermore, as already demonstrated in Chapter 4, the film

[c]For the details of this theoretical work, the thesis written by Donghee Chang[20] from Anton Van der Ven's group in University of California-Santa Barbara needs to be referred.

contains large defect-free regions where the Li ion source can make local contact and hence minimize any structural influence of defects in the film on lithiation. A schematic of our in-situ TEM set-up for lithiation of a TiO_2-B film is shown in Figure 5.2a. By contacting the top surface of the film with the Li-metal coated STM tip, an electro-chemical cell was assembled and run with an external voltage source-meter. Figure 5.2b shows an image of the tip and the film after breaking up the contact, following an electrochemical lithiation experiment, as described below. The naturally grown Li_2O on the STM tip acts as a solid electrolyte for the cell since it is electrically insulating but has high Li ion conductivity. Figure 5.2c shows the electron energy loss spectroscopy (EELS) spectra of the Li-K edge and the O-K edge in Li_2O. The peaks shown in both near-edge spectra match well with the literature on the electronic environment in Li_2O structure.[23] Lithiation of a TiO_2-B structure was conducted under potentiostatic mode at room temperature. Assuming that a sudden conductance change, observed at -3 V (film relative to STM tip) as the voltage was swept from 0 to -5 V, is an indication of the threshold for Li ion transport through the electrolyte into TiO_2, we used the higher lithiation voltage of -4 V in order to expedite Li ion migration into the film. In this study, no analysis of delithiation of the film was attempted due to the difficulty of extracting much of the widely spread Li from the film after lithiation.

Upon lithiation of the thin film under constant bias of -4 V, rapid surface wetting by Li metal occurred instantly across a wide region of the film surface, probably also covering most of the cross-section of the film (i.e., the sides of the TEM grid), followed by slower growth in extent of the layer as lithiation proceeded. Li metal in direct contact with the TiO_2-B film formed a thin layer of sub-crystalline material, 2-3 nm in thickness, with a distinct cubic lattice. Using fast Fourier transformation (FFT), this layer was found to be c-Li_xO (*space group:* Fm3m). The

formation of c-Li_xO has been previously observed as a reaction product of Li and a nano-structured TiO_2 electrode during in-situ lithiation.[24-25] This layer could only be identified at the top most surface of the thin film because of its few nm thickness, which makes it very electron beam (e-beam) transparent and thus hardly visible on the remainder of the film's cross-section. We speculate that the Li_xO formation is driven by the chemical interaction between Li metal and the TiO_2-B film, which creates a solid-electrolyte interphase (SEI) layer that effectively slows the rate of further Li migration into the bulk of the film. Interestingly, extended exposure of the cross-section to the e-beam promotes further reaction between the Li metal that wet the surface of the cross-section and TiO_2-B, inducing the complete phase transformation into spinel Li_xTiO_2 (Figure 5.3). Hence, all HRTEM images shown below were taken with a faster survey rate at lower beam dose to minimize the influence of the e-beam on the film.

5.3.1 Strain-induced phase transformation upon b-axis lithiation in TiO_2-B

In conjunction with the initial formation of these surface features described above, a more well-defined structural change occurred in TiO_2-B under lithiation at -4 V. The change involved a nano-scale shear of the TiO_2-B layer from the top surface all the way to the interface between TiO_2-B and Ca:TiO_2-B. The shear occurred in two different modes; 1) via abrupt burst vertically across the TiO_2-B lattice and 2) via gradual rupture across the TiO_2-B lattice.

A first mode occurred within the film as soon as Li ions propagated laterally from a Li source throughout the wide periphery of the film's cross-section. As it propagated, Li ions diffused into primitive TiO_2-B grains and induced the sudden rupture of the shear entirely across the TiO_2-B lattice. Li ion migration was observed through the change in image contrast; as this contrast

swept across the film, the shears were abruptly ruptured. Hence, in the end, a large number of shears throughout the primitive TiO_2-B lattice were generated over a wide region away from the tip-film contact. Schematics in Figure 5.4a and HRTEM images of the TiO_2-B thin film before and after Li ion insertion (Figure 5.4b and c) demonstrate occurrence of this shear. The three identical features, each marked with an arrow, clearly indicate that changes occurred during lithiation. Interestingly, as demonstrated in the FFT pattern taken from a HRTEM image (Inset of Figure 5.4b), these shears only occurred when a (010) plane was exposed at the film's cross-section. According to many theoretical studies[12,26], Li ion intercalation most favorable occurs along a *b*-axis since it is the largest open channel in a TiO_2-B lattice. This can imply that as Li ions propagated along the film's cross-section, it was most likely that they diffused through a (010) plane to induce shears.

As opposed to the first mode, the second mode shears were generated when Li intercalated into a TiO_2-B film that had already been lithiated to a certain extent. Interesting, this type of shears happened only at the tip-film contact. Along with the schematics in Figure 5.5a, HRTEM images in Figure 5.5b and c show a TiO_2-B film with additional shears. Interestingly, the formation of a shear occurred much gradually than that under the first mode. The possible reason for this slow kinetics is because the formation of a solid-electrolyte interphase upon Li wetting on a film's cross-section made Li insertion into a bulk much difficult. This also explains why this type of a shear can proceed partially across the film and only happen at the tip-film contact where there is a large reservoir of Li from the source that can be electrochemically impinged upon the surface of the film.

In both modes of shearing, the thickness of the Li metal wetting layer increased perceptibly when these Li ion induced defects were generated. This conveys our belief that Li ions transferred

from the STM tip to the TiO_2-B structure either stayed on the cross-sectional surface of the thin film or migrated into TiO_2-B structure, creating a unique set of defects. The defect generated in the TiO_2-B layer did not extend into the Ca:TiO_2-B layer, suggesting that Ca:TiO_2-B is thermodynamically more stable than regular TiO_2-B or possibly amount of Li inserted into the lattice was too low to induce any discernible structural change. The HRSTEM images in Figures 5.6a and b provide a detailed illustration of one of the representative Li insertion-induced defects formed via shearing upon Li ion insertion. The tiny microstructure formed in between the two abutting TiO_2-B lattices strikingly resembles that in the as-grown (100) TiO_2-B film discussed in Chapter 4 with the anatase-type structure formed by the 6 Ti atoms each from TiO_2-B on the left and right (Figure 5.6c). The angle of this shear normal to the substrate was found to be 34 ^{o} for all the defects of this type, everywhere throughout the film. This raises the possibility that the lattice expansion upon Li insertion into a TiO_2-B film generated the micro-structural misfit strain and induced the phase transformation to an anatase-type structure for effective strain relaxation. To explore this possibility, the theoretical calculation using density functional theory (DFT) was employed.

5.3.2 Phase stability and structural relationship of various lithiated TiO_2 polymorphs

To first understand the possibility of phase transformation from bronze to anatase-type structure upon lithiation, a phase stability calculation on series of lithiated titania polymorphs was conducted upon varying Li content. The TiO_2 polymorphs considered in the calculation were bronze, anatase, and spinel structure. Pure anatase TiO_2 and fully lithiated anatase TiO_2 were

considered as reference for the calculation of the formation energies, per TiO_2 formula unit, of lithiated TiO_2 polymorphs (Li_xTiO_2), which is also defined as:

$$\Delta E(x) = E(x) - xE_{TiO_2} - (1-x)E_{LiTiO_2} \quad [1]$$

where E(x) is the free energy required for specific Li vacancy arrangement at Li concentration *x* in Li_xTiO_2 for anatase, bronze, and spinel TiO_2 phases. E_{TiO2} and E_{LiTiO2} are the energies of the primitive anatase TiO_2 and fully lithiated anatase $LiTiO_2$. Based on this calculation, it was found that upon Li insertion over Li mole fraction x=0.4, anatase and spinel TiO_2 become energetically favorable to form than TiO_2-B. At x=0.5, the phase stability of Li_xTiO_2 becomes in the descending order of spinel > anatase > bronze, showing that the ordered spinel phase becomes the most stable structure. This agrees well with previous experimental studies on the formation of spinel $LiTi_2O_4$.[27] Upon Li insertion x>0.6, the anatase polymorph becomes the most stable.

Phase stability calculation indicates that there is a thermodynamic driving force for the transformation from Li_xTiO_2-B to both anatase-type Li_xTiO_2 and spinel Li_xTiO_2 upon insertion of high concentration Li in the range of $0.4<x<1$. However, this does not imply that both phases are easy to be transformed from Li_xTiO_2-B because the new phase nucleation is also heavily dependent upon strain energy penalties due to the structural misfit between the new phase and Li_xTiO_2-B. Hence, the next step was to consider the possibility of Li_xTiO_2-B having coherent interfaces with the new phase - anatase and spinel Li_xTiO_2.

To explore this possibility, the crystallographic relationship between the new phase and the Li_x TiO_2-B was first considered. Intuitively, the degree of shear-induced deformation upon lithiation for Li_xTiO_2-B → spinel Li_xTiO_2 transformation is ought to be greater than that of Li_xTiO_2-B → anatase Li_xTiO_2 because the transformation from a monoclinic (Li_xTiO_2-B) to a cubic structure

(spinel Li_xTiO_2) requires a larger degree of crystallographic deformation than that of a tetragonal (anatase TiO_2) or an orthorhombic structure (β-$LiTi_2O_4$).

Indeed, the crystallographic pathways that link Li_xTiO_2-B and spinel Li_xTiO_2 could not be identified due to lack of similarity in Ti and O bonding configurations in the two materials. However, a crystallographic pathway linking $LiTi_2O_4$-B (x=0.5) and β-$LiTi_2O_4$ can be easily identified as shown in Figure 5.7. By shearing the corner of a $LiTi_2O_4$-B unit cell diagonally, a monoclinic structure can be transformed to an orthorhombic structure. As a result, a sheared monoclinic structure with some degree of lattice distortion shares a similar Ti and O bonding configuration with β-$LiTi_2O_4$.

In view of the crystallographic similarities between Li_xTiO_2-B and anatase Li_xTiO_2, it is possible that two phases can coherently coexist. This possibility can be evaluated using the Green-Lagrange strain tensor *E*, which is a measure of atomic displacement that the new phase undergoes to fit crystallographically to the parent phase. *E* is defined as:

$$E = \frac{\hat{F}^{+}F - I}{2} \qquad [2]$$

where *F* is the deformation tensor based on the ratio between the lattice constants of the transformed crystal *L'* to the lattice constants of the original crystal *L*, according to *L'=FL*. F^+ corresponds to the transpose of *F*. If the set of three eigenvalues obtained from the deformation tensor *F* has one positive, one negative, and one close-to-zero eigenvalues, there exists a strain invariant plane, also known as a 'habit plane'. Both the transformations from TiO_2-B to anatase TiO_2 and from $LiTi_2O_4$-B to β-$LiTi_2O_4$ satisfy this requirements. However, the eigenvalues close to zero are still considerable and, thus, this transformation should be accompanied by coherency

strain. The estimated strain energy generated via transformation from $LiTi_2O_4$-B to β-$LiTi_2O_4$, according to first principles calculation, is 81 meV per Ti, which is smaller than the free energy difference of $LiTi_2O_4$-B and β-$LiTi_2O_4$. This indicates that it is energetically favorable for $LiTi_2O_4$-B to transform into β-$LiTi_2O_4$.

A schematic in Figure 5.8 demonstrates the two examples of transformation possible in TiO_2-B and lithiated TiO_2-B at the calculated habit plane. Interestingly, the atomic configuration at the interface between $LiTi_2O_4$-B and β-$LiTi_2O_4$ matches very well with the one observed experimentally via in-situ TEM upon Li insertion into TiO_2-B. This strongly implies that the shears generated in a film are most likely induced by the misfit strain from the volumetric change of a TiO_2-B lattice upon *b*-axis lithiation. To relax this strain, the Li_xTiO_2-B film at x=0.5 undergoes the low order phase transformation to a β-$LiTi_2O_4$ phase along the habit plane under minimum stress.

5.3.3 Structural relaxation of TiO_2-B upon c-axis lithium intercalation

The strain-induced structural transformation upon Li insertion discussed so far has been observed only for the TiO_2-B grains with a (010) plane exposed at the film's cross-section. However, for the case of the grains with a (100) plane exposed to the surface, Li ions would experience difficulty in penetrating through the film's cross-section because the least open channel of TiO_2-B is along *a*-direction. In fact, the DFT calculations done by both Islam[12] and Panduwinata[26] demonstrated *a* channels to have the migration energy barrier at least 3 times higher than *b* channels. Hence, we need to consider another possibility - that is *c*-axis Li migration, since its migration energy is as comparably low as that of *b*-axis. As Li ions penetrate through a (001)

plane and migrate along *c*-axis, it is likely that they also diffuse through *b*-axis and induce lattice expansion. Hence due to the local lattice misfit strain upon Li insertion, the film undergoes shearing to relieve the local misfit strain, similar to the case of *b*-axis lithiation. The cross-sectional HRSTEM images of TiO_2-B in Figures 5.9a and b demonstrate well how the shearing occurred. All the sheared pathway under the [100] view axis look slightly curved, but it is worth noting that the extent of a shear that initiated from the topmost surface of a TiO_2-B film is different from region to region as illustrated in Figure 5.9a. This suggests that the local strain relaxation occurred at various places may happen at different points in time upon lithiation since Li migration can either proceed along *c*-axis or side-track to *b*-axis. Surprisingly, similar defect features were also observed during the post-mortem study of the film cycled electrochemically via a method explained elsewhere[28], as shown in Figures 5.9c and d. A noticeable feature observed in some grains upon shearing induced by *c*-axis Li intercalation is the formation of a cubic mound at the topmost (001) plane. Figure 5.10 shows a HRTEM image of this mound and the corresponding fast Fourier transformation FFT image (from the region marked as B). By making the direct comparison of FFT patterns between the mound and the adjacent TiO_2-B matrix (Figure 5.10b) generated from the HRTEM image (Figure 5.10a), it was found that the mound has a spinel Li_xTiO_2 structure, which is known to be the most thermodynamically stable phase at x=0.5.

Finally, to fully support that Li indeed intercalated into TiO_2-B, a fine electronic study such as core-loss EELS was performed on a lithiated region of the specimen to detect any shift of valence of Ti. For EELS performed on a TiO_2-B film prior to lithiation (a STEM image shown in Figure 5.11a), the L_2 and L_3 edges of Ti are consist of the two distinct peaks that correspond to e_g and t_{2g} levels. These levels are separated by the octahedral crystal field (orbital degeneracy) and

clear characteristics of 4+ valence of Ti. (EELS in Figure 5.11c(i)) However, the core-loss edges shown in the after-lithiated TiO_2 film (EELS in Figure 5.11c(ii) taken from a STEM image in Figure 5.11b) only have a single peak per edge that was most likely aroused from the valley in between e_g and t_{2g} peaks upon valence transition of Ti from 4+ to 3+. This transition strongly suggests the phase transition from TiO_2-B to $LiTiO_2$-B upon full lithiation. In addition to a TiO_2-B layer, the core-loss edges on Ca:TiO_2-B and STO layers were also examined. EELS spectra in Figure 5.12 demonstrates the point EELS study performed on all three distinct layers. As opposed to Ti edges in TiO_2-B, the ones in both Ca:TiO_2-B and STO definitely show the two distinct t_{2g} and e_g peaks in each edge, demonstrating almost no Li intercalation occurred in these regions.

5.4. Conclusion

In summary, we have discovered a relaxation mechanism of TiO_2-B via in-situ TEM lithiation experiments performed on a thin film. Depending on Li intercalation direction into TiO_2-B, $LiTi_2O_4$-B relaxes its structure locally in different ways, either by simple shearing or shear induced lower-order phase transformation. From the results, we also identified the interesting structural similarity to the as-grown TiO_2-B film demonstrated in Chapter 4. This unique finding on structural relaxation upon Li insertion enriches the knowledge on intercalation chemistry of one of the promising anode materials and leads to more understanding of electro-chemical processes of thin-film Li-ion cell devices.

5.5. References

1. R. Marchand, L. Brohan, M. Tournoux, "TiO_2(B) a new form of titanium dioxide and the potassium octatitanate $K_2Ti_8O_{17}$", *Mater. Res. Bull.* **15** 1129-1133 (1980)

2. D. Deng, M. G. Kim, J. Y. Lee, J. Cho, "Green energy storage materials: Nanostructured TiO_2 and Sn-based anodes for lithium-ion batteries", *Energy Environ. Sci.* **2** 818-837 (2009)

3. M. Tournoux, R. Marchand, L. Brohan, "Layered $K_2Ti_4O_9$ and the open metastable TiO_2(B) structure", *Prog. Solid State Chem.* **17** 33-52 (1986)

4. M. Zukalová, M. Kalbáč, L. Kavan, I. Exnar, M. Graetzel, "Pseudocapacitive Lithium Storage in TiO_2(B)", *Chem. Mater.* **17** 1248-1255 (2005)

5. A. R. Armstrong, G. Armstrong, J. Canales, R. García, P. G. Bruce, "Lithium-Ion Intercalation into TiO_2-B Nanowires", *Adv. Mater.* **17** 862-865 (2005)

6. A. R. Armstrong, C. Arrouvel, V. Gentili, S. C. Parker, M. S. Islam, P. G. Bruce, "Lithium Coordination Sites in Li_xTiO_2(B): A Structural and Computational Study", *Chem. Mater.* **22** 6426-6432 (2010)

7. B. Zachau-Christiansen, K. West, T. Jacobsen, S. Atlung, "Lithium insertion in different TiO_2 modifications", *Solid State Ionics* **28–30, Part 2** 1176-1182 (1988)

8. G. Armstrong, A. R. Armstrong, J. Canales, P. G. Bruce, "Nanotubes with the TiO_2-B structure", *Chem. Commun.* 2454-2456 (2005)

9. V. Etacheri, Y. Kuo, A. Van der Ven, B. M. Bartlett, "Mesoporous TiO_2-B microflowers composed of (1 -1 0) facet-exposed nanosheets for fast reversible lithium-ion storage", *J. Mater. Chem. A* **1** 12028-12032 (2013)

10. A. R. Armstrong, G. Armstrong, J. Canales, P. G. Bruce, "TiO_2-B Nanowires", *Angew. Chem. Int. Ed.* **43** 2286-2288 (2004)

11. Y. Ren, Z. Liu, F. Pourpoint, A. R. Armstrong, C. P. Grey, P. G. Bruce, "Nanoparticulate TiO_2(B): An Anode for Lithium-Ion Batteries", *Angew. Chem. Int. Ed.* **124** 2206-2209 (2012)

12. C. Arrouvel, S. C. Parker, M. S. Islam, "Lithium Insertion and Transport in the TiO_2−B Anode Material: A Computational Study", *Chem. Mater.* **21** 4778-4783 (2009)

13. A. G. Dylla, G. Henkelman, K. J. Stevenson, "Lithium Insertion in Nanostructured TiO_2(B) Architectures", *Acc. Chem. Res.* **46** 1104-1112 (2013)

14. A. S. Dalton, A. A. Belak, A. Van der Ven, "Thermodynamics of Lithium in TiO_2(B) from First Principles", *Chem. Mater.* **24** 1568-1574 (2012)

15. B. J. Morgan, P. A. Madden, "Lithium intercalation into TiO_2(B): A comparison of LDA, GGA, and GGA+*U* density functional calculations", *Phys. Rev. B* **86** 035147 (2012)

16. M. V. Koudriachova, "Role of the surface in Li insertion into nanowires of TiO_2-B", *Surf. Interface Anal.* **42** 1330-1332 (2010)

17. T. Okumura, T. Fukutsuka, A. Yanagihara, Y. Orikasa, H. Arai, Z. Ogumi, Y. Uchimoto, "Nanosized Effect on Electronic/Local Structures and Specific Lithium-Ion Insertion Property in TiO_2–B Nanowires Analyzed by X-ray Absorption Spectroscopy", *Chem. Mater.* **23** 3636-3644 (2011)

18. T. Okumura, T. Fukutsuka, A. Yanagihara, Y. Orikasa, H. Arai, Z. Ogumi, Y. Uchimoto, "Electronic and local structural changes with lithium-ion insertion in TiO_2-B: X-ray absorption spectroscopy study", *J. Mater. Chem.* **21** 15369-15377 (2011)

19. M. Fehse, M. Ben Yahia, L. Monconduit, F. Lemoigno, M.-L. Doublet, F. Fischer, C. Tessier, L. Stievano, "New Insights on the Reversible Lithiation Mechanism of TiO_2(B) by Operando X-ray Absorption Spectroscopy and X-ray Diffraction Assisted by First-Principles Calculations", *J. Phys. Chem. C* **118** 27210-27218 (2014)

20. D. Chang, *Ph. D. Thesis*, "Elucidating the origins of hysteresis and reaction mechanisms of electrode materials for Li and Na batteries", Materials Science and Engineering, University of Michigan, (2015)

21. M. J. Hÿtch, E. Snoeck, R. Kilaas, "Quantitative measurement of displacement and strain fields from HREM micrographs", *Ultramicroscopy* **74** 131-146 (1998)

22. S.-W. Cheong, "Transition metal oxides: The exciting world of orbitals", *Nat. Mater.* **6** 927-928 (2007)

23. H. Zheng, Y. Liu, S. X. Mao, J. Wang, J. Y. Huang, "Beam-assisted large elongation of in situ formed Li_2O nanowires", *Sci. Rep.* **2** (2012)

24. X. H. Liu, J. W. Wang, Y. Liu, H. Zheng, A. Kushima, S. Huang, T. Zhu, S. X. Mao, J. Li, S. Zhang, W. Lu, J. M. Tour, J. Y. Huang, "In situ transmission electron microscopy of electrochemical lithiation, delithiation and deformation of individual graphene nanoribbons", *Carbon* **50** 3836-3844 (2012)

25. X. Wang, D.-M. Tang, H. Li, W. Yi, T. Zhai, Y. Bando, D. Golberg, "Revealing the conversion mechanism of CuO nanowires during lithiation-delithiation by in situ transmission electron microscopy", *Chem. Commun.* **48** 4812-4814 (2012)

26. D. Panduwinata, J. D. Gale, "A first principles investigation of lithium intercalation in TiO_2-B", *J. Mater. Chem.* **19** 3931-3940 (2009)

27. R. J. Cava, D. W. Murphy, S. Zahurak, A. Santoro, R. S. Roth, "The crystal structures of the lithium-inserted metal oxides $Li_{0.5}TiO_2$ anatase, $LiTi_2O_4$ spinel, and $Li_2Ti_2O_4$", *J. Solid State Chem.* **53** 64-75 (1984)

28. K. Zhang, M. B. Katz, B. Li, S. J. Kim, X. Du, X. Hao, J. R. Jokisaari, S. Zhang, G. W. Graham, A. Van der Ven, B. M. Bartlett, X. Pan, "Water-Free Titania–Bronze Thin Films with Superfast Lithium-Ion Transport", *Adv. Mater.* **26** 7365-7370 (2014)

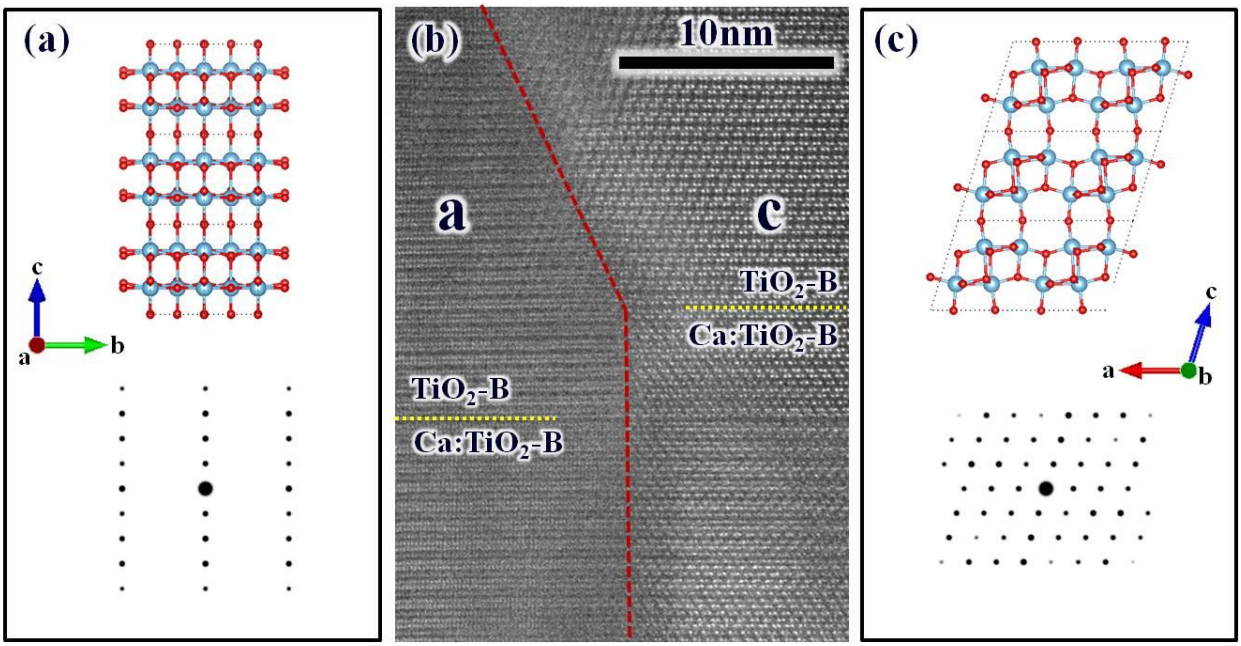

Figure 5.1 Schematic representations and corresponding simulated electron diffraction patterns of TiO_2-B lattice projected along **a**. [100] and **c.** [010] direction. Ti and O atoms are drawn in blue and red, respectively. **b.** HRSTEM image showing the interfacial boundary between the two grains with (100) and (010) planes exposed to the cross-sectional surface.

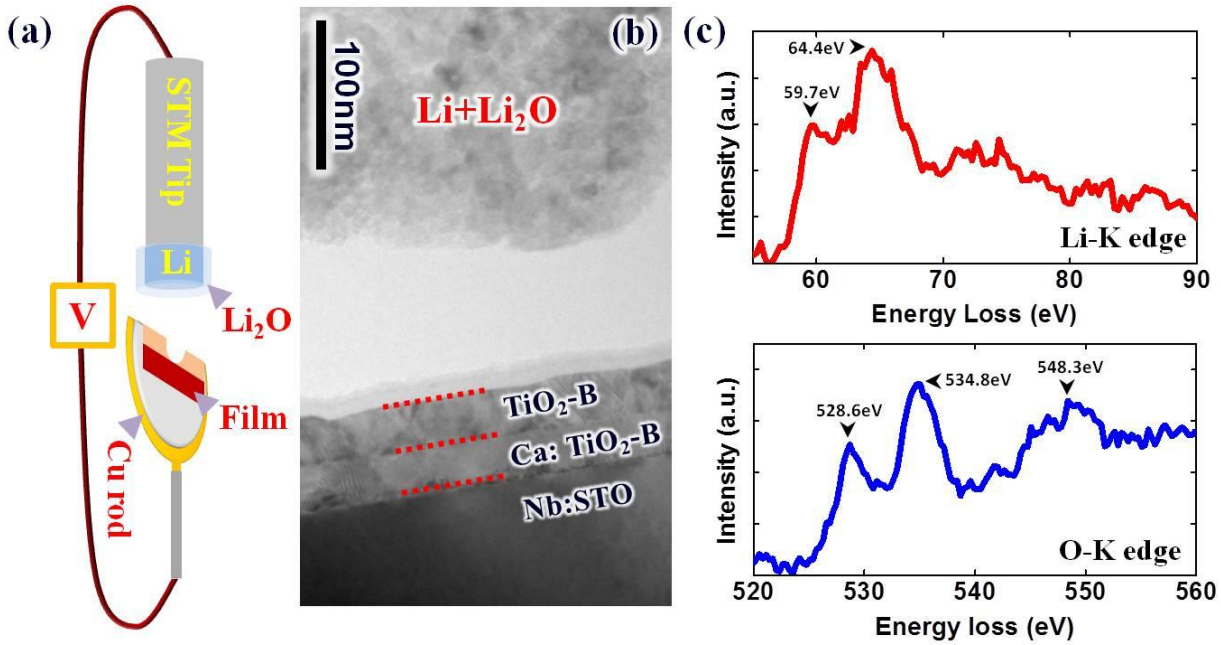

Figure 5.2 a. A schematic and **b.** a TEM image of a set-up for an in-situ Li-ion cell inside TEM, and **c.** electron energy loss spectroscopy of Li STM tip demonstrating the existence of both Li and O.

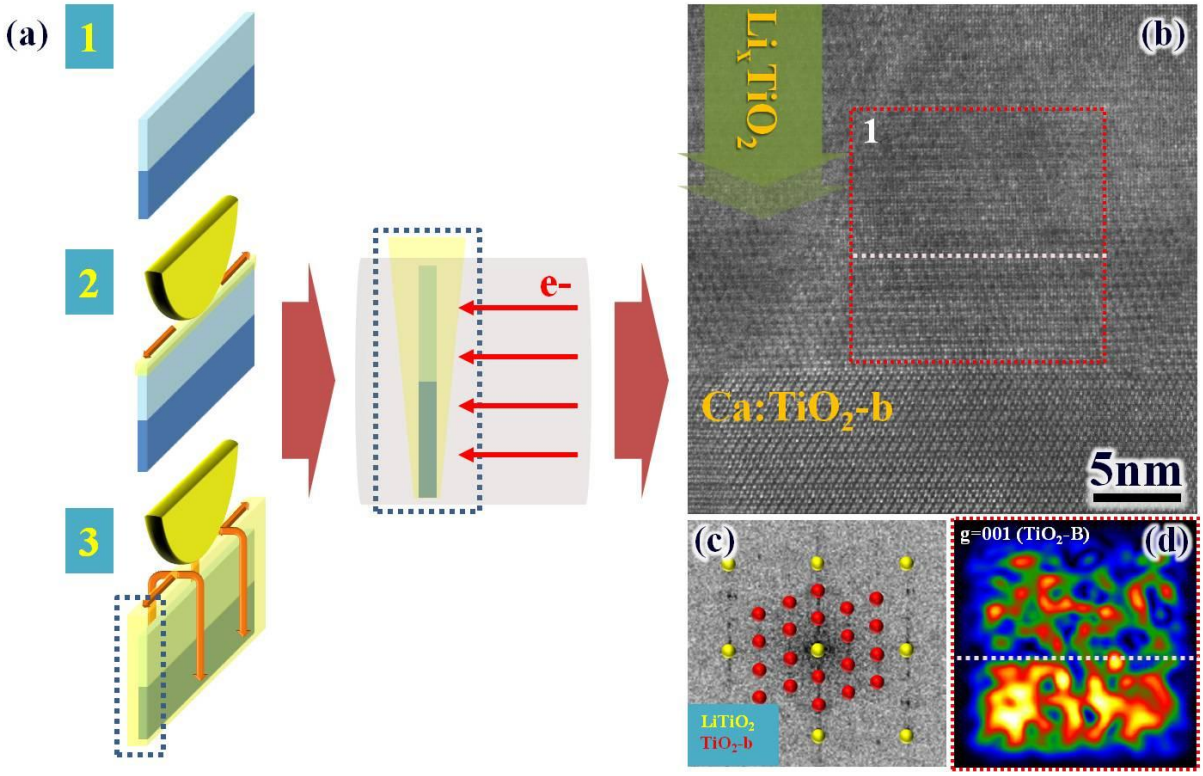

Figure 5.3 a. The schematic showing the sequence of Li ion wetting on the cross-sectional TEM specimen, and **b and c.** high resolution STEM image and a corresponding FFT pattern demonstrating the effect of an electron beam on a Li wetted sample. **d.** A phase map from region 1 showing the gradual transition of TiO_2-B to Li_xTiO_2.

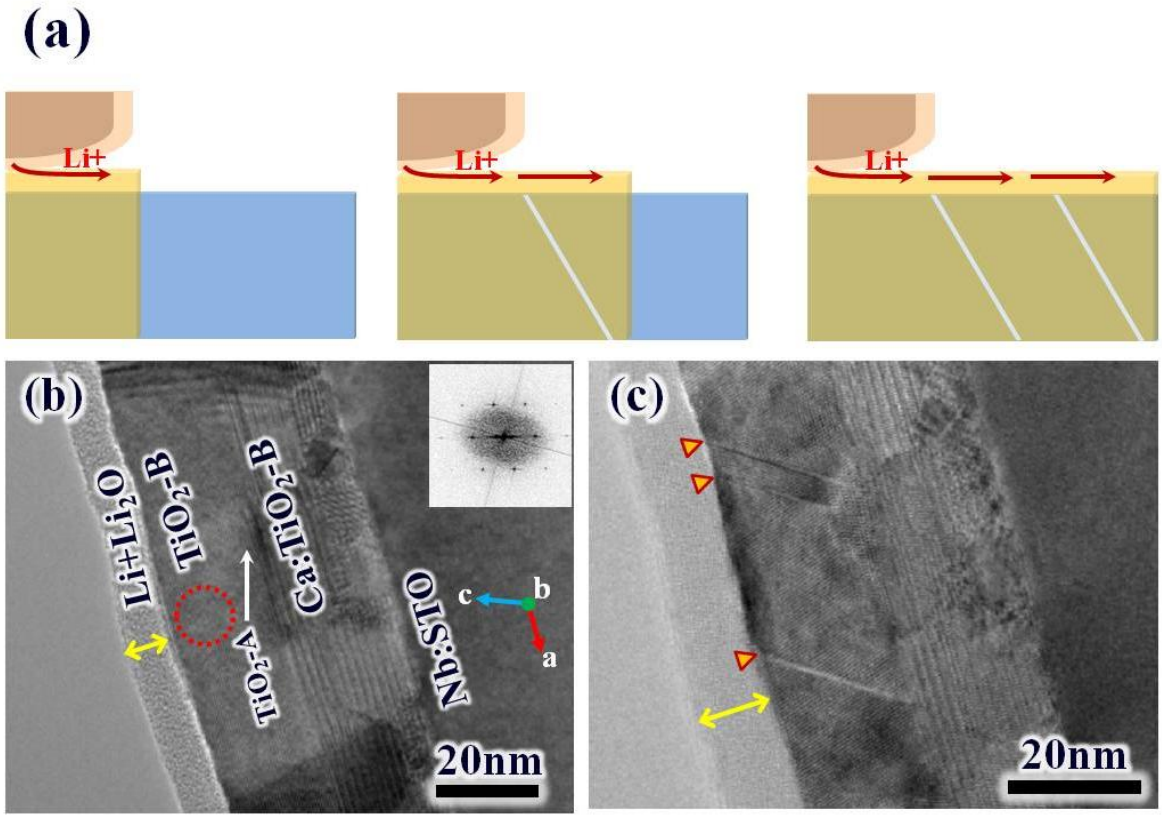

Figure 5.4 a. A schematic demonstrating sequence of defect generation upon lateral Li propagation on a film's cross-sectional surface. **b and c.** High-resolution TEM Image of a TiO_2-B thin film before and after lithiation. Arrows indicate the structural changes observed in the structure during lithiation. The inset in **b** shows the FFT pattern of the region marked with red.

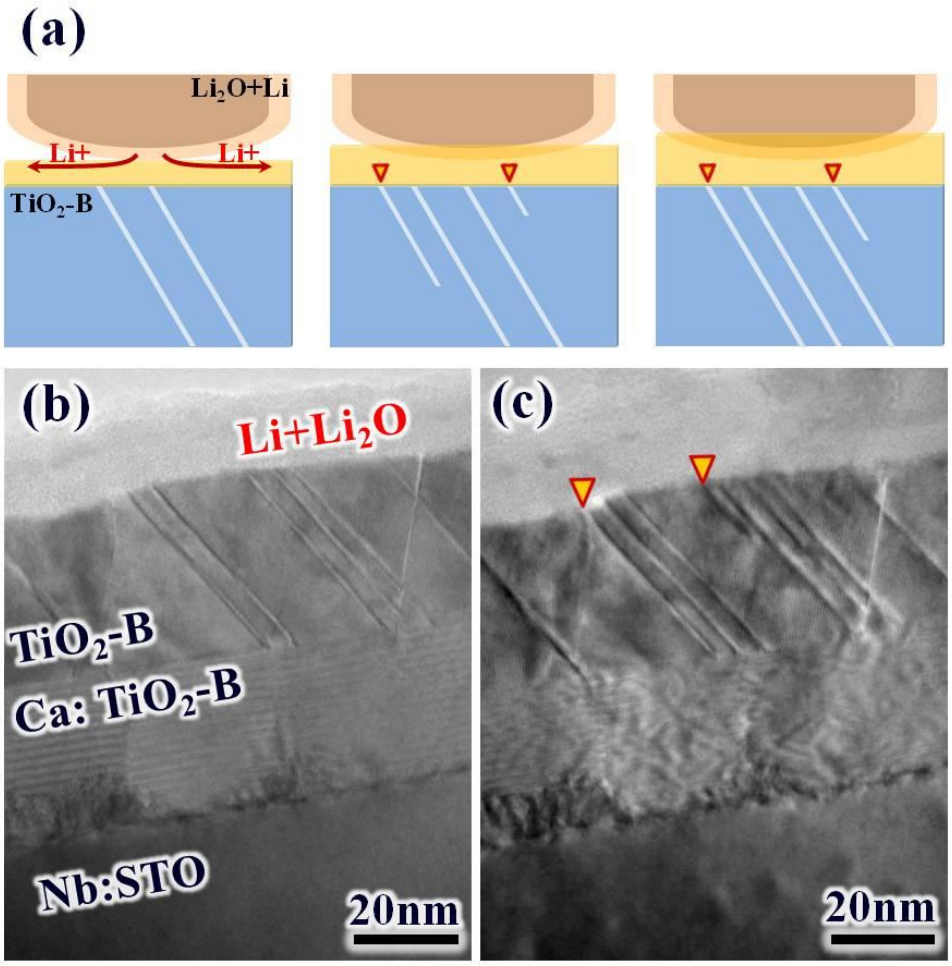

Figure 5.5 a. Schematics of Li insertion at the direct contact between Li STM tip and the film. TEM Images of a TiO_2-b and Ca:TiO_2 dual-layer film **b.** before and **c.** after for additional lithium insertion. More pathways are likely to be generated under prolonged lithiation. (Arrows) Note that Ca:TiO_2-B layer is unaffected during lithiation.

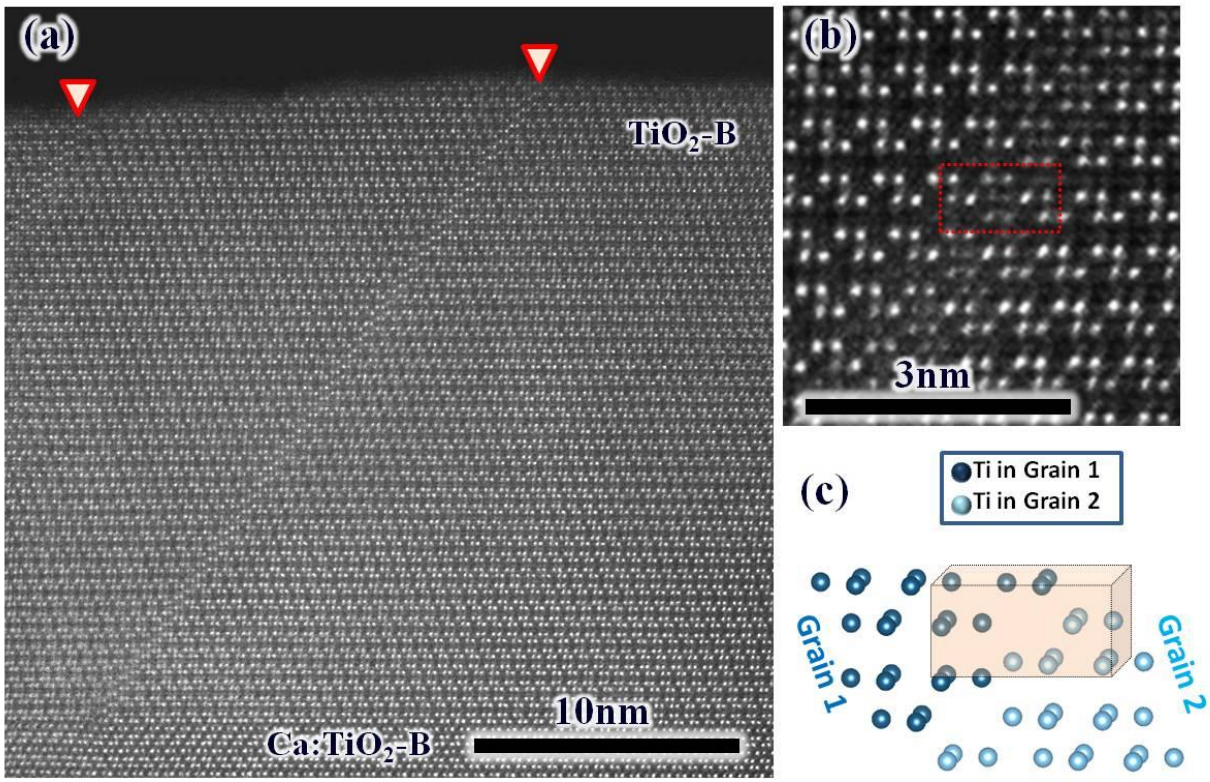

Figure 5.6 a. High resolution STEM and **b.** magnified STEM images of a lithiated TiO_2-B layer. **c.** A 3-dimensional schematic showing microstructural shearing of TiO_2-B upon lithiation.

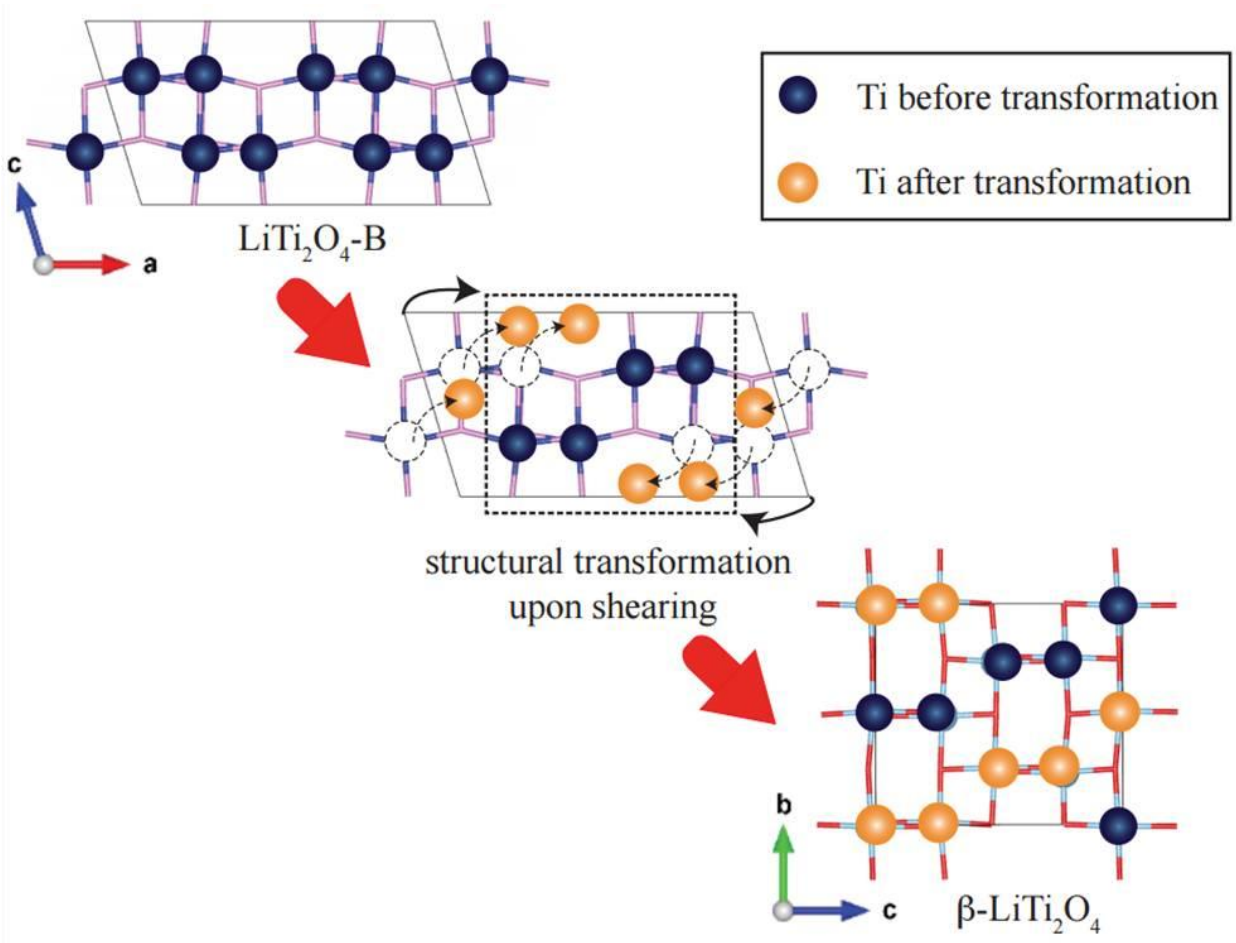

Figure 5.7 The structural relationship between $LiTi_2O_4$-B and β-$LiTi_2O_4$ before and after shear-induced structural transformation. Li atoms are omitted to show clearly the configuration of Ti and O ordering upon structural transformation. [Image Courtesy: Donghee Chang from the Anton Van der Ven's group]

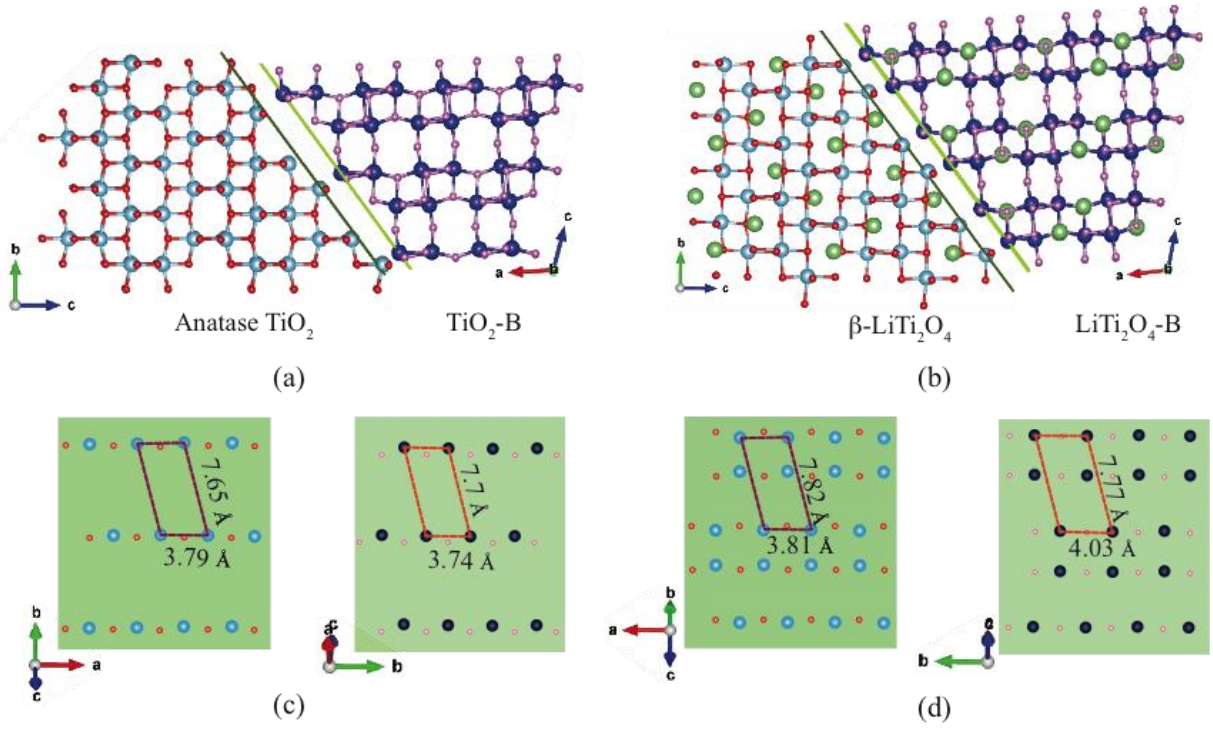

Figure 5.8 The schematic illustration of the interfacial relationship along the habit plane upon **a.** pure anatase TiO_2 phase inclusion in TiO_2-B phase and **b.** β-$LiTi_2O_4$ phase inclusion in $LiTi_2O_4$-B. The comparisons of ordering of Ti and O atoms at the habit plane for **c.** pure anatase TiO_2 and TiO_2-B and **d.** b-$LiTi_2O_4$ and $LiTi_2O_4$-B are also illustrated. [Image Courtesy: Donghee Chang from the Anton Van der Ven's group]

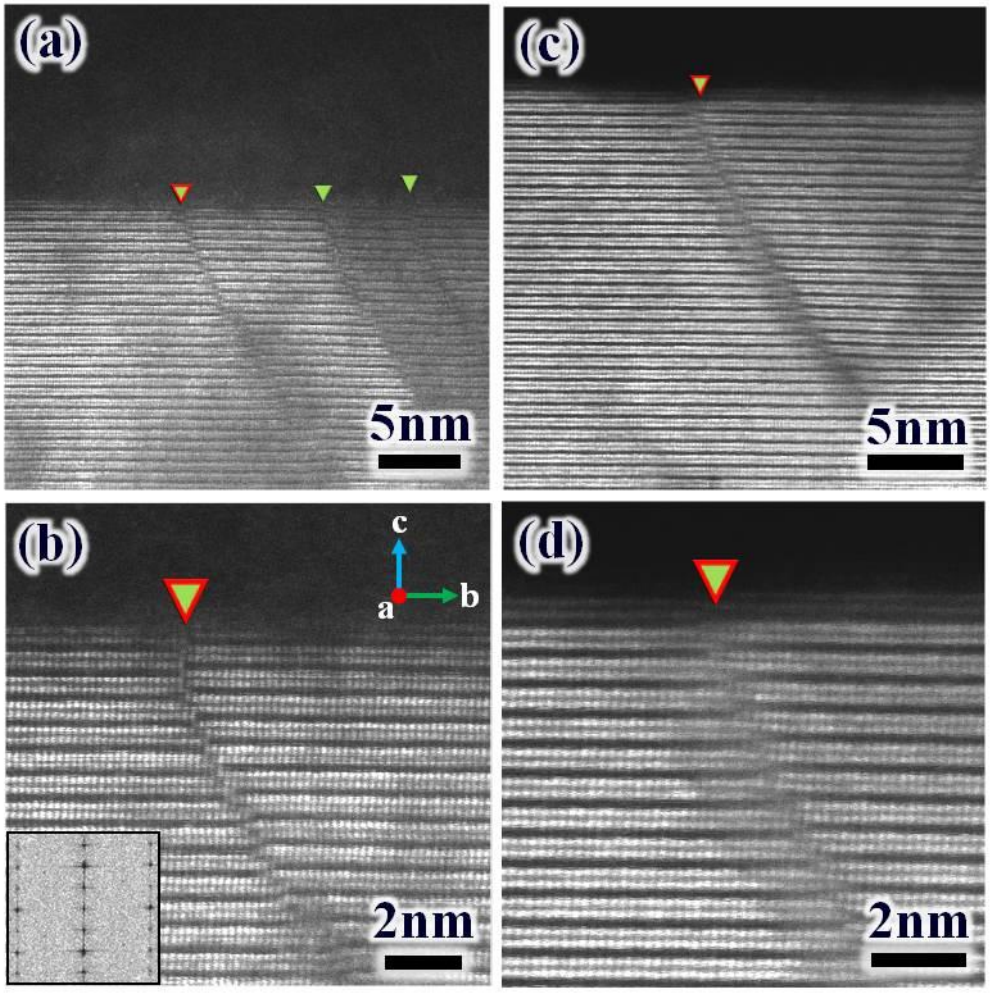

Figure 5.9 High-resolution TEM images demonstrating *c*-axis shearing of a TiO_2-B plane shown along [100] after **a and b.** in-situ and **c and d.** ex-situ electro-chemical cycling. The inset in **b.** shows the FFT pattern of the region.

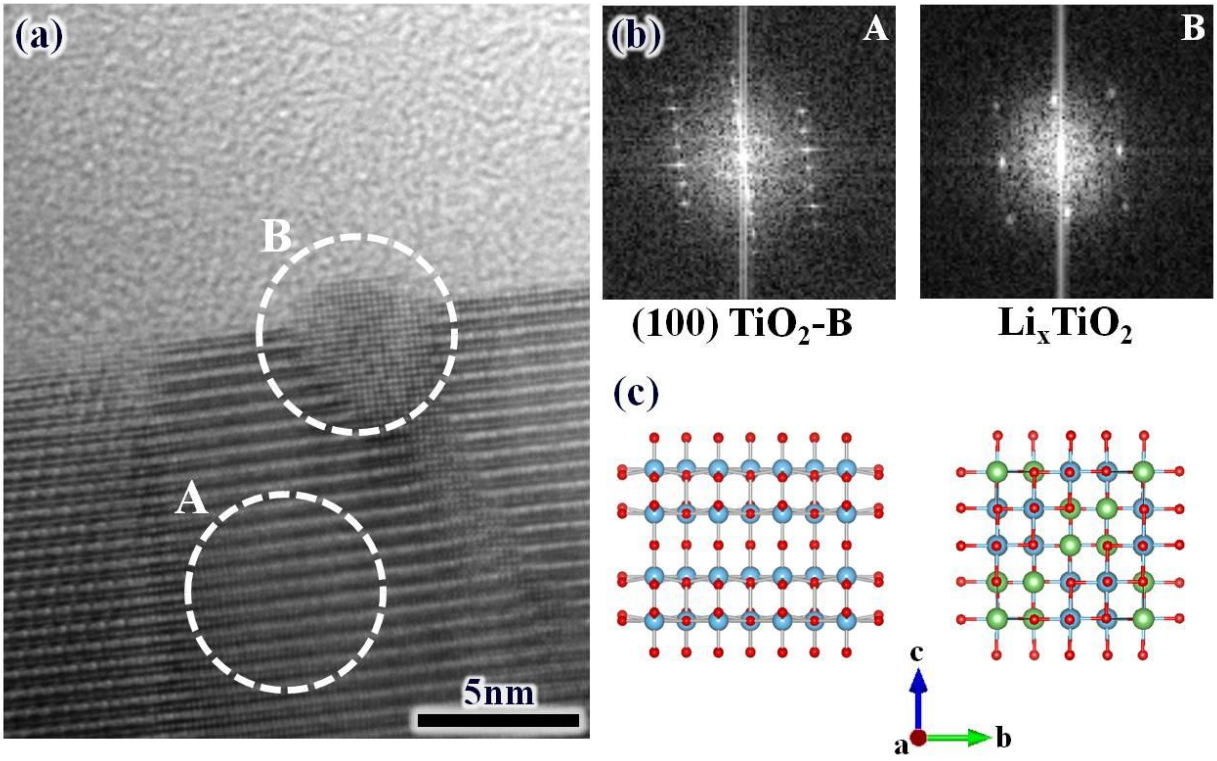

Figure 5.10 a. HR-TEM image and **b.** selected-area diffraction patterns, demonstrating the formation of B: spinel Li_xTiO_2 at the top of the shear within the A: regular TiO_2-B film, and **c.** corresponding atomic models of TiO_2-B and Li_xTiO_2.

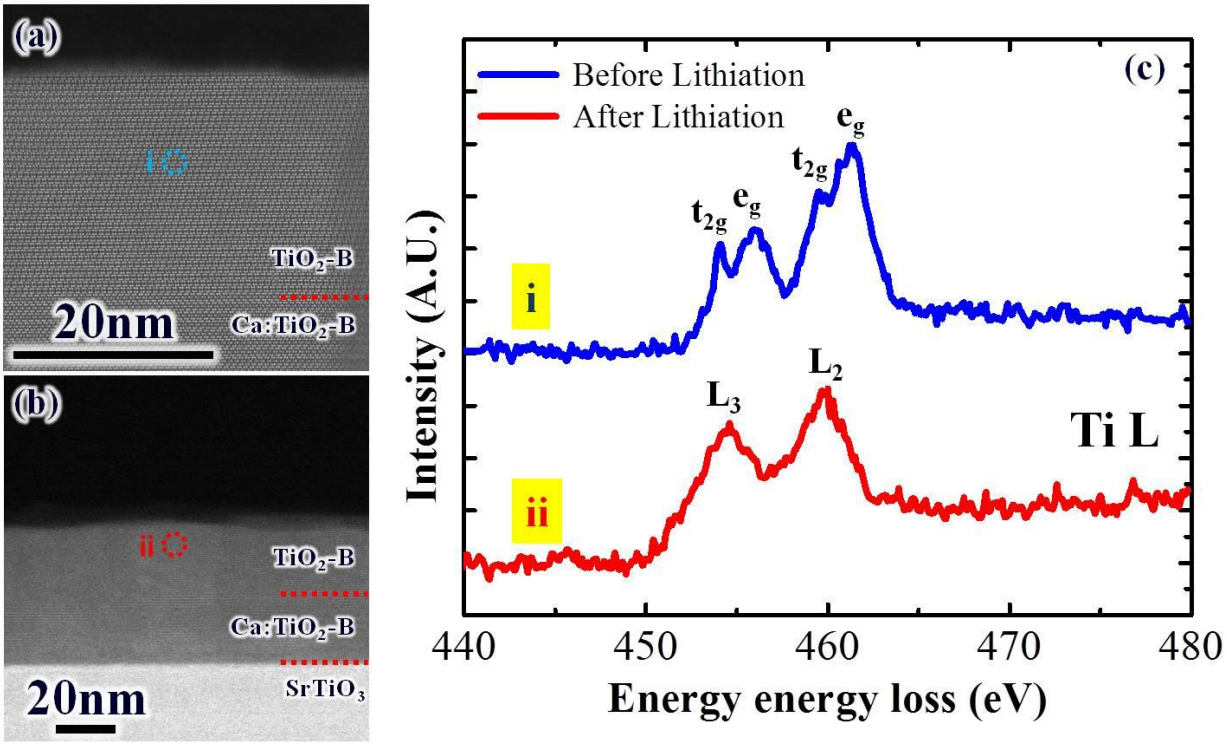

Figure 5.11 High-resolution TEM images demonstrating a TiO_2-B film **a.** before and **b.** after full lithiation. **c.** EELS Spectra on the regions marked with circles in both **a** and **b** demonstrate the shift of a valence state of Ti from Ti^{4+} to Ti^{3+} upon full lithiation.

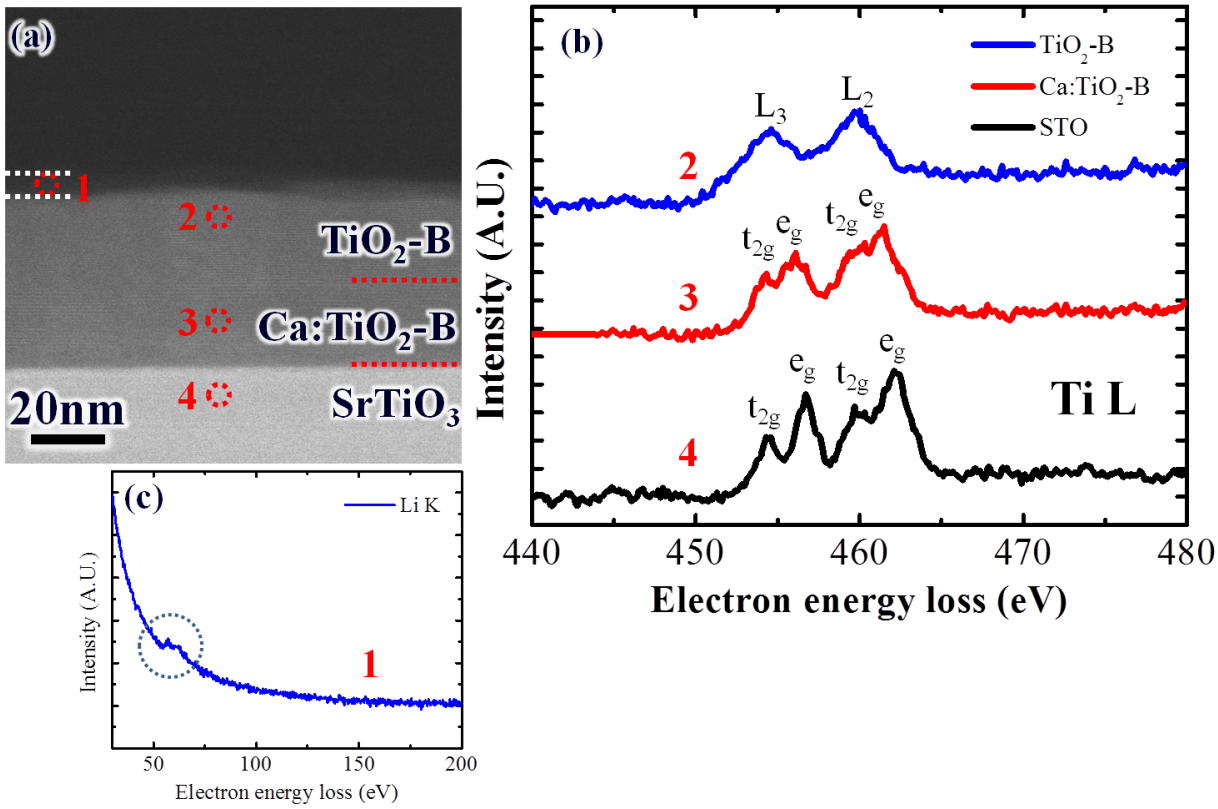

Figure 5.12 a. HR-STEM image of a TiO_2-B thin film after lithiation, **b.** EELS near edge spectra of Ti K for TiO_2-B, Ca:TiO_2-B, and STO, and **c.** an edge spectrum of Li K that wets the top surface of the film.

Chapter 6. TEM Study on the effect of rutile TiO_2 coating upon lithiation of p-Si NWs

6.1. Introduction and Background

Increasing demand for effective energy storage has triggered a tremendous interest in high energy-density electrodes for lithium ion batteries. Commercialized lithium ion batteries with graphite as the anode have been extensively used in mobile devices. However, a new system with higher capacity and energy density is needed for hybrid electric vehicles (HEVs), plug-in hybrid electric vehicles (PHEVs), and a high power grid system.[1] Silicon is considered promising due to its high theoretical gravimetric capacity of 4200 $mAhg^{-1}$, which greatly surpasses that of graphite (372 $mAhg^{-1}$).[2] However, the application of Si has been proved challenging due to pulverization associated with a large volumetric change of 300% during lithium insertion/extraction, leading to capacity loss.[3] To overcome this problem, various approaches such as morphology control,[4] carbon-coating,[5-8] and use of polymer/organic binders,[9-10] as well as active-inactive composites[11-16] have been studied.

Surface coating of Si nanowires (NWs) by the native silicon oxide (SiO_x) has recently been proposed by Cho[14-15] and Cui[17] and their co-workers. The SiO_x shell not only enhances mechanical stability of a Si NW, but it also prevents formation of new solid electrolyte interphase (SEI), hence improving capacity retention. Other metal oxides like ZrO_2, Al_2O_3, and

TiO_2 have also been considered as coating layers for lithiated Si NWs based on their different potential ranges relative to Si and thermal stabilities under SEI formation.[11-13,16] However, increasing thickness of a coating contributes to capacity fading and decreases coulombic efficiency due to the compressive stress on the Si core, making lithiation thermodynamically limited. Nevertheless, an optimized thickness of coating of an anode may sustain a longer battery life in exchange for its initial capacity being reduced.

Despite extensive study of inert oxide layers on a Si NW, understanding of lithium ion transportation through the coated Si NW is still incomplete. In many ex-situ studies, the indirect observation and quantification of Li intercalation has proved difficult due to heavy incorporation of carbon needed to encapsulate the oxide coated NW for conductivity enhancement.[18] The added carbon not only obscures the migration path of lithium, since intercalation may happen in both Si and C, but it also fails to suppress large exothermic reactions between Li_xSi and the electrolyte at high temperature.[19] In contrast, an in-situ technique, where the electrochemical device is assembled inside a TEM, for example, offers a unique opportunity to scrutinize structural changes associated with lithium intercalation into a complex nanostructured system. Here, using this technique, it is demonstrated for the first time how lithium intercalates into a Si NW coated with a semi-inert TiO_2 layer of varying thickness. Hence, this study examines how TiO_2 coating affects the final morphology of the inner silicon core and the resulting dimension of the entire NW during Li intercalation by varying the coating thickness-to-NW-diameter ratio (i.e. t/D ratio).

6.2. Experimental Procedures

Si NW arrays were fabricated on a n-Si wafer via an aqueous Ag-assisted electroless etching method. The P doping level was ~$10^{15}cm^{-3}$. A uniform TiO_2 coating was deposited onto the Si NWs via atomic-layer deposition (ALD), allowing precise control over the layer thickness. Both the crystallinity and uniformity of thickness of TiO_2 used in these studies were examined under a high-resolution transmission electron microscope (HR-TEM, JEOL JEM-3010F) and a scanning transmission electron microscope (HR-STEM, JEOL JEM-2100F).

A TEM specimen for TiO_2-coated Si NWs was prepared by the method already explained in Chapter 2. A prepared specimen was loaded onto a single-tilt in-situ Nanofactory Instruments TEM-STM holder, comprising half of an electro-chemical cell assembly in a JEOL JEM-3010F microscope. The complete set-up electro-chemical assembly was performed in a manner similar to that explained in Chapter 3. Lithiation and delithiation were performed under potentiostatic mode by applying a constant voltage across the electrodes. Due to large contact resistance and heterogeneity between the NW and Li (held on the STM tip), any potential and current measurement during the lithiation process is not reliable, so TEM SAED was used to confirm structural changes observed within the Si NW, especially a crystalline-to-amorphous phase transformation. The extent of lithiation was qualitatively determined by the location of the Li NW reaction front that is driven across the entire NW.

6.3. Results and Discussion

6.3.1 Characterization of a TiO_2-coated Si NW

In this study, a rutile polymorph of TiO_2 was selected as the coating material since, upon lithiation, it turns electrically conductive in certain extent to effectively enhance the electrical conduction to Si and undergoes only a 4% lattice expansion, effectively limiting the volumetric expansion of a Si NW. Figure 6.1a shows the Si NW coated with multi-crystalline TiO_2. The NW is oriented along the [001] direction, as confirmed by SAED (Figure 6.1b). The EELS line scan across the NW (Figure 6.1c) shows that the coating of TiO_2 around Si is uniform. Both BF TEM and DF STEM micrographs (Figures 6.1d and e) of TiO_2/Si interfaces show that the Si NW does not undergo chemical reaction with TiO_2 during coating. The coating thickness of TiO_2 is either 10 nm or 30 nm, and the NW diameter varies over the range 65-220 nm. Individual grain dimension within the TiO_2 coating varies in width but is uniform in height.

6.3.2 In-situ lithiation of a TiO_2-coated Si NW under TEM

Figures 6.2a and b illustrate the open prototype electrochemical cell that was constructed inside a TEM by loading a TiO_2-coated Si NW as one electrode and Li metal as the counter-electrode. The naturally formed Li_2O layer on the Li metal surface, also identified in the characteristic near-edge signal of Li K from EELS on the edge of a Li-coated STM tip (Figure 6.2c), was considered a solid electrolyte for Li ion transport. Upon contacting, the potential of -4V and 4V relative to the Li metal electrode was applied to the NWs for lithiation and delithiation.

A similar type of experiments was already performed on pristine phosphorous-doped Si NWs via in-situ TEM by Huang and co-workers with an electrochemical set-up similar to that used in this study.[3] Their study shows the rapid migration of Li ions along the surface of a NW, followed by diffusion into Si from the side to form an amorphous Li_xSi shell. The interfacial boundary between the amorphous Li_xSi shell and crytalline Si core moves radially inward via continuous phase transformation (e.g., $Si + Li^+ + e^- \rightarrow Li_xSi$), causing radial expansion to happen more rapidly than axial expansion. Interestingly, this radial lithiation reaches a kinetic limitation such that after a certain period of time, it no longer proceeds due to the insufficient reservoir of electrons from along the contracted Si NW core. This prevents the Si NW from reaching full lithiation.[3]

On the other hand, the axial migration of Li ions along the surface of a TiO_2-coated Si NW is also expected to be fast, but radial penetration of Li into the NW should be somewhat limited by the presence of the semi-inert coating layer. Figures 6.3a, b, and c show sequential images of Li ion migration into a Si NW with TiO_2 coating (t/D=0.23) during lithiation. Li ions first enter Si through a (100) facet in contact with the Li source, inducing radial expansion due to expansion along the [110] orientation.[20] As the NW expands radially, the TiO_2 coating fractures and begins to peel off, until the entire Si core reaches full lithiation, as shown in Figures 6.3d and e. The change in SAED pattern upon lithiation (Figures 6.3f and g) provides a clear indication of the lithiated Si phase, $Li_{15}Si_4$, corresponding to full lithiation. We note that the coated NW after lithiation has undergone average radial and axial expansions of ~248% and 108%, respectively. The local radial expansion varies, however, with a maximum of only 270%, since lithiation has been limited by remnants of the TiO_2 coating. Since the coating is polycrystalline, variation in grain-to-grain bonding along the NW allows weaker bonding to generate a higher chance for

cracks to initiate and propagate. Hence, the strength of bonding within TiO_2 influences the overall morphology phases found in the lithiated Si NW.

It is interesting to note that, during the lithiation of this composite NW, there is no significant change in dimension of the TiO_2 coating, implying that it functions as an effective buffer upon lithiation of Si. To prove this, an additional experiment was performed on a closed-ended NW (also capped by TiO_2) instead of an open-ended one under experimental conditions (Figure not shown). Even after a long lithiation period, no significant change was observed.

The average propagation speed of the reaction front for a pristine p-doped Si NW was found to be approximately 14 nm/s, ~10 times faster than in an undoped Si NW. This is comparable to the speed observed in an uncoated phosphorous-doped Si NW.[3] The speed of lithium migration in a coated NW, however, varies from NW to NW during lithiation due to variations in coating, i.e., the presence of differently sized and shaped grains. Lithium ion diffusion can even be blocked at certain points in time of lithiation if the interfacial bonding between TiO_2 and Si is robust enough to initially constrain the diffusion of lithium. Hence, Li ions that are originally migrating along the NW surface are driven inward instead, making sure that each segment of the Si NW is fully lithiated. Hence, the full degree of lithiation can be achieved locally by continuously diverting Li ions inside a NW by having a TiO_2 shell interrupting their surface migration. During this first stage of lithiation, the hydrostatic stress from a lithiated NW builds up due to continuous feeding of Li ions that induces volumetric expansion as indicated from complete amorphorization of the Si core (see schematic in Figure 6.4) followed by crystallization to c-$Li_{15}Si_4$, which has lower energy of formation than the amorphous phase, Li_xSi.[21] This leads to further tearing of TiO_2 coating from the core, allowing Li ions to initiate and repeat the process in adjacent segments of the NW until the entire coating is full of cracks. The details of this segmented lithiation are well

illustrated in Figure 6.5. Note that the length of each segment varies according to the presumed bonding strength between TiO_2 and Si. This fully lithiated NW, upon delithiation, performed by applying +4V relative to Li metal, contracts both radially and axially by 21% and 3%, respectively, clearly showing some degree of integrity of the NW despite seemingly large structural reversibility (Figure 6.6). The use of more ionically conductive liquid electrolyte and incorporation of carbon improve Li extraction from the Si NW.[21-22] (also see Appendix A)

While the TiO_2 coating appears to promote lithiation along the axial direction in this instance, the lithiation behavior is in fact a function of coating thickness. Here, another NW, with t/D=0.08, was also tested to observe lithiation behavior of a Si NW with thinner TiO_2 coating. Since the strength of bonding between TiO_2 grains is relatively weaker, compared to the tensile stress arising from lithiation of the Si NW core in the case with t/D=0.23, lithiation proceeds smoothly throughout the NW, with little effect of the TiO_2 coating. The final morphology after full lithiation is quite uniform throughout, similar to that of the uncoated NW, as shown in Figures 6.7a-c. This is very different from the NW with thicker coating that shows very rough surface profile (Figure 6.7d-f). This shows that an excessively thin coating has almost no mechanical influence on the NW lithiation, since the entire lithiated NW has undergone significant contraction in length (~28%) and only slightly less radial expansion than the uncoated one. The comprehensive plot in Figure 6.8a demonstrates the effect of the relative coating thickness (t/D) on the average radial expansion of the coated NW, based on four different NW measurements. From the plot, it is apparent that the thicker coating can suppress the NW core from expanding and somewhat maintain the integrity of a Si NW, again likely due to the stronger bonding between grains of the TiO_2 coating. In addition to the average radial expansion, average axial elongation of the coated NW upon lithiation is also plotted against t/D. A coated NW with higher

t/D ratio tends to remain more elongated than one with lower ratio, due to the segmented lithiation. The overall difference in the lithiated morphology of the coated NW for both low and high t/D ratio is illustrated in Figures 6.8b and c and agrees well with that suggested by Cui and co-workers from their work on ex-situ electrochemical lithiation of a coated Si NW.[17] Their work, which was also performed under potentiostatic mode, involved lithiating a batch of coated Si NWs and extracting comparative statistics of these NW dimensions before and after lihiation. They concluded that coated Si NWs with lower t/D ratio exhibit both radial expansion and contraction in length upon lithiation. However, for NWs with higher t/D ratio, they observed a slight increase in both the length and diameter upon lithiation, despite that the degree of radial expansion is still more significant than that of axial expansion, in agreement with our in-situ results[17].

6.4. Conclusions

In summary, The nano-scale effect of TiO_2 coating on the morphological changes of a Si NW was observed upon full lithiation by in-situ TEM. Coatings with sufficiently large t/D ratio induce segmented lithiation that promotes axial Li ion migration during transformation of Si to $Li_{15}Si_4$. Hence, the overall morphology of the coated Si NW upon full lithiation shows less radial expansion, as well as reduced axial contraction, than. These results confirm the effect of coating Si NWs with inert, or semi-inert oxide layers on lithiation, which may lead to a more optimized morphology control of Si nanostructures that can better accommodate anisotropy, thus improving the performance of Si as a Li-ion battery anode, while providing insight into the dynamics that occur during the lithiation process.

6.5. References

1. M. Armand, J. M. Tarascon, "Building better batteries", *Nature* **451** 652-657 (2008)

2. A. S. Arico, P. Bruce, B. Scrosati, J.-M. Tarascon, W. van Schalkwijk, "Nanostructured materials for advanced energy conversion and storage devices", *Nat. Mater.* **4** 366-377 (2005)

3. X. H. Liu, L. Q. Zhang, L. Zhong, Y. Liu, H. Zheng, J. W. Wang, J.-H. Cho, S. A. Dayeh, S. T. Picraux, J. P. Sullivan, S. X. Mao, Z. Z. Ye, J. Y. Huang, "Ultrafast Electrochemical Lithiation of Individual Si Nanowire Anodes", *Nano Lett.* **11** 2251-2258 (2011)

4. Y. Park, N.-S. Choi, S. Park, S. H. Woo, S. Sim, B. Y. Jang, S. M. Oh, S. Park, J. Cho, K. T. Lee, "Si-Encapsulating Hollow Carbon Electrodes via Electroless Etching for Lithium-Ion Batteries", *Adv. Energy Mater.* **3** 206-212 (2013)

5. J. Shu, H. Li, R. Yang, Y. Shi, X. Huang, "Cage-like carbon nanotubes/Si composite as anode material for lithium ion batteries", *Electrochem. Commun.* **8** 51-54 (2006)

6. L. Luo, J. Wu, J. Luo, J. Huang, V. P. Dravid, "Dynamics of Electrochemical Lithiation/Delithiation of Graphene-Encapsulated Silicon Nanoparticles Studied by In-situ TEM", *Sci. Rep.* **4** (2014)

7. L.-F. Cui, Y. Yang, C.-M. Hsu, Y. Cui, "Carbon−Silicon Core−Shell Nanowires as High Capacity Electrode for Lithium Ion Batteries", *Nano Lett.* **9** 3370-3374 (2009)

8. T. D. Bogart, D. Oka, X. Lu, M. Gu, C. Wang, B. A. Korgel, "Lithium Ion Battery Peformance of Silicon Nanowires with Carbon Skin", *ACS Nano* **8** 915-922 (2013)

9. B. Koo, H. Kim, Y. Cho, K. T. Lee, N.-S. Choi, J. Cho, "A Highly Cross-Linked Polymeric Binder for High-Performance Silicon Negative Electrodes in Lithium Ion Batteries", *Angew. Chem., Int. Ed* **51** 8762-8767 (2012)

10. I. Kovalenko, B. Zdyrko, A. Magasinski, B. Hertzberg, Z. Milicev, R. Burtovyy, I. Luzinov, G. Yushin, "A Major Constituent of Brown Algae for Use in High-Capacity Li-Ion Batteries", *Science* **334** 75-79 (2011)

11. A. Kohandehghan, P. Kalisvaart, K. Cui, M. Kupsta, E. Memarzadeh, D. Mitlin, "Silicon nanowire lithium-ion battery anodes with ALD deposited TiN coatings demonstrate a major improvement in cycling performance", *J. Mater. Chem. A* **1** 12850-12861 (2013)

12. E. Memarzadeh Lotfabad, P. Kalisvaart, K. Cui, A. Kohandehghan, M. Kupsta, B. Olsen, D. Mitlin, "ALD TiO_2 coated silicon nanowires for lithium ion battery anodes with enhanced cycling stability and coulombic efficiency", *Phys. Chem. Chem. Phys* **15** 13646-13657 (2013)

13. J. Rong, X. Fang, M. Ge, H. Chen, J. Xu, C. Zhou, "Coaxial Si/anodic titanium oxide/Si nanotube arrays for lithium-ion battery anodes", *Nano Res.* **6** 182-190 (2013)

14. S. Sim, P. Oh, S. Park, J. Cho, "Critical Thickness of SiO_2 Coating Layer on Core@Shell Bulk@Nanowire Si Anode Materials for Li-Ion Batteries", *Adv. Mater.* **25** 4498-4503 (2013)

15. H. Yoo, J.-I. Lee, H. Kim, J.-P. Lee, J. Cho, S. Park, "Helical Silicon/Silicon Oxide Core–Shell Anodes Grown onto the Surface of Bulk Silicon", *Nano Lett.* **11** 4324-4328 (2011)

16. Z. Y. Zeng, J. P. Tu, X. H. Huang, X. L. Wang, X. B. Zhao, K. F. Li, "Electrochemical Properties of a Mesoporous Si/TiO_2 Nanocomposite Film Anode for Lithium-Ion Batteries", *Electrochem. Solid-State Lett.* **11** A105-A107 (2008)

17. M. T. McDowell, S. W. Lee, I. Ryu, H. Wu, W. D. Nix, J. W. Choi, Y. Cui, "Novel Size and Surface Oxide Effects in Silicon Nanowires as Lithium Battery Anodes", *Nano Lett.* **11** 4018-4025 (2011)

18. B. M. Bang, H. Kim, H.-K. Song, J. Cho, S. Park, "Scalable approach to multi-dimensional bulk Si anodes via metal-assisted chemical etching", *Energy Environ. Sci.* **4** 5013-5019 (2011)

19. G. Jeong, J.-H. Kim, Y.-U. Kim, Y.-J. Kim, "Multifunctional TiO2 coating for a SiO anode in Li-ion batteries", *J. Mater. Chem.* **22** 7999-8004 (2012)

20. H. Yang, S. Huang, X. Huang, F. Fan, W. Liang, X. H. Liu, L.-Q. Chen, J. Y. Huang, J. Li, T. Zhu, S. Zhang, "Orientation-Dependent Interfacial Mobility Governs the Anisotropic Swelling in Lithiated Silicon Nanowires", *Nano Lett.* **12** 1953-1958 (2012)

21. C.-M. Wang, X. Li, Z. Wang, W. Xu, J. Liu, F. Gao, L. Kovarik, J.-G. Zhang, J. Howe, D. J. Burton, Z. Liu, X. Xiao, S. Thevuthasan, D. R. Baer, "In Situ TEM Investigation of Congruent Phase Transition and Structural Evolution of Nanostructured Silicon/Carbon Anode for Lithium Ion Batteries", *Nano Lett.* **12** 1624-1632 (2012)

22. J. W. Wang, X. H. Liu, K. Zhao, A. Palmer, E. Patten, D. Burton, S. X. Mao, Z. Suo, J. Y. Huang, "Sandwich-Lithiation and Longitudinal Crack in Amorphous Silicon Coated on Carbon Nanofibers", *ACS Nano* **6** 9158-9167 (2012)

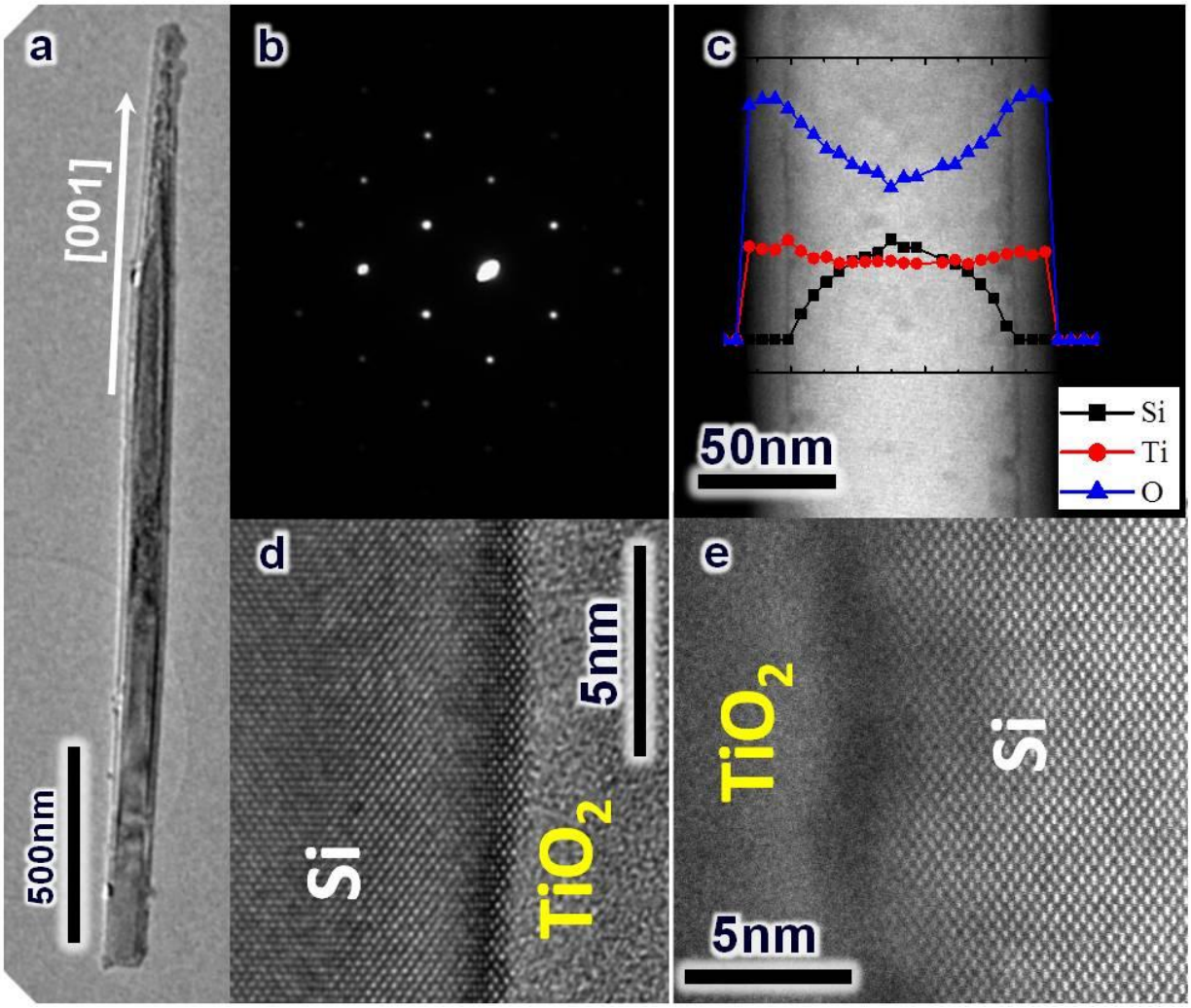

Figure 6.1 a. TEM micrograph of a single TiO_2-coated NW, and **b.** SAED of a Si core showing [001] growth orientation, **c, d, and e.** Both EELS line scan as well as high-resolution BF TEM and DF STEM images of a Si/TiO_2 interface illustrate the uniform shell thickness of TiO_2 around a Si NW.

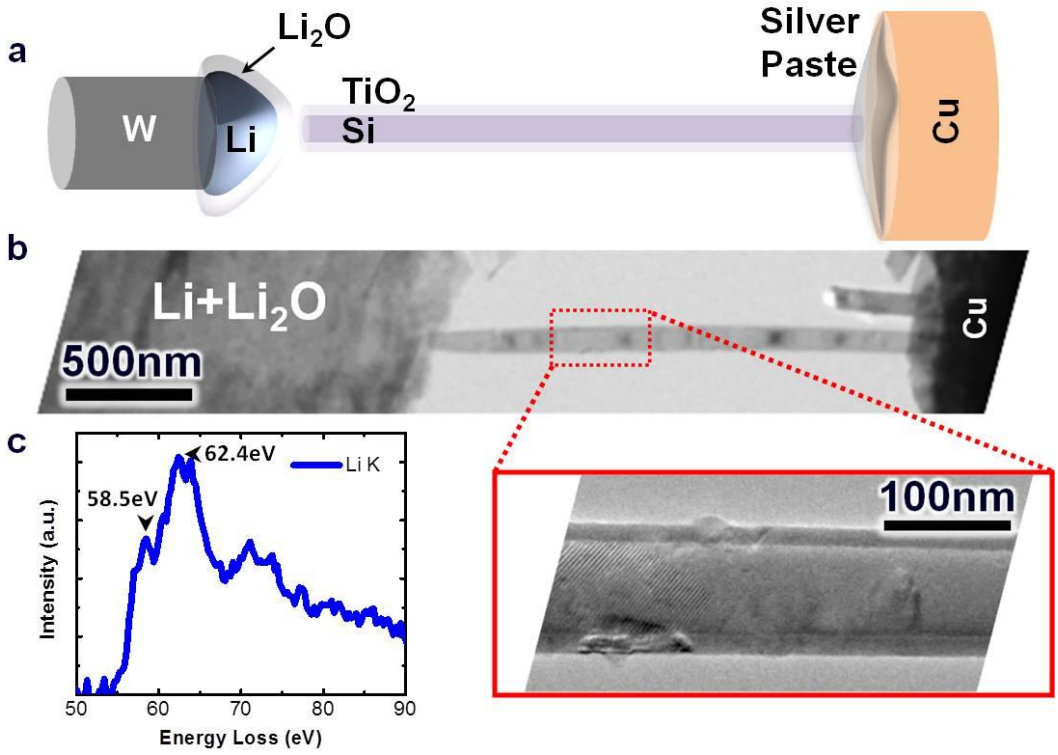

Figure 6.2 a. Schematic illustration of electrochemical set-up built inside TEM, **b.** TEM Image of the set-up, **c.** EELS Spectrum of a characteristic Li K peak from a Li_2O layer grown on Li metal.

se

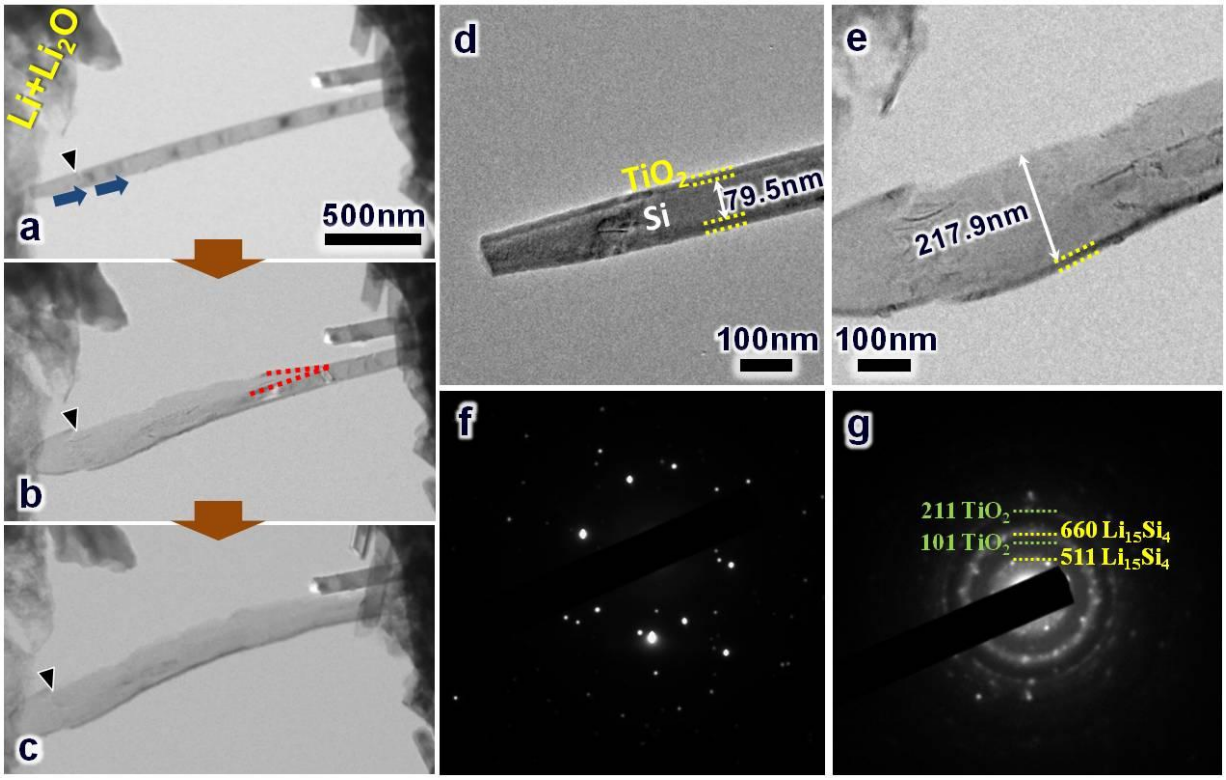

Figure 6.3 a, b, and c. Sequential TEM images illustrating different stages of lithiation inside a Si NW core, generating a fracture of TiO_2 shell, **d and e.** TEM images of a TiO_2-coated NW before and after lithiation, respectively and **f and g.** corresponding SAED of the these two stages.

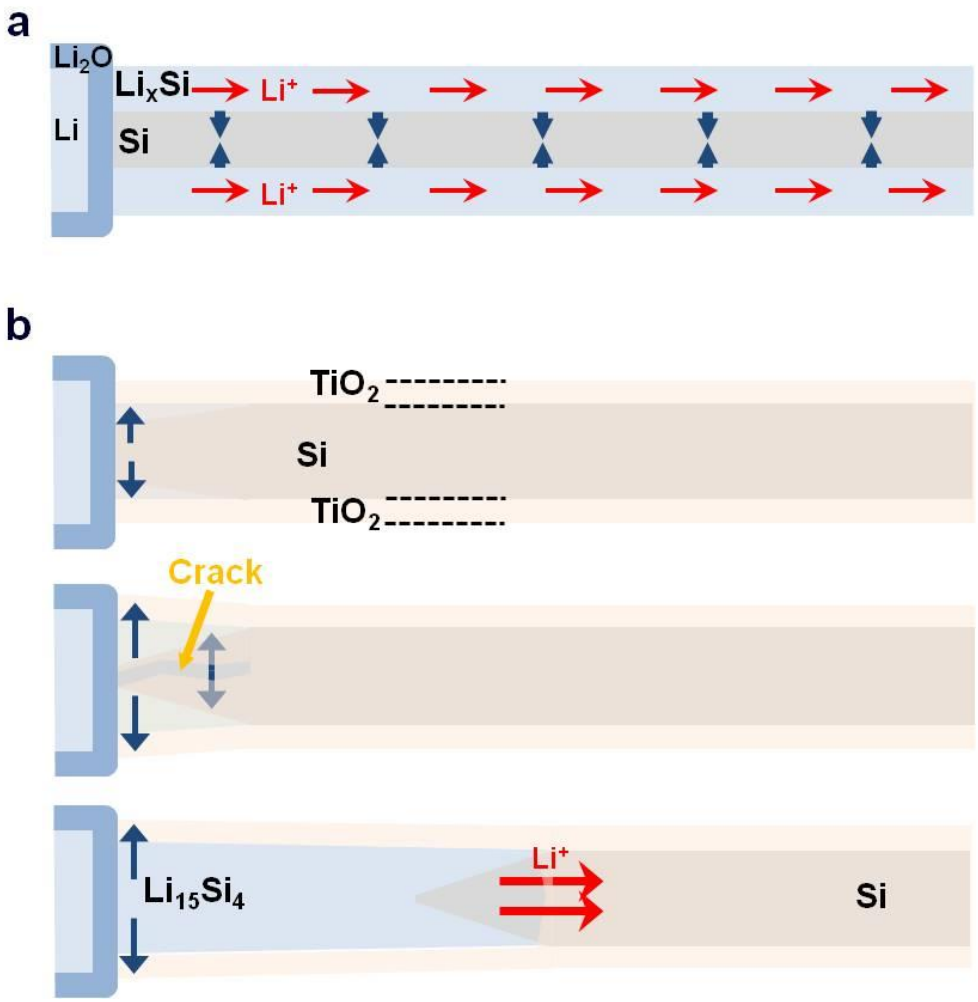

Figure 6.4 Schematics of lithium ion insertion **a.** into a primitive p-Si NW and **b.** into a TiO_2-coated p-Si NW.

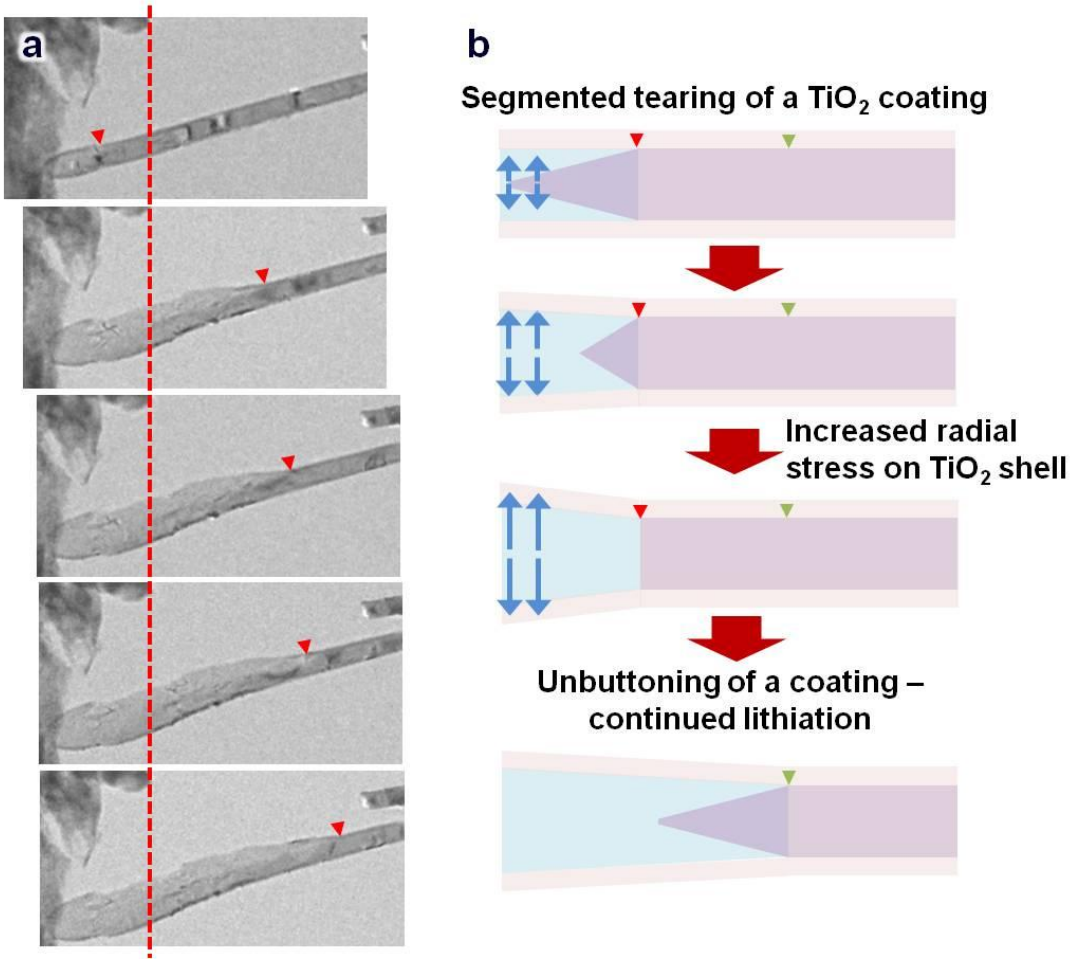

Figure 6.5 a. Sequence of TEM imaging of a TiO_2-coated Si NW at various stages of lithiation and **b.** a schematic of segmented tearing of TiO_2 coating.

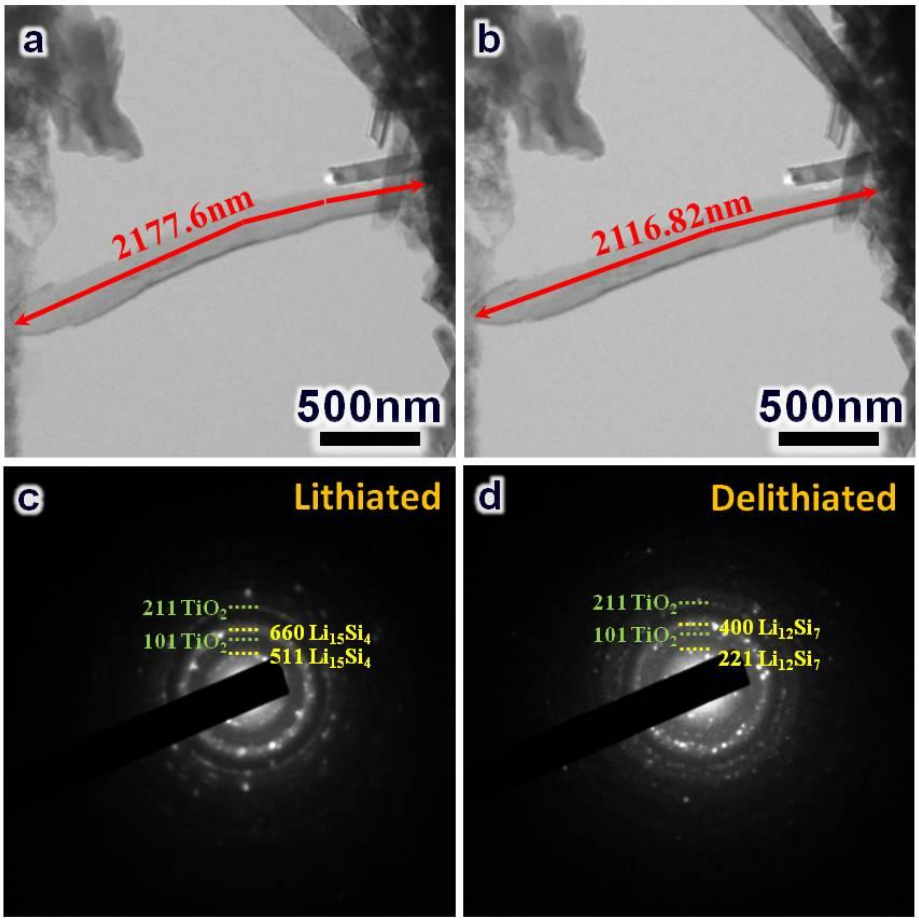

Figure 6.6 TEM images of a lithiated TiO_2-coated NW **a.** before and **b.** after delithiation and **c and d.** corresponding SAED of the these two stages.

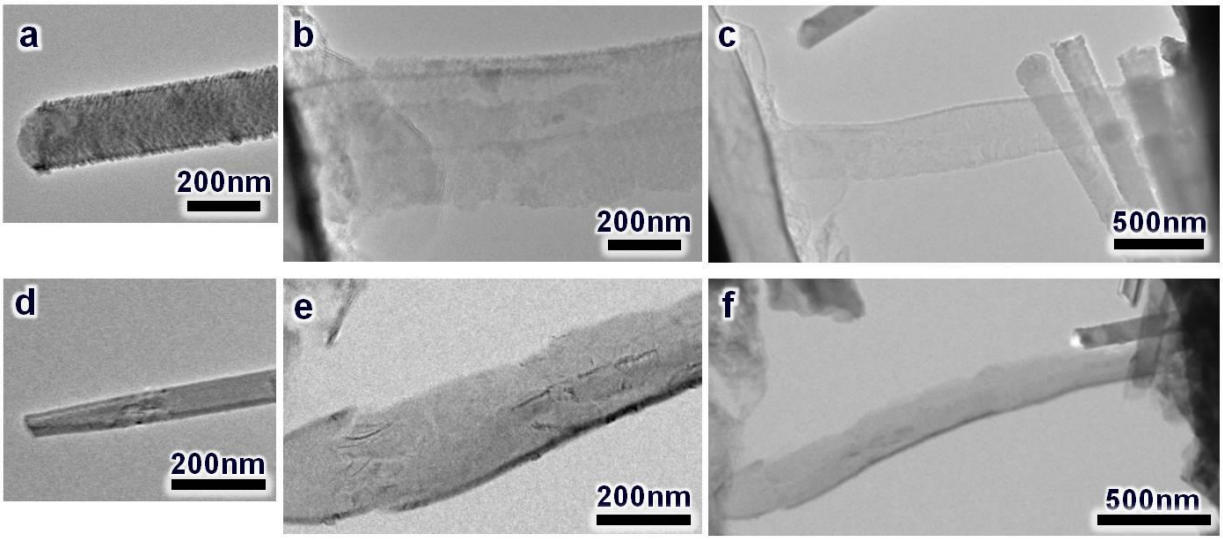

Figure 6.7 TEM micrographs of a Si NW with the core diameter-to-coating thickness ratio of 12:1 and 4.4:1, respectively, **a and d.** before and **b and e.** after lithiation. **c and f.** Lower magnification images showing the entire NWs.

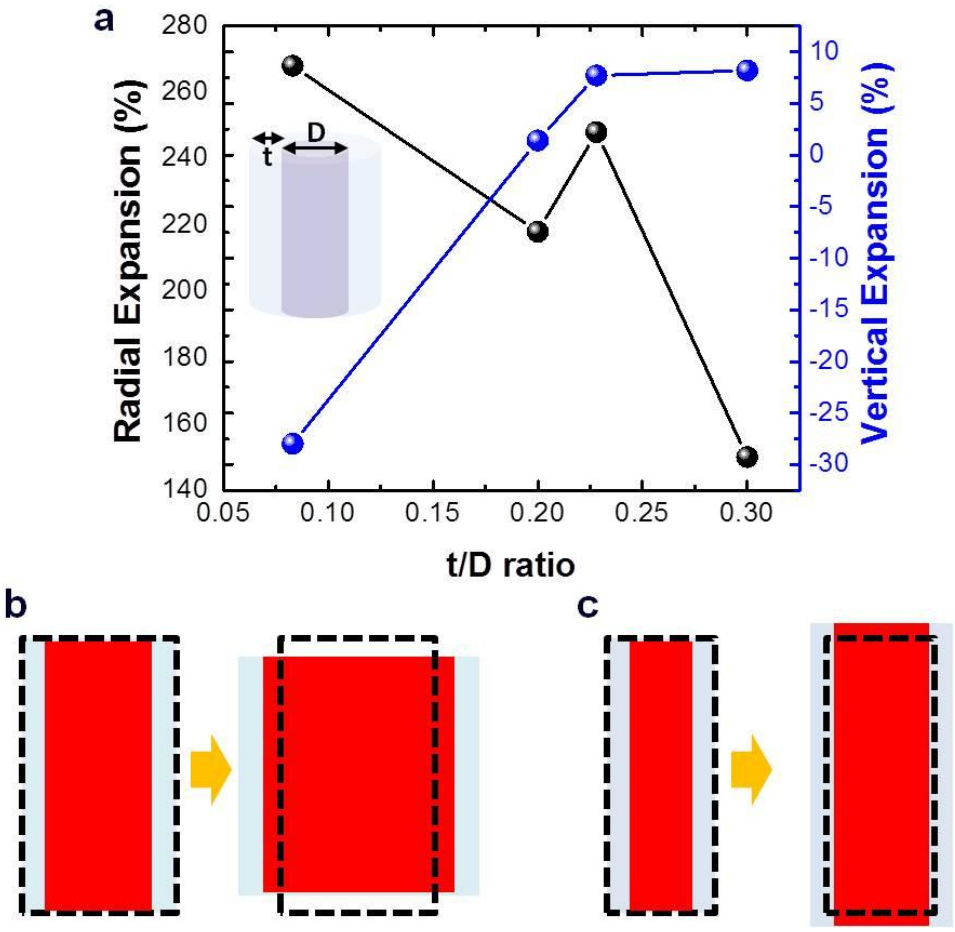

Figure 6.8 a. A graph showing the radial expansion and vertical expansion of a silicon core (%) against the coating thickness-to-core diameter ratio. Summarized schematics showing the final lithiated morphology of coated Si NWs with **b.** low t/D ratio vs. c. high t/D ratio

Chapter 7. Summary and Future work

7.1. Summary

Overall, this thesis presented a detailed study of various TiO_2-related Li ion battery anode materials using a novel structural characterization technique - in-situ atomic resolution transmission electron microscopy - that offers real-time observation of structural changes associated with Li intercalation in unprecedented details. In addition, postmortem analytical electron microscopy (aberration-corrected scanning transmission electron microscopy) combined with theoretical calculations using density functional theory were employed to enrich understanding of the mechanisms for lithium migration and structural relaxation upon lithiation for the anodes, originally detected by in-situ transmission electron microscopy.

The atomic-resolution electrochemical study of a rutile TiO_2 nanowire clearly demonstrated the two-step phase transformations upon lithium intercalation. It was found that rutile TiO_2 turns into first a monoclinic structure upon reaching the intermediate lithiation stage (Li mole fraction $x\sim0.5$) and finally a rock-salt structure upon full lithiation $x\sim1$. The interesting aspect of lithiation of a rutile polymorph was its highly anisotropic nature of the phase transformations that induced a large asymmetric structural expansion when reaching the intermediate stage and

ultimately generated a bubble-like dilation at multiple regions along the nanowire upon full lithiation.

The second topic of the thesis was related to the electrochemical lithiation of a TiO_2-B thin film, which was successfully deposited as a thin film onto a conventional (100) $SrTiO_3$ substrate. In the process of growth optimization, a Ca-variant of a TiO_2-B structure (Ca:TiO_2-B) was identified and effectively used as a template for the growth of a high quality TiO_2-B film. Chapter 4 presented the comprehensive overview of interfaces and defects in TiO_2-B and Ca:TiO_2-B films deposited on (100) and (110) $SrTiO_3$ substrates. A later part of the chapter focused on identifying the interfacial relationship between TiO_2-B and Ca:TiO_2-B. Near the interface between the two, a large number of both periodic and non-periodic out-of-phase boundaries were generated due to the missing Ca-modified layer either at the topmost surface or in the middle of a Ca:TiO_2-B stack. Also interesting is the interfacial relationship of TiO_2-B with a secondary phase anatase TiO_2 grain that was not only grown directly from $SrTiO_3$ but also structurally transformed from a parent TiO_2-B structure. The latter was formed as a micro-grain that has a distinct epitaxial and orientation relationship with TiO_2-B.

The second part of the chapter discussed extensively many interesting defects in a lithiated TiO_2-B film grown on (100) $SrTiO_3$ induced by strain relaxation upon a volumetric change of the film. It was found that the shape of these features are dependent on a Li insertion pathway. Upon Li intercalation along *b*-axis, lithiated TiO_2-B underwent a phase transformation to a higher order symmetry anatase-type TiO_2 structure via single column shearing. A theoretical study using

density functional theory was performed to calculate phase stability and the strain energy of various lithiated TiO_2 polymorphs. Due to its striking structural similarity with Li_xTiO_2-B and low strain energy of formation, anatase-type Li_xTiO_2, or more specifically β-$LiTi_2O_4$, was found energetically favorable to be transformed from $LiTi_2O_4$-B, thus supporting the experimental finding. Upon Li intercalation along *c*-axis, lithiation that initiated from the topmost (001) plane of TiO_2-B had Li either migrate vertically straight down towards a Ca:TiO_2-B layer or diffuse laterally through a *b*-axis channel. This generated shears of varying depth from the top to a certain point across the film upon structural relaxation depending on the degree of a misfit strain within Li_xTiO_2-B.

A final work of this thesis involved in using rutile TiO_2 as an semi-inert coating around a Si nanowire and understanding its influence on Li insertion into Si. Conclusively, a uniform TiO_2 coating around a Si nanowire helped suppress a volumetric expansion and maintain structural integrity of a Si core. It also gave rise to segmented lithiation by having each small nanowire portion experiencing full lithiation (up to $Li_{15}Si_4$) before the portion expanded to let Li progress towards the next segment of Si by tearing TiO_2 coating. Hence, Li migration behavior of a coated nanowire was different from that of an uncoated one which had Li wet the surface of the nanowire prior to its radial inward migration. Hence, the lithiated Si nanowire, when coated, was expanded both vertically and radially while the uncoated or thinly coated nanowire was expanded radially but compressed vertically. This result agreed well with the results from literature using ex-situ transmission electron microscopy examination of a Si nanowire coated with a native SiO_x layer after a potentiostatic cycling test using a standardized electrochemical cell.[1]

7.2. Future work

Out of many future works, the first is to expand the scope of investigations on the lithiation mechanism towards many other TiO_2 polymorphs besides rutile and bronze. A good system for an in-situ study is anatase TiO_2, which is the most extensively studied anode system in literature due to its excellent chemical stability in a nanostructured form. It has been indirectly demonstrated that there is two-phase coexistence between the Li-poor anatase phase and the emerging orthorhombic β-phase ($Li_{0.5}TiO_2$) upon Li insertion up to the mole fraction of ~0.5.[2-5] By employing high-resolution transmission electron microscopy, the mechanism for nucleation and growth of the β-phase from the anatase nanostructure will be interesting to explore. So far only the preliminary study has been done using anatase nanotubes, as included in the appendix (see Appendix B). However, due to some difficulty in handling the polycrystalline nanotubes for in-situ microscopy, the future experiment will use more structurally robust single-crystalline nanowires instead.

A comparative study of lithiation in TiO_2 in various structural forms will be of extensive interest for investigation and especially useful for morphological optimization for the real battery application. For example, for the TiO_2-B thin film, it was found that Li intercalation is limited to certain orientations and generates misfit strain to be ultimately relaxed via shearing and phase transformation. However, TiO_2-B nanostructure, especially nanoparticles, are not likely to be influenced as much by the bulk strain as the surface strain due to the high surface-to-volume ratio. The influences of the surface strain from some facets like (110) and (001) surfaces on Li

intercalation process are of great interest since these surfaces are found to accommodate Li ion diffusion.[6] Li intercalation into these nanoparticles can be performed via in-situ high-resolution transmission electron microscopy by loading them on a highly conductive graphene sheet for enhanced Li ion transport.

Lastly, investigating TiO_2 polymorphs for a rechargeable Na ion battery application using in-situ transmission electron microscopy will be novel and interesting due to high abundance of Na on earth. The electrochemical testing of anatase TiO_2 using Na has been demonstrated in conjunction with in-situ X-ray diffraction and ex-situ electron microscopy to study the Na intercalation mechanism into anatase TiO_2. However, there are some disagreements on the reaction pathways, especially whether anatase TiO_2 undergoes entirely an insertion reaction[7], as in the case using Li, or a mixed conversion and insertion reaction[8]. Energy dispersive spectroscopy and selected area electron diffraction will be conducive to identifying Na migration pathways and structural changes of TiO_2 upon reactions with Na.

7.3. References

1. M. T. McDowell, S. W. Lee, I. Ryu, H. Wu, W. D. Nix, J. W. Choi, Y. Cui, "Novel Size and Surface Oxide Effects in Silicon Nanowires as Lithium Battery Anodes", *Nano Lett.* **11** 4018-4025 (2011)

2. A. A. Belak, Y. Wang, A. Van der Ven, "Kinetics of Anatase Electrodes: The Role of Ordering, Anisotropy, and Shape Memory Effects", *Chem. Mater.* **24** 2894-2898 (2012)

3. M. Wagemaker, G. J. Kearley, A. A. van Well, H. Mutka, F. M. Mulder, "Multiple Li Positions inside Oxygen Octahedra in Lithiated TiO_2 Anatase", *J. Am. Chem. Soc.* **125** 840-848 (2002)

4. M. Wagemaker, A. P. M. Kentgens, F. M. Mulder, "Equilibrium lithium transport between nanocrystalline phases in intercalated TiO_2 anatase", *Nature* **418** 397-399 (2002)

5. M. Wagemaker, R. van de Krol, A. P. M. Kentgens, A. A. van Well, F. M. Mulder, "Two Phase Morphology Limits Lithium Diffusion in TiO_2 (Anatase): A 7Li MAS NMR Study", *J. Am. Chem. Soc.* **123** 11454-11461 (2001)

6. Y. G. Andreev, P. M. Panchmatia, Z. Liu, S. C. Parker, M. S. Islam, P. G. Bruce, "The Shape of TiO2-B Nanoparticles", *J. Am. Chem. Soc.* **136** 6306-6312 (2014)

7. K.-T. Kim, G. Ali, K. Y. Chung, C. S. Yoon, H. Yashiro, Y.-K. Sun, J. Lu, K. Amine, S.-T. Myung, "Anatase Titania Nanorods as an Intercalation Anode Material for Rechargeable Sodium Batteries", *Nano Lett.* **14** 416-422 (2014)

8. L. Wu, D. Bresser, D. Buchholz, G. A. Giffin, C. R. Castro, A. Ochel, S. Passerini, "Unfolding the Mechanism of Sodium Insertion in Anatase TiO2 Nanoparticles", *Adv. Energy Mater.* **5** 1401142 (2015)

Appendix A Lithiation of a rutile TiO_2-coated Si NW using a liquid cell prototype inside TEM

A.1. Introduction and Background

As an extension to the study on lithiation of a Si nanowire (NW) coated with rutile TiO_2 using in-situ transmission electron microscopy (TEM) as demonstrated in chapter 6, a similar study on NWs but using a liquid cell prototype rather than a solid cell prototype for in-situ TEM was performed. The difference between the two prototypes comes from the choice of an electrolyte; a liquid cell prototype uses a low vapor pressure ionic liquid electrolyte (ILE) rather than amorphous Li_2O used in the solid cell.

Despite the convenience of its use for in-situ TEM, Li_2O is seldom used as an electrolyte in the conventional battery system because Li ion diffusivity is only about 10^{-10} cm^2s^{-1}.[1] Hence, it is more desirable to apply a liquid electrolyte that has a reasonably high Li ion diffusivity for effective cell operation. Along with the low vapor pressure, lithium bis(trifluoromethylsulfonyl) imide (LiTFSI) dissolved into 1-butyl-1-methylpyrrolidinium bis(trifluoromethylsulfonyl) imide (P_{14}TFSI) has a reasonable ionic diffusivity of around $10^{-6}cm^2s^{-1}$[2] and, thus, is a good liquid electrolyte candidate to be used for a cell assembled in TEM. Certainly, using a liquid electrolyte is anticipated to provide a better picture of electrochemical reactions between Li and the NW since they must resemble to that occurring in a standard electrochemical cell. Therefore, in this

work, using an ionic liquid electrolyte, electrochemical lithiation was performed on a TiO_2-coated Si NW inside TEM.

A.2. Experimental Procedures

A batch of ~30nm p-doped Si NWs was grown on a Si substrate by chemical vapor deposition (CVD). A uniform rutile TiO_2 coating was deposited onto a Si NW via atomic layer deposition (ALD) with a precise control over the layer thickness prior to be decorated with rutile TiO_2 nanotube (NT) powders.

A TEM specimen was prepared by embedding NWs in a Ag-based paste on a tungsten wire. A prepared specimen was loaded onto a piezo-drive of a single-tilt in-situ Nanofactory Instruments TEM-STM holder to be part as an anode of an electro-chemical cell assembly in a JEOL JEM-3010F microscope. Bulk Li metal, as a counter-part, was scrapped onto a copper rod and dipped into an ILE consist of P_{14}TFSI solution mixed with 10 wt% LITFSI to coat it on the surface of Li, prior to loading it on the other side of the holder. A piezo-movement of the W tip attached with NWs can be controlled with great precision within the holder, allowing it to be contacted with the liquid electrolyte, thus completing the assembly of an electro-chemical cell inside the TEM.

A.3. Results and Discussion

Figure A.1a illustrates the schematic of a liquid cell prototype used for testing a single TiO_2-coated Si NW inside TEM. In order to avoid the effect of an electron beam that readily reacts

with liquid electrolyte, a long NW with a length greater than 10 μm, as illustrated in Figure A.1b, was used for testing. Figure A.1c shows the NW after getting immersed into an ILE.

In this study, lithiation and delithiation of a TiO_2-coated Si NW were conducted under potentiostatic mode at room temperature. A bias of -3V with respect to Li metal for lithiation and 3V for lithium extraction were used; these voltage were set slightly larger than the ones used in literature[3] in order to expedite Li ion migration into the film. According to Figure A.2a, c, and e, upon lithiation and delithiation, the NW underwent a lateral expansion and contraction approximately by 140% and 90%, respectively. The axial changes, based on the measurement from the reference point (yellow lines in Figure A.2a, c, and e) to the contact with an ILE (red lines in Figure A.2a, c, and e) upon lithiation and delithiation were 120% and 97%, respectively. All measurements included both a Si core and a TiO_2 shell, and the degree of dimensional changes in a Si core alone was not considered because of difficulty in measurements especially upon delithiation as TiO_2 nanoparticles detached from a lithiated Si did not contract as much as a core.

SAED was simultaneously performed to observe the structural changes associated with the electrochemical cycle (Figure A.2b, d, and f). Indeed, the structural change of a Si core occurred from c-Si to c-$Li_{15}Si_4$, which in fact agreed with the result obtained using a solid cell prototype in Chapter 6. However, upon delithiation, the lithiated Si changed its structure from c-$Li_{15}Si_4$ to a-LiSi, indicating more extraction of Li ions happened than that using a solid cell. This is because of higher Li ion diffusivity of an ILE than that of a solid electrolyte. In order to extract Li entirely from Si, many in-situ TEM studies applied a carbon coating on a Si NW to improve ion transport back to its source upon delithiation.[4-5]

A TiO_2-coated Si NW demonstrated remarkable cyclability and structural integrity even after the second lithiation and delithiation as demonstrated in Figure A.3. Upon lithiation and delithiation, the NW underwent the lateral expansion and contraction by 159% and 76%. Interestingly, the degree of structural changes was slightly higher than that of the first cycle because lithiation and delithiation behaviors of Si during the second cycle are less influenced by the much weakened coating after the first cycle. The observation suggests both the advantage and disadvantage of having a TiO_2 coating around Si. While the uniform coating effectively suppresses the Si core from expanding upon lithiation, it can also block Li from being extracted from Si when it gets delithiated. Nevertheless, high fluidity of an ILE was conducive to NW cyclability as it helped Li migration in and out of the NW.

After the second round of lithiation, there were notable signs of degradation observed throughout the NW. Although having double TiO_2 layers (ALD TiO_2 and TiO_2 NTs) surrounding Si made the coating more robust, the weak bonding among different grains induced uneven expansion of the NW as shown in Figure A.4a. This could potentially disintegrate the NW as the local stress built up inside the NW due to the difference in Li ion kinetics among different regions along the NW. In addition, some parts of a TiO_2 coating were detached from a Si NW as it expanded and was unable to hold its coating epitaxally (Figure A.4b). Finally, some TiO_2 NTs decorated around a ALD TiO_2 coating disappeared (Figure A.4c) possibly due to the weak bonding with an inner coating. The degradation of a coating affected the delithiation behavior of the coated NW. Li, instead of being extracted through the channels inside Si towards the NW-liquid electrolyte interface, migrated out laterally through the intraparticle gaps of the damaged TiO_2 coating. Figure A.5a illustrates the weak image contrasts sporadically emerged from a TiO_2 coating. These contrasts can be attributed to Li that migrated out of Si as the NW shrinked radially upon

delithiation. This finding suggests the possibility of fast extraction of Li through the sides, which would otherwise have been impossible if the coating remained completely intact. In context to the conventional Li ion battery where the NW anode is completely immersed in the liquid electrolyte, this further implies that the amount and speed of Li extraction and transport through the electrolyte should be improved and contribute to an increase in charge/discharge rate capability. (see Figure A.5b) Hence, by optimizing the design of a coating around Si, the NW can potentially maintain its structural integrity upon lithiation while providing expedite inlets and outlets for Li during charge and discharge.

A.4. Conclusions

In summary, the electrochemical lithiation and delithiation of a rutile TiO_2-coated Si NW were performed using a liquid cell prototype inside TEM. Upon multiple lithiation and delithiation cycles, the Si core maintained its good cyclability and structural integrity despite the degradation of the TiO_2 coating. A more careful design of a TiO_2 coating around Si would not only restrain Si from large volumetric expansion upon Li insertion but also provide multiple routes for efficient Li extraction prior to being carried out by a liquid elctrolyte.

A.5. References

1. X. H. Liu, J. Y. Huang, "In situ TEM electrochemistry of anode materials in lithium ion batteries", *Energy Environ. Sci.* **4** 3844-3860 (2011)

2. T. Nishida, K. Nishikawa, Y. Fukunaka, "Diffusivity Measurement of $LiPF_6$, LiTFSI, $LiBF_4$ in PC", *ECS Trans.* **6** 1-14 (2008)

3. X. H. Liu, H. Zheng, L. Zhong, S. Huang, K. Karki, L. Q. Zhang, Y. Liu, A. Kushima, W. T. Liang, J. W. Wang, J.-H. Cho, E. Epstein, S. A. Dayeh, S. T. Picraux, T. Zhu, J. Li, J. P. Sullivan, J. Cumings, C. Wang, S. X. Mao, Z. Z. Ye, S. Zhang, J. Y. Huang, "Anisotropic Swelling and Fracture of Silicon Nanowires during Lithiation", *Nano Lett.* **11** 3312-3318 (2011)

4. J. W. Wang, X. H. Liu, K. Zhao, A. Palmer, E. Patten, D. Burton, S. X. Mao, Z. Suo, J. Y. Huang, "Sandwich-Lithiation and Longitudinal Crack in Amorphous Silicon Coated on Carbon Nanofibers", *ACS Nano* **6** 9158-9167 (2012)

5. C.-M. Wang, X. Li, Z. Wang, W. Xu, J. Liu, F. Gao, L. Kovarik, J.-G. Zhang, J. Howe, D. J. Burton, Z. Liu, X. Xiao, S. Thevuthasan, D. R. Baer, "In Situ TEM Investigation of Congruent Phase Transition and Structural Evolution of Nanostructured Silicon/Carbon Anode for Lithium Ion Batteries", *Nano Lett.* **12** 1624-1632 (2012)

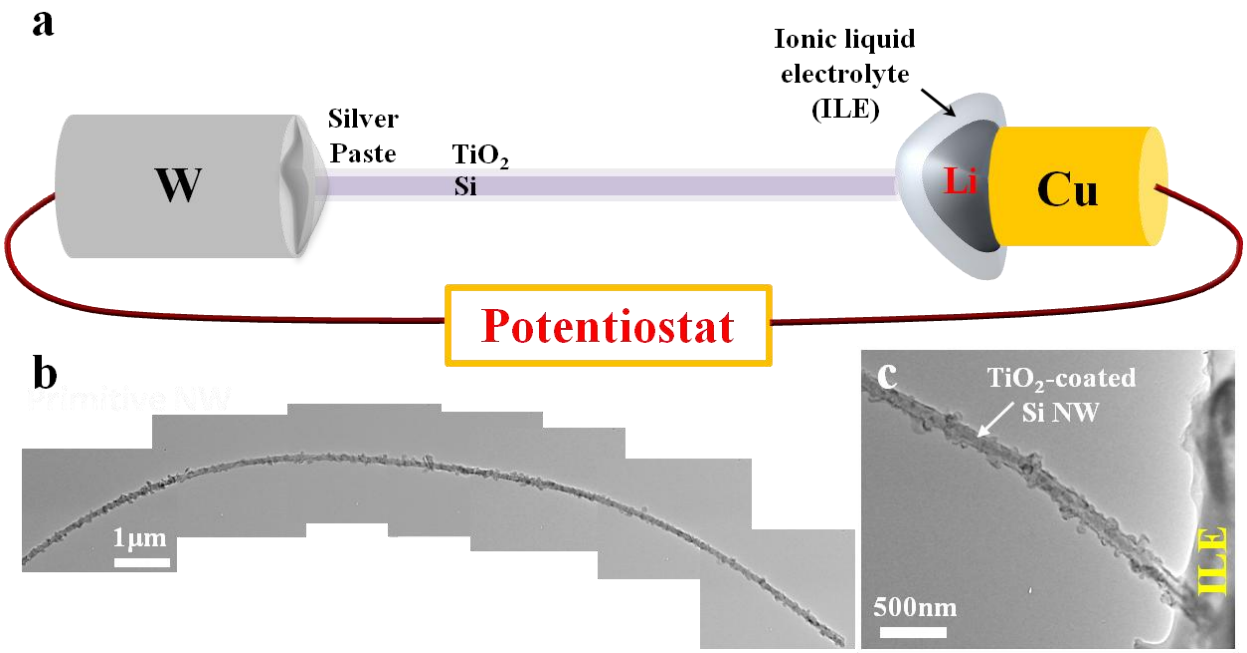

Figure A.1 a. A schematic illustration of an electrochemical set-up built inside TEM, **b.** Low-magnification TEM image of a primitive rutile TiO_2-coated Si NW, and **c.** TEM image of a NW contacted with an ILE.

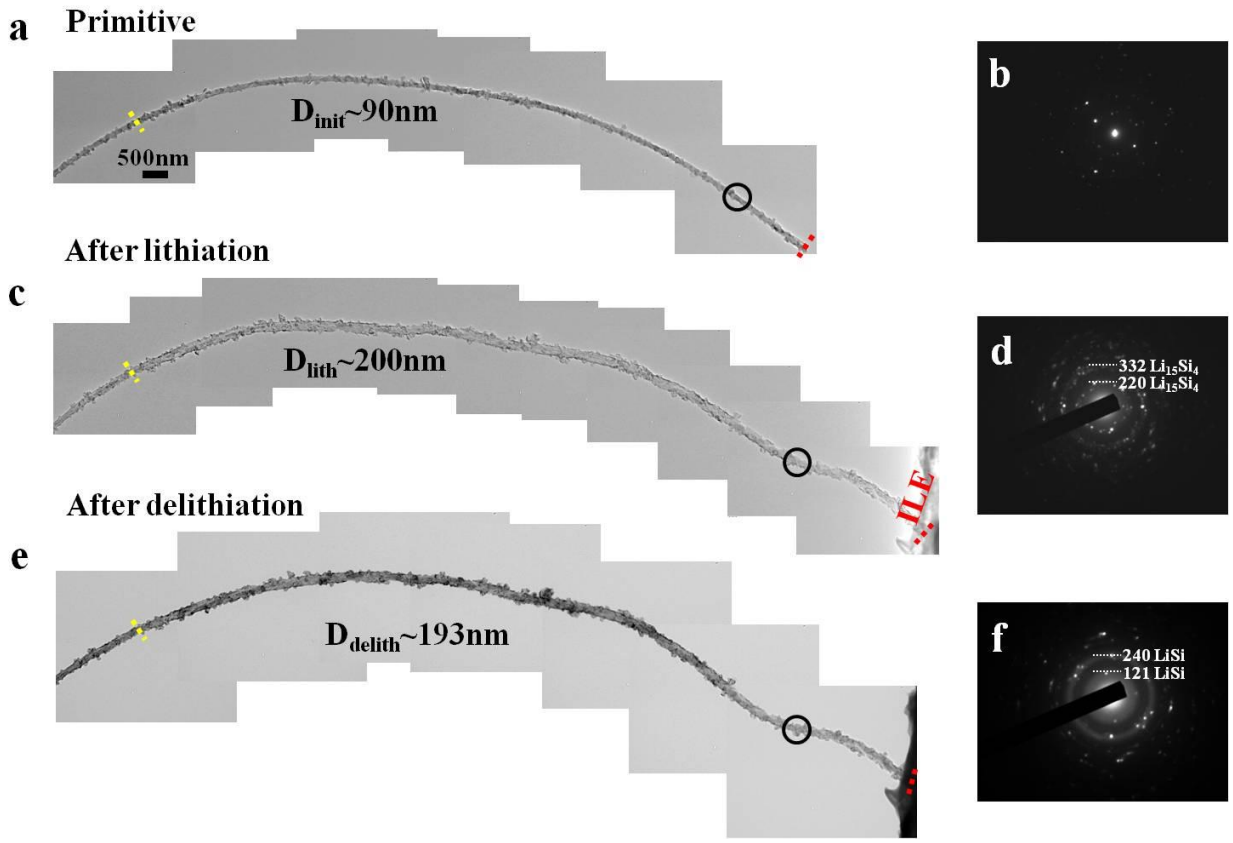

Figure A.2 Low-magnification TEM images of a TiO_2-coated Si NW **a.** before, **c.** after lithiation, and **e.** after delithiation, and **b, d, and f.** Corresponding SAED patterns taken from the areas within the NWs (circles), respectively. D is the maximum diameter of the NW at different stages.

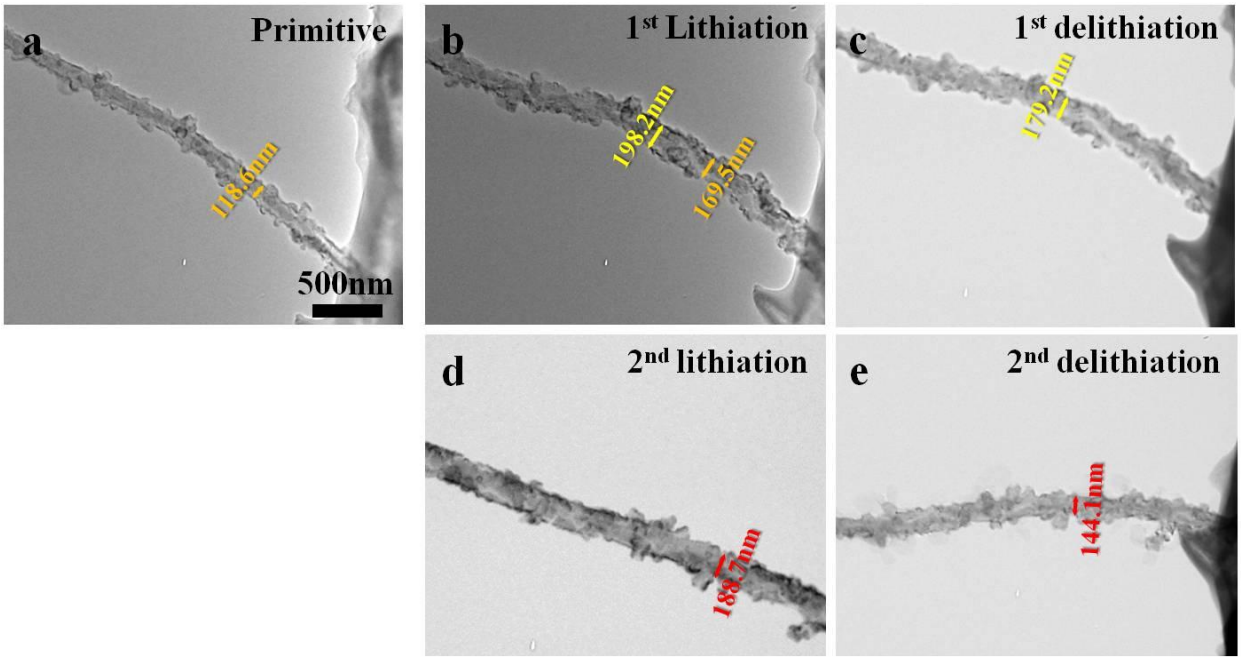

Figure A.3 TEM Images demonstrating various stages of lithiation and delithiation of a TiO_2-coated Si NW; **a.** primitive, **b and c.** after 1st lithiation and delithiation, and **d and e.** after 2nd lithiation and delithiation. Measurements at different stages marked with a same color mean that the they were taken at the same location within the NW.

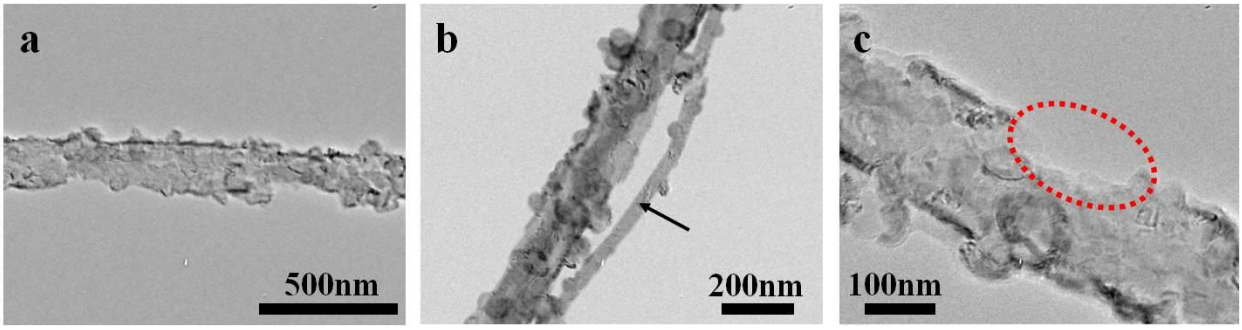

Figure A.4 TEM Images that demonstrate the aftermath of NW lithiation. **a.** Non-uniform expansion of Si, **b.** detachment of a TiO_2 coating, and **c.** missing TiO_2 nanoparticles.

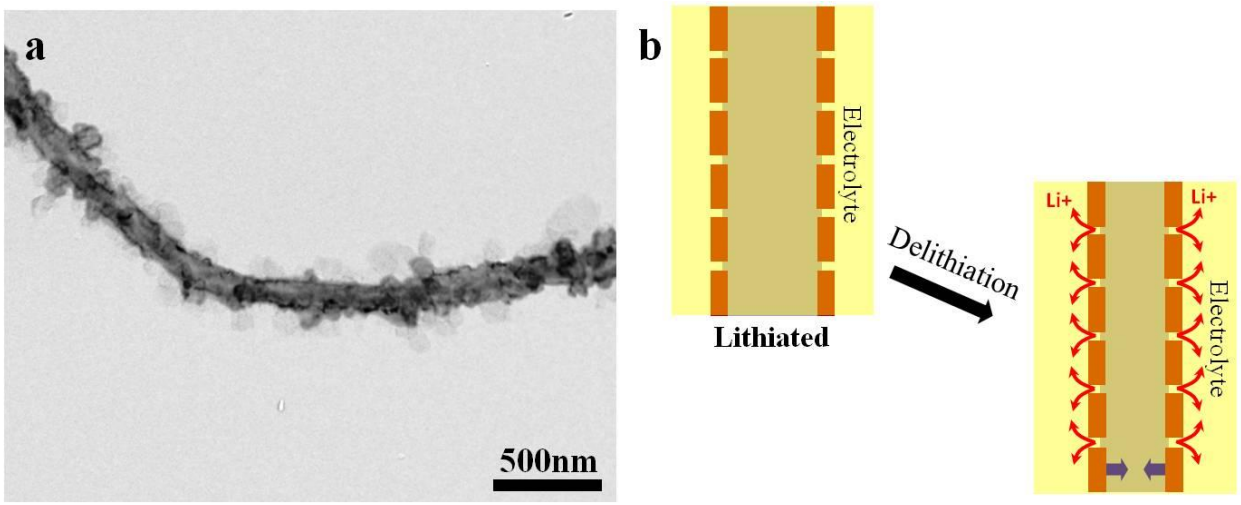

Figure A.5 a. TEM image of a NW undergoing delithiation. Li ions were being extracted from the TiO_2 side wall through the intraparticle gaps. **b.** This would lead to fast extraction of Li ions through the side for the case of a conventional cell where the entire NW is immersed in the liquid electrolyte.

Appendix B Structural Characterization of nanostructured anatase TiO_2 upon electrochemical lithiation

B.1. Introduction and Background

Another TiO_2 polymorph, besides rutile and bronze, that will be interesting to discuss in this thesis is the anatase polymorph of TiO_2. It is one of the most studied intercalation anode materials for a Li ion battery for its reversible Li ion storage capability. Along with its excellent chemical stability in smaller dimensions, nanostructured anatase TiO_2 has not only overcome the disadvantages of the bulk (i.e. poor ionic and electrical conductivity) but also enhanced the electrochemical energy storage properties. According to Wagemaker and co-workers, anatase TiO_2 nanostructure experiences immediate phase separation into a Li-poor α phase ($Li_{0.05}TiO_2$) and a Li-rich β phase ($Li_{0.5}TiO_2$) upon Li insertion.[1-3] Despite the two phases being indirectly identified both in in-situ X-ray diffraction and ex-situ nuclear magnetic resonance, the distinct boundary nucleation and growth upon phase separation between the two phases are more to be explored. The theoretical study done by Van der Ven, et al., using density functional theory suggests this boundary lies along the strain invariant plane. According to their calculation, Li diffusion parallel to the boundary makes the growth of the Li-rich phase self-limited since it is only ensued by Li insertion into the Li-poor phase. Thus, this promotes the

growth of a Li-rich phase "shell" around the Li-poor phase and possibly leads to the performance degradation of an electrode.

In this work, a direct probing of the two-phase reaction in anatase TiO_2 nanostructures was attempted for the first time using in-situ transmission electron microscopy (TEM). For a preliminary study, polycrystalline anatase TiO_2 nanotubes (NTs) were selected as a test anode material. In conjunction with an in-situ study, post-mortem scanning TEM (STEM) was performed on electrochemically cycled NWs using a standard Li ion cell to identify structural changes that could be indicative of phase separation in anatase TiO_2 NTs.

B.2. Experimental Procedures

TiO_2 nanotube arrays were prepared by an anodization process in a two-electrode electrochemical bath. The working electrode, Ti foil (99.5% purity, 0.25 mm thick, Alfa Aesar) was cleaned in a mild detergent, rinsed with DI water and ultra-sonicated in acetone and ethanol for 5 minutes in each solvent. Then, the Ti foil was immersed in 1:18:81 it for another 5 minutes. After cleaned, it was dried by a N_2 blow. A platinum foil was used as the counter electrode. The voltage was applied by a DC power supply (Agilent, E3612A). A thin TiO_2 nanotube array layer was produced by anodizing the Ti foil in a solution of ethylene glycol (99.8%, JT Baker) containing 0.30% ammonium fluoride (NH4F, 96%, Alfa Aesar) and 5% H_2O at 60 V for 3.5 hours. The procedures for TEM sample preparation and an in-situ TEM set-up for TiO_2 NTs are similar to that described in Chapter 3 of the thesis.

Li ion half-cells (EL-CELL ECC-STD) were assembled inside an argon-filled glove box (Innovative Technology Inert Lab) with both O_2 and H_2O levels below 2 ppm and tested on a 4-

channel system (Princeton Applied Research VersaSTAT MC) using Li metal, non-aqueous electrolyte (1M LiPF6 in ethylene carbonate : dimethyl carbonate 1:1 (v/v), Merck), a 1.55-mm-thick glass fiber separator, and a TiO_2 NT film deposited on a electrically conductive Ti foil. The post-mortem imaging was performed using high-resolution STEM.

B.3. Preliminary Findings

Cyclic voltammetry on a TiO_2 NT film performed at 0.1mV/s clearly revealed the distinct peaks both during reduction and oxidation. These peaks were shown approximately at 1.7 eV and 2.1 eV and are possibly indicative of the co-existence of the two phases, Li-poor TiO_2 and $Li_{0.5}TiO_2$. Other small peaks were also identified approximately at 1.4 eV and 1.65 eV, respectively, upon reduction and oxidation, and they are possibly biphasic peaks of two phases, $Li_{0.5}TiO_2$ and $LiTiO_2$. (Figure B.1) However, the above measurement only shows two-phase coexistence not phase separation. The possibility of the two phase separation was hinted when performing a galvanostatic electrochemical measurement on TiO_2 NTs. As shown in Figure B.2a, upon reaching a biphasic plateau around 2.0 V, a tentative "overshoot" of an potential was observed. When projecting this qualitatively into the Gibbs free energy diagram like in Figure B.2b, this bump corresponds to a sudden change in the slope of a free energy curve since the potential (V) is the mole fraction derivative of Gibbs free energy. Interestingly, this overpotential happened regardless of the Li discharge rate of the cell, and this means that Li ion diffusion into a Li_xTiO_2 lattice proceeded slowly to overcome the energy barrier of formation of β-$Li_{0.5}TiO_2$. (Figure B.2b) However, by eventually overcoming the barrier, Li_xTiO_2 could finally reach the biphasic state between β-$Li_{0.5}TiO_2$ and Li-poor Li_xTiO_2. (Figure B.2c)

An ex-situ STEM examination performed on after-cycled anatase TiO_2 NTs revealed intriguing structural changes occurred after 200 cycles (charge/discharge rate range of 0.5~1C). Figure B.3a and b show the high-resolution STEM of the cross-section of one of NTs before and after cycling. In contrast to the as-grown NT that has small, randomly shaped nano-pores naturally formed upon growth, the after-cycled NT has much uniformly dispersed large nano-pores that are distinct in shapes and orientations. There is also a clear increase in the depth of these voids as demonstrated in the comparative phase maps calculated from the fast-Fourier transformation (FFT) patterns of TEM images via geometric phase analysis before and after the electrochemical cycles.[4-5] (Figure B.3d and f) The density of these voids is neglected in this study since the number of voids in each NT varies from one to the other. The nano-pores in the after-cycled NTs are rectangular-shaped with sharp edges top and bottom and diffuse edges left and right. Based on STEM imaging performed along a [011] zone axis, the sharp and diffused edges correspond to {011} and {100} planes respectively. Interestingly, the sharp edges lie parallel to the *a*-axis, which happens to be the most favorable direction for Li ion migration.

The origin of this feature can be understood in context to previous works that have been done on Li ion migration in anatase TiO_2. According to Wagemaker et al., Li ions travel through the energetically favorable octahedral sites in Li_xTiO_2 that are located zigzag along a-direction. At x=0.5, Li_xTiO_2 undergoes instant phase transformation from a tetragonal (α) to an orthorhombic (β) structure.[3] However, based on in-situ X-ray diffraction, they later concluded that the mechanism for phase transition in anatase TiO_2 is size-dependent; smaller nanostructures ranged from ~15nm to ~40nm only exist or nucleate as single domains, either α or β-phase, without having any phase boundaries, while larger nanostructures (>130nm) have two phases co-existing with a distinct phase boundary within each single crystallite.[6] This difference is due to the fast

initial phase boundary movement that instantly affects both domain sizes and their solubility limits of the two phases. According to Van der Ven, et al., this instant movement is theoretically possible in anatase TiO_2 because it is interfacially controlled and not diffusion-controlled by Li ions.[7] The growth of α and β phases is most likely induced by the diffusion-less martensitic transformation that has the strain-free habit plane in *b*-*c* axis and not by slow Li ion diffusion into Li_xTiO_2. However, as lithium ions migrate, several variants of a β phase grow larger and start impinging upon each other. This not only induces a loss of lattice coherency at α-β interfaces perpendicular to the habit plane but also generates a head-to-head stress between the two impinged β phases to generate defects and, if worse, cracks.

Based on these studies, a parallel correlation can be done with our STEM results. First, our NTs are larger than 130nm on average and most likely undergo two phase coexistence between α and β phases. Hence, the two parallel sharp edges in large nano-pores are most likely the traces of phase separation between α and β phases upon Li insertion. The nano-pores were most likely formed due to a loss of strain coherency between α and β phases as the boundary expanded via constant Li insertion. The question that still remains, however, is whether these distinctly shaped nano-pores were expanded from the original nano-pores of an as-grown NT or newly nucleated within the NT upon Li insertion. To answer this question, the electrochemical lithiation of an anatase NT was attempted inside TEM to directly observe phase transformation.

To observe the phase transition occurring in an anatase TiO_2, lithiation of a NT was conducted under potentiostatic mode at room temperature under illumination of a low-dose electron beam. Upon constant Li insertion of a TiO_2 NT bundle under -4V bias, the Moirés fringes emerged at different regions throughout a NT (Figure B.4). This implies that there is presence of a new phase in addition to the original phase and might already suggest the possible two phase co-

existence. Unfortunately, the orientation and epitaxial relationship of a new phase relative to the original could not be identified during the lithiation due to the difficulty of performing high-resolution TEM and selected area electron diffraction (SAED) on a polycrystalline nanostructure. Nevertheless, upon continuous lithiation up to lithium mole fraction almost equivalent to 1, the NT underwent full phase transformation from anatase to β-$Li_{0.5}TiO_2$ as clearly demonstrated from SAED (Figure B.5). Polycrystalline Li_2O was also detected in the diffraction pattern and could have been derived from solid-electrolyte interphase formation between a TiO_2 NT and Li at the surface of a NT. After phase transformation, the NW structure disintegrated completely. The tearing of a NT was again possibly driven by two phase separation during lithiation. The randomness in structural disintegration was probably due to the polycrystallinity of anatase TiO_2 that has randomly oriented grains (Figure B.5). It is interesting to note that the fracture generation upon loss of coherency was observed in a similar manner in another biphasic Li insertion material, $LiFePO_4$, although the phase boundary migration in $LiFePO_4$ is driven purely by Li ion diffusion and not by an interfacial phenomenon.[8-9]

B.4. Conclusions and Future Work

In summary, the electrochemical lithiation was attempted for the first time on a polycrystalline anatase TiO_2 NT inside TEM to observe in real-time two phase separation between a Li-poor α phase and a Li-rich β phase. Although the structural disintegration of an anatase TiO_2 upon full lithiation is suggestive of phase separation, high-resolution TEM characterization is necessary to obtain the clearer picture on the phenomenon. Unfortunately, the polycrystalline NT form of anatase TiO_2 made the in-situ experiment difficult since the NWs were too fragile to load individually onto the sample post. A much simpler system like a solid, single-crystalline anatase

TiO_2 will be a good material system for in-situ TEM study. Single crystallinity of a NW not only promotes Li insertion but also enables clear visualization of the Li intercalation phenomenon.

B.5. References

1. M. Wagemaker, A. P. M. Kentgens, F. M. Mulder, "Equilibrium lithium transport between nanocrystalline phases in intercalated TiO_2 anatase", *Nature* **418** 397-399 (2002)

2. M. Wagemaker, R. van de Krol, A. P. M. Kentgens, A. A. van Well, F. M. Mulder, "Two Phase Morphology Limits Lithium Diffusion in TiO_2 (Anatase): A 7Li MAS NMR Study", *J. Am. Chem. Soc.* **123** 11454-11461 (2001)

3. M. Wagemaker, G. J. Kearley, A. A. van Well, H. Mutka, F. M. Mulder, "Multiple Li Positions inside Oxygen Octahedra in Lithiated TiO_2 Anatase", *J. Am. Chem. Soc.* **125** 840-848 (2003)

4. M. J. Hÿtch, E. Snoeck, R. Kilaas, "Quantitative measurement of displacement and strain fields from HREM micrographs", *Ultramicroscopy* **74** 131-146 (1998)

5. The software used for geometric phase analysis was developed by Christoph Koch.

6. K. Shen, H. Chen, F. Klaver, F. M. Mulder, M. Wagemaker, "Impact of Particle Size on the Non-Equilibrium Phase Transition of Lithium-Inserted Anatase TiO_2", *Chem. Mater.* **26** 1608-1615 (2014)

7. A. A. Belak, Y. Wang, A. Van der Ven, "Kinetics of Anatase Electrodes: The Role of Ordering, Anisotropy, and Shape Memory Effects", *Chem. Mater.* **24** 2894-2898 (2012)

8. C. V. Ramana, A. Mauger, F. Gendron, C. M. Julien, K. Zaghib, "Study of the Li-insertion/extraction process in $LiFePO_4/FePO_4$", *J. Power Sources* **187** 555-564 (2009)

9. G. Chen, X. Song, T. J. Richardson, "Electron Microscopy Study of the $LiFePO_4$ to $FePO_4$ Phase Transition", *Electrochem. Solid-State Lett.* **9** A295-A298 (2006)

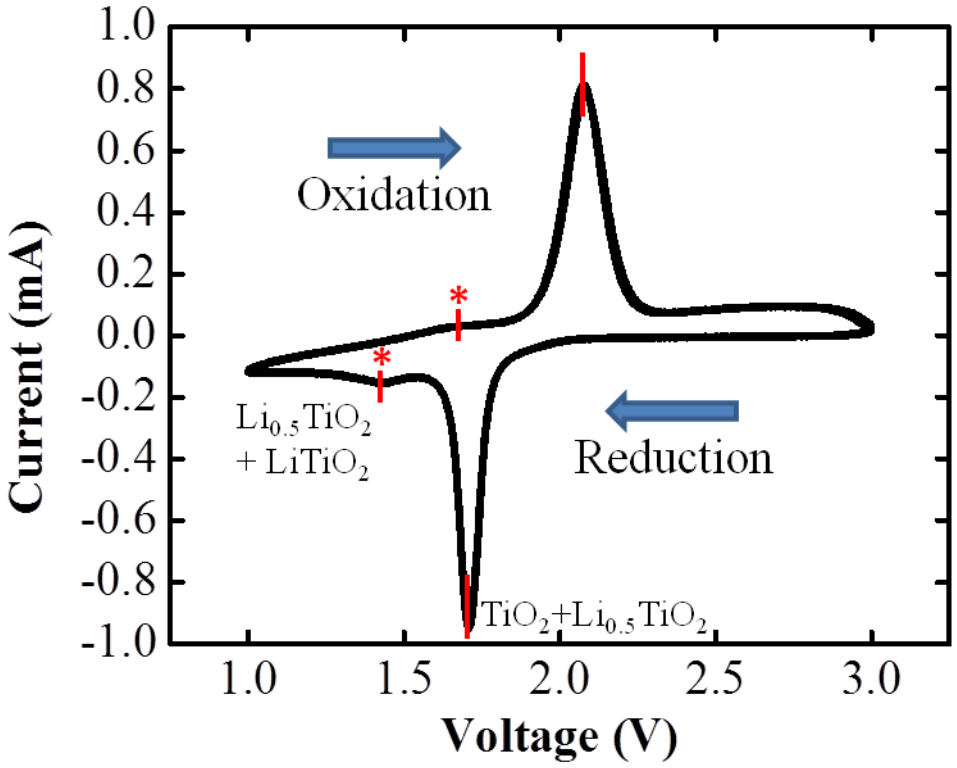

Figure B.1 Cyclic voltammetry curve of a TiO_2 NT film at the scan rate of 0.1mV/sec.

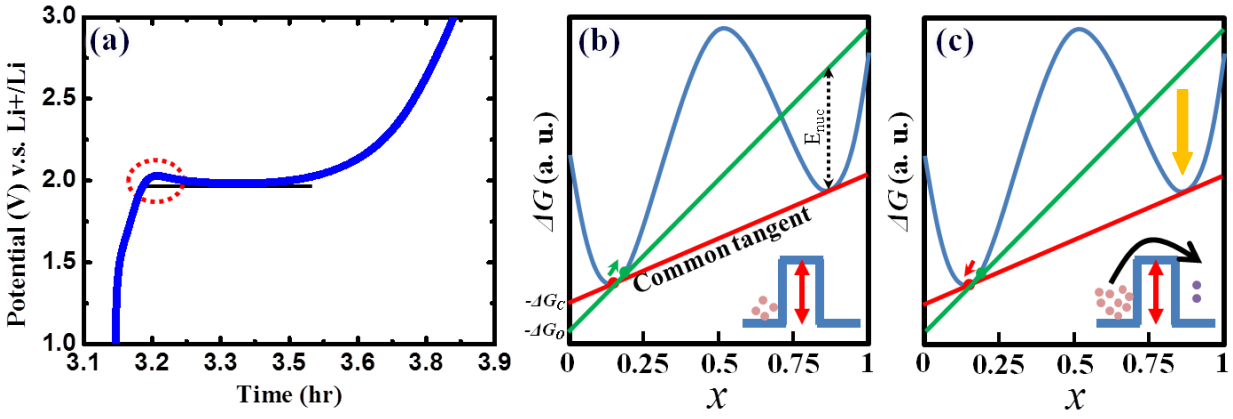

Figure B.2 a. A representative galvanostatic curve of a TiO_2 NT film upon 3rd discharge. An "overshoot" due to an over-potential is marked with red. **b and c.** Corresponding schematics of Gibbs free energy illustrating the sequential changes in a tangential line. An "overshoot" is possibly due to resistance of lithiated TiO_2 to nucleate the new phase, β-$Li_{0.5}TiO_2$.

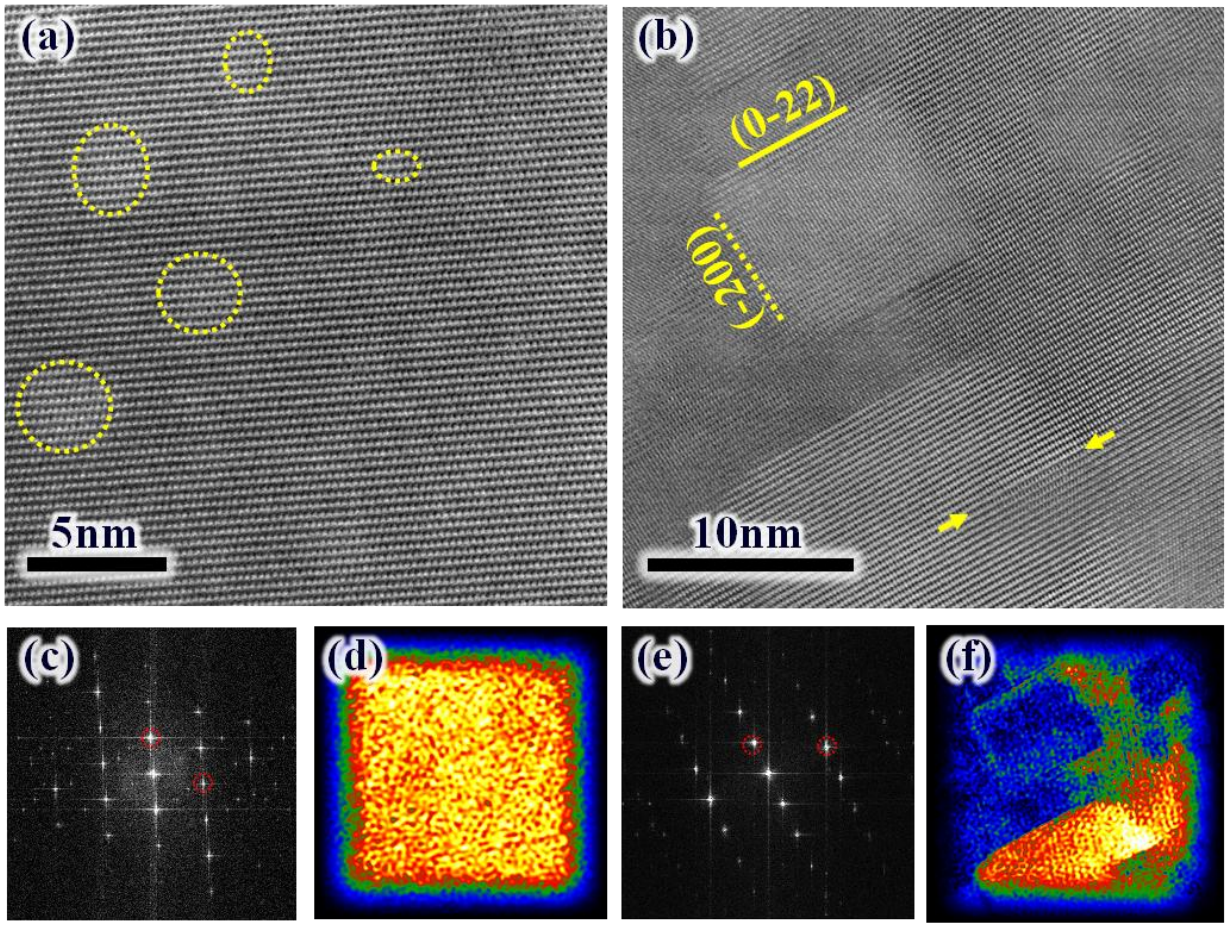

Figure B.3 HRSTEM images of a TiO_2 NT and their corresponding FFT patterns and Bragg-filtered maps **a, c, and d.** before and **b, e, and f.** after electrochemical cycling. The red circles on FFT patterns in c and e are the reciprocal lattice spots used for map calculation.

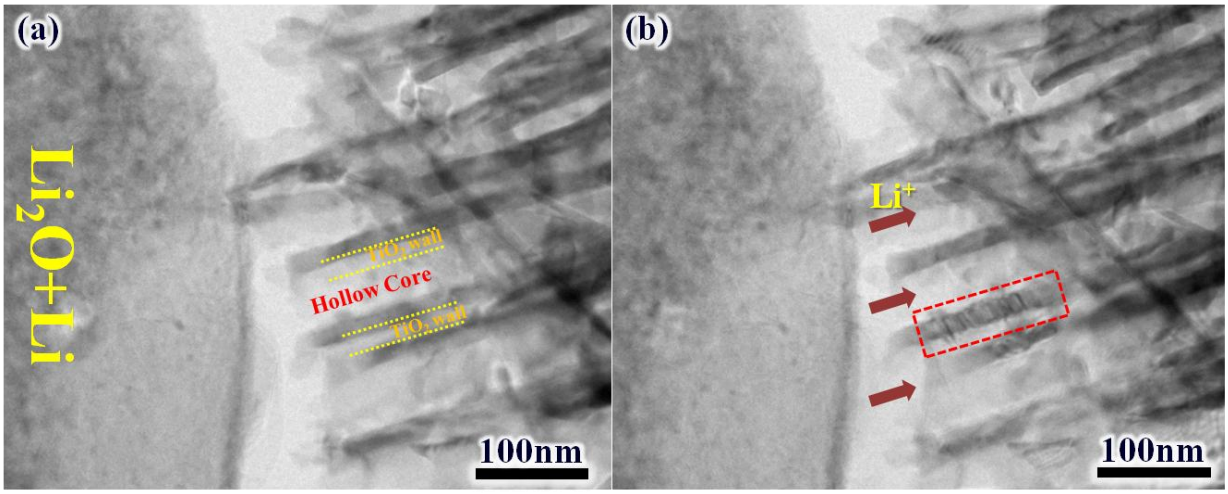

Figure B.4 Low-magnification TEM images of an anatase TiO_2 NT bundle **a.** before and **b.** during lithium insertion.

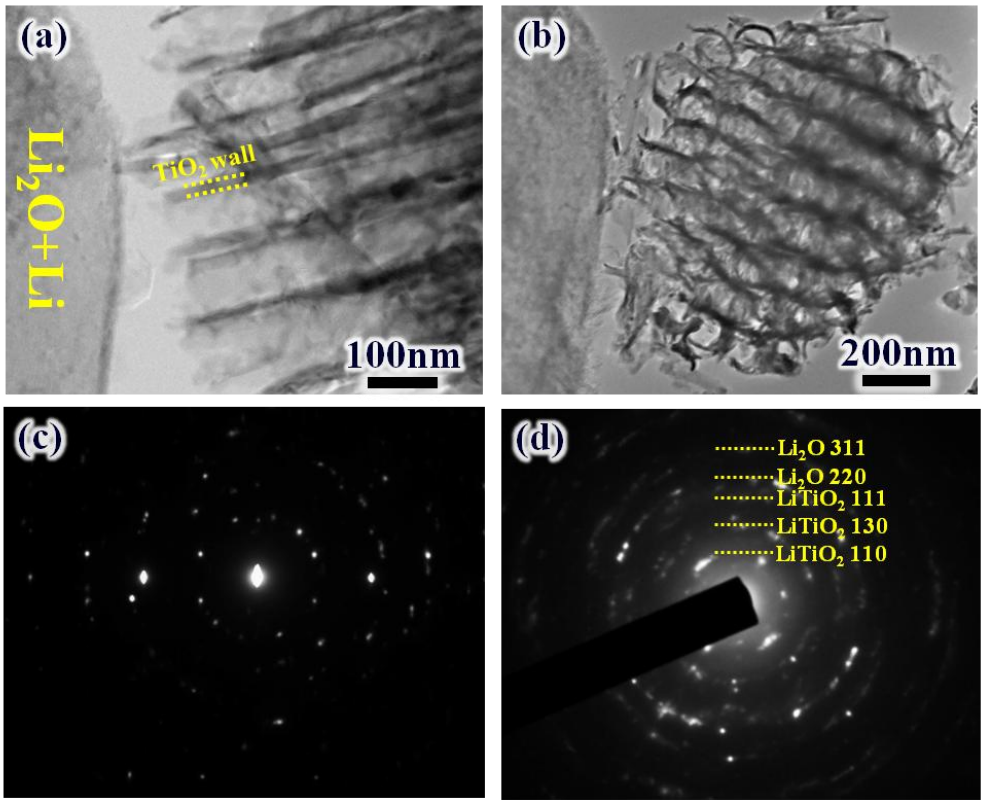

Figure B.5 Low-magnification TEM images of an anatase TiO_2 NT bundle **a.** before and **b.** after lithiation and **c and d.** corresponding SAED.

Appendix C Observation of a conversion reaction of a CuO nanowire upon Li insertion

C.1. Introduction and Background

The electrochemical study presented so far in this thesis has been dedicated to TiO_2 polymorphs that undergo insertion/de-insertion reaction upon Li insertion. As already discussed in Chapter 1, most of other binary transition metal oxides undergo a conversion reaction upon lithiation. Despite that less than one electron transfer is possible in intercalation materials, many possible oxidation states of transition metal oxides allow more than one electron transfer through a conversion reaction and, thus, greatly enhances specific charge capacity.[1] As one of widely studied conversion systems, CuO has been known to transform directly into metallic Cu nanoparticles upon Li-induced reduction. Upon Li extraction, the system irreversibly undergoes oxidation to Cu_2O, instead of CuO.[2] Here, the conversion reaction of CuO upon Li insertion was observed using high-resolution transmission electron microscopy (HRTEM).

C.2. Experimental methods

Monoclinic CuO NWs were grown on a copper foil using a thermal oxidation method as reported in elsewhere.[3] The procedures for TEM sample preparation and an in-situ TEM set-up for CuO NWs are similar to that described in Chapter 3 of the thesis.

C.3. Results and Discussion

Both schematics and TEM images in Figure C.1 demonstrate how lithiation proceeded under a potentiostatic mode of -3V. Clearly, as Li was driven from its source towards the other end of the NW, CuO immediately began to dilate both radially and vertically. A reaction front (as marked with yellow in Figure C.1b) had the distinct conical shape, which was indicative of faster Li diffusion along the surface than through the channels inside the NW.[4]

Ultimately, the entire NW underwent the radial and vertical expansion of 121%. and 119%, respectively. This expansion was kinetically induced upon reduction of CuO to Cu while oxygen ions were attached to Li to form a binary compound, Li_2O. This is shown in TEM images (Figure C.2a and b) by the change in the morphology of the NW before and after lithiation and the corresponding selected area electron diffraction (SAED) patterns (Figure C.2c and d). After lithiation, reduced 2-5 nm Cu nanoparticles got embedded in Li_2O matrix. Both the polcrystallinity of Cu and the amorphous nature of Li_2O are clearly marked by the ring patterns in SAED (Figure C.2d). A 5-7 nm thin layer that was observed at the surface of the lithiated NW is possibly a solid-electrolyte interphase (SEI) layer.

So far, lithiation of a CuO NW performed using Li_2O as a solid electrolyte demonstrated the similar result to that using a liquid electrolyte.[4] However, different from the liquid cell prototype case, upon applying reverse polarity, delithiation of the NW could not be achieved in our work. Instead, an interesting feature was detected near the interface between Li source and the NW (Figure C.3). Figures C.3b and c show the TEM images of a lithiated NW near and away from a Li contact, respectively, after a reverse bias was applied. Comparing to the smooth SEI layer

formed around the lithiated CuO NW away from the contact (Figure C.3c), the layer surrounding the NW near the contact was at least twice as large and very rough with jagged edges (Figure C.3b). It is suspected that these edges were induced by the growth of a Li_2O matrix followed by polycrystallization because the lattice spacing obtained in one of crystallites in Figure C.3d is 0.26 nm which is equivalent to the interplanar spacing of (111) Li_2O. There is still a large concentration of Li surrounding the NW, and hence it is possible that this layer could have grown more upon further applying a bias.

The expansion of Li_2O crystallites was resulted by the inefficient extraction of Li from the NW. Due to low Li ion conductivity of Li_2O electrolyte, Li ions that were unable to migrate back to the source were gradually accumulated at the Li source-NW contact to interact with surrounding residue oxygen ions from a TEM column.[5] Hence, upon replacing an electrolyte with higher ionic conductivity (i.e. ionic liquid electrolyte), the electrochemical reversibility could have enhanced as demonstrated in literature.[4]

C.4. Conclusions

In summary, electrochemical lithiation and delithiation on a CuO NW were performed under TEM. Upon lithiation, a CuO NW underwent a conversion reaction by reducing into metallic Cu embedded in a Li_2O matrix. However, delithiation upon applying a reverse bias was unsuccessful by inducing the formation and growth of large Li_2O crystallites surrounding the NW, most likely due to low Li ion conductivity of a solid electrolyte.

C.5. References

1. F. Wang, R. Robert, N. A. Chernova, N. Pereira, F. Omenya, F. Badway, X. Hua, M. Ruotolo, R. Zhang, L. Wu, V. Volkov, D. Su, B. Key, M. S. Whittingham, C. P. Grey, G. G. Amatucci, Y. Zhu, J. Graetz, "Conversion Reaction Mechanisms in Lithium Ion Batteries: Study of the Binary Metal Fluoride Electrodes", *J. Am. Chem. Soc.* **133** 18828-18836 (2011)

2. J. Cabana, L. Monconduit, D. Larcher, M. R. Palacín, "Beyond Intercalation-Based Li-Ion Batteries: The State of the Art and Challenges of Electrode Materials Reacting Through Conversion Reactions", *Adv. Mater.* **22** E170-E192 (2010)

3. X. Jiang, T. Herricks, Y. Xia, "CuO Nanowires Can Be Synthesized by Heating Copper Substrates in Air", *Nano Lett.* **2** 1333-1338 (2002)

4. X. Wang, D.-M. Tang, H. Li, W. Yi, T. Zhai, Y. Bando, D. Golberg, "Revealing the conversion mechanism of CuO nanowires during lithiation-delithiation by in situ transmission electron microscopy", *Chem. Commun.* **48** 4812-4814 (2012)

5. X. H. Liu, J. W. Wang, Y. Liu, H. Zheng, A. Kushima, S. Huang, T. Zhu, S. X. Mao, J. Li, S. Zhang, W. Lu, J. M. Tour, J. Y. Huang, "In situ transmission electron microscopy of electrochemical lithiation, delithiation and deformation of individual graphene nanoribbons", *Carbon* **50** 3836-3844 (2012)

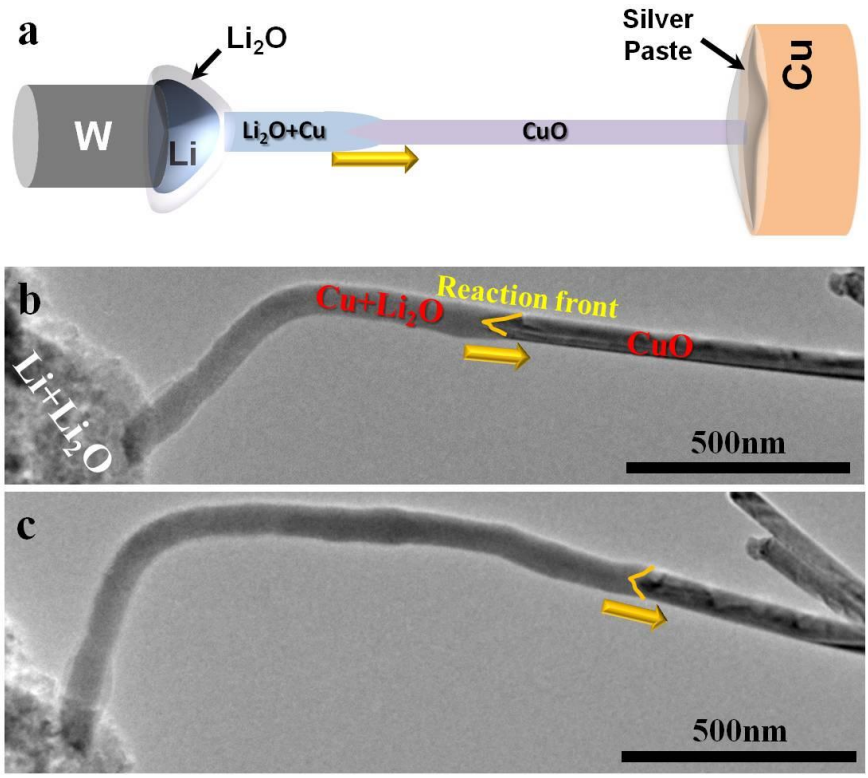

Figure C.1 a. A schematic illustrating the lithiation process of a CuO NW connected to the electrochemical set-up built inside TEM, **b and c.** TEM images demonstrating lithiation of CuO with the migration of a reaction front.

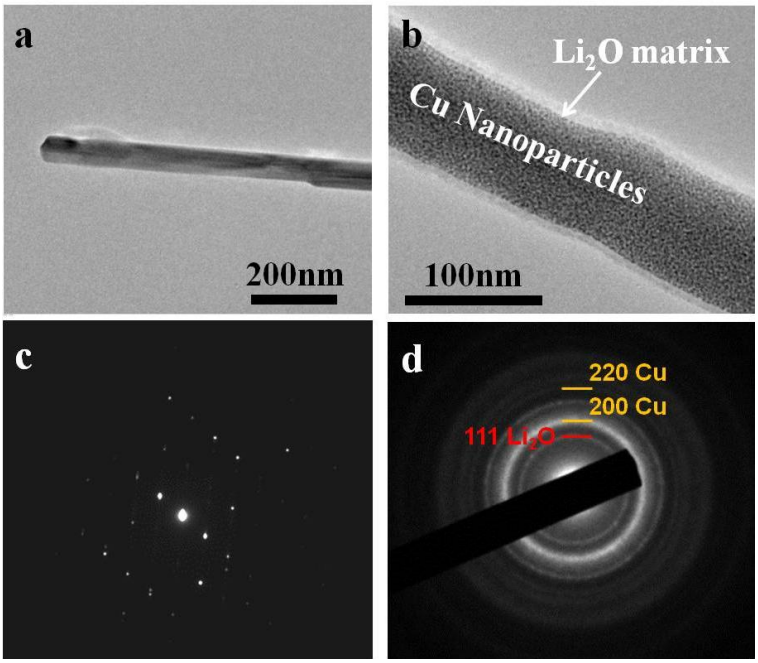

Figure C.2 TEM images and corresponding SAED patterns of a CuO NW **a and c.** before and **b and d.** after lithiation.

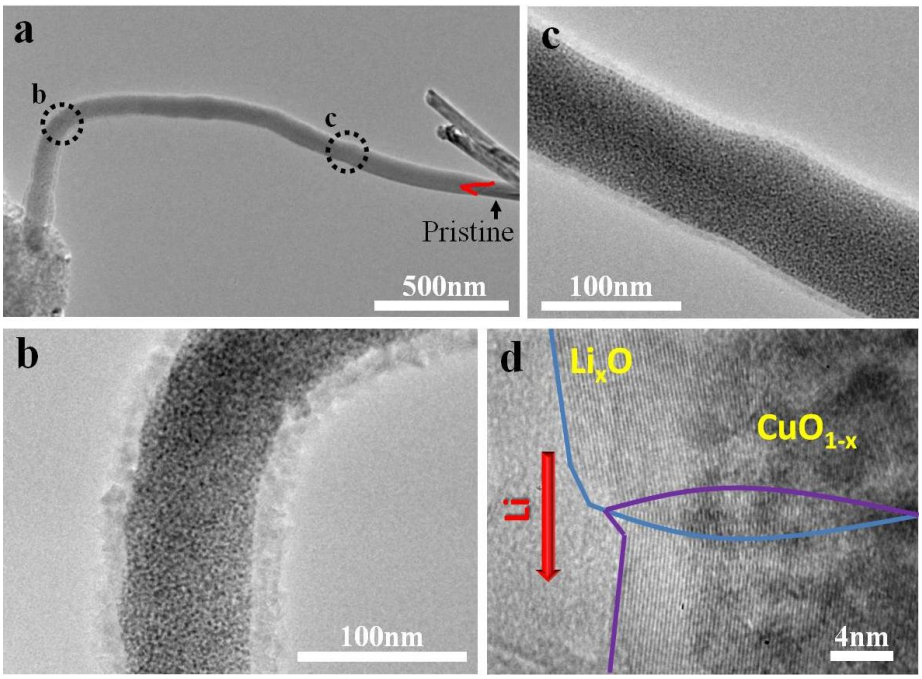

Figure C.3 a. A TEM image of a NW upon applying a reverse bias. **b and c.** Higher magnification TEM images of regions marked with b and c in **a**. d. HRTEM image of the NW surface near the Li source-NW contact.